IMPACT OF HELICOPTER MAIN ROTOR, AIRFRAME AND LANDING GEAR INTERACTIONS ON AIRFRAME LOADS DURING LANDINGS

A THESIS SUBMITTED TO
THE GRADUATE SCHOOL OF NATURAL AND APPLIED SCIENCES
OF
MIDDLE EAST TECHNICAL UNIVERSITY

BY

AHMED LEVENT UYGUN

IN PARTIAL FULFILLMENT OF THE REQUIREMENTS
FOR
THE DEGREE OF MASTER OF SCIENCE
IN
AEROSPACE ENGINEERING

JANUARY 2023

Approval of the thesis:

IMPACT OF HELICOPTER MAIN ROTOR, AIRFRAME AND LANDING GEAR INTERACTIONS ON AIRFRAME LOADS DURING LANDINGS

submitted by **AHMED LEVENT UYGUN** in partial fulfillment of the requirements for the degree of **Master of Science in Aerospace Engineering Department, Middle East Technical University** by,

Prof. Dr. Halil Kalıpçılar
Dean, Graduate School of **Natural and Applied Sciences** _____

Prof. Dr. Serkan Özgen
Head of Department, **Aerospace Engineering** _____

Assoc. Prof. Dr. İlkay Yavrucuk
Supervisor, **Aerospace Engineering, METU** _____

Examining Committee Members:

Prof. Dr. Ozan Tekinalp
Aerospace Engineering, METU _____

Assoc. Prof. Dr. İlkay Yavrucuk
Aerospace Engineering, METU _____

Prof. Dr. Tuncay Karaçay
Mechanical Engineering, Gazi University _____

Assoc. Prof. Dr. Nilay Sezer Uzol
Aerospace Engineering, METU _____

Assoc. Prof. Dr. Bülent Özkan
Mechanical Engineering, Gazi University _____

Date: 04.01.2023

I hereby declare that all information in this document has been obtained and presented in accordance with academic rules and ethical conduct. I also declare that, as required by these rules and conduct, I have fully cited and referenced all material and results that are not original to this work.

Name, Surname: Ahmed Levent Uygun

Signature :

ABSTRACT

IMPACT OF HELICOPTER MAIN ROTOR, AIRFRAME AND LANDING GEAR INTERACTIONS ON AIRFRAME LOADS DURING LANDINGS

Uygun, Ahmed Levent
M.S., Department of Aerospace Engineering
Supervisor: Assoc. Prof. Dr. İlkay Yavrucuk

January 2023, 100 pages

The complex and challenging landing problem in helicopters has long been studied using a combination of analytical models and experimental tests. This study takes a comprehensive approach by utilizing multi-body dynamics analysis of a 6-ton class helicopter to simulate various landing maneuvers in accordance with the certification standards set by organizations such as EASA and FAA. The conventional methods tend to focus solely on the interaction between the airframe and landing gear, neglecting the crucial role of rotor dynamics. This study aims to examine the complex and nonlinear interplay between the airframe, landing gear, and rotor during landing, and its impact on airframe loads.

The results of the study showed that conventional methods calculate the ground reactions relatively accurately, but not airframe accelerations. One cause of this discrepancy was found to be the gyroscopic effect of the rotor, which introduces pitch-roll coupling, leading to unbalanced forces. The study also revealed that the generally accepted assumption of constant lift during landing was invalid, as lift decreases upon touch down due to the rotor blades' flapping degree of freedom, resulting in increased

critical loads. Additionally, the aerodynamic forces acting on the blades were found to fluctuate during touch down. The findings of this study highlight the limitations of conventional methods and the need for a more comprehensive approach that considers the effects of rotor dynamics and blade behavior during helicopter landing.

Keywords: helicopter, landing, airframe loads, landing gear loads, multi-body dynamics

ÖZ

İNİŞ SIRASINDA HELİKOPTER ANA ROTORU, GÖVDE VE İNİŞ TAKIMI ETKİLEŞİMLERİNİN GÖVDE YÜKLERİNE ETKİSİ

Uygun, Ahmed Levent
Yüksek Lisans, Havacılık ve Uzay Mühendisliği Bölümü
Tez Yöneticisi: Doç. Dr. İlkay Yavrucuk

Ocak 2023 , 100 sayfa

Helikopterlerde zorlu ve karmaşık iniş sorunu, uzun süredir analitik modeller ve deneysel testlerin birleştirilmesiyle çalışılmaktadır. Bu çalışmada, EASA ve FAA gibi kuruluşlar tarafından belirlenen sertifikasyon standartlarına uygun olarak 6-ton sınıfı bir helikopterin iniş manevralarının benzetimini gerçekleştirmek için çoklu-cisim dinamiği analizi kullanarak kapsamlı bir yaklaşım benimsenmiştir. Geleneksel yöntemler genellikle gövde ve iniş takımı arasındaki etkileşime odaklanmakta ve rotor dinamiğinin önemli rolünü göz ardı etmektedir. Bu çalışma, gövde, iniş takımı ve rotorun iniş sırasındaki karmaşık ve çizgisel olmayan etkileşimini ve bu etkileşimin gövde yüklerine olan etkisini incelemeyi amaçlamaktadır.

Çalışmanın sonuçları, geleneksel yöntemlerin yer reaksiyonlarını nispeten isabetli olarak hesapladığını, ancak gövde ivmelelerini hesaplayamadığını göstermiştir. Bu tutarsızlığın nedenlerinden birinin, yunuslama ve yuvarlanmayı akuple ederek dengesiz kuvvetlere yol açan rotorun jiroskopik etkisinin olduğu bulunmuştur. Ayrıca, genellikle kabul gören iniş sırasında kaldırma kuvvetinin sabit kalması varsayımının

da geçersiz olduğu açığa vurulmuştur; çünkü pallerin çırpına serbestlik dereceleri nedeniye iniş sırasında gövdeye akan kaldırma kuvveti azalmakta ve kritik yüklerde artışlar olmaktadır. Paller üzerinde etkili olan aerodinamik kuvvetlerin de iniş sırasında salınım yaptığı gözlemlenmiştir. Bu çalışmanın bulguları, geleneksel yöntemlerin sınırlamalarını vurgulamış ve helikopter inişi sırasında rotor dinamiklerinin ve pal davranışlarının etkilerinin dikkate alındığı daha kapsamlı bir yaklaşımın gereksinimini ortaya koymuştur.

Anahtar Kelimeler: helikopter, iniş, gövde yükleri, iniş takımı yükleri, çoklu cisimler dinamiği

With gratitude, a small but heartfelt contribution to the thriving Turkish aviation

ACKNOWLEDGMENTS

I would like to express my deep gratitude to my supervisor, Dr. İlkay Yavrucuk, for inspiring me with his courses on flight mechanics and helicopter dynamics. His extensive knowledge and experience in the field of helicopters opened my eyes to the fascinating world of rotary-wing aircraft and ignited my passion for this research. I am grateful for the opportunity to have learned from such a talented and experienced educator.

I would also like to express my heartfelt thanks to my colleagues Uğur Kalkan and Harun Tıraş for their valuable contributions to the focus of my thesis. Their insightful discussions and ideas were instrumental in shaping the direction of my research, and I am grateful for the opportunity to have worked with such intelligent and thoughtful individuals.

I would be remiss if I didn't express my deepest gratitude to İmge Yığılı, who was my ultimate coffee supplier throughout the thesis-writing process. Her unwavering support and encouragement kept me going even when I wanted to throw in the towel (or, more accurately, toss my laptop out the window).

I would also like to thank Buğra Köksal and Gürkan Sertsoy for helping me maintain my morale while I was struggling to meet my deadlines during my graduate studies. They did this by simply being in worse situations than myself, which helped me to keep things in perspective, for which I am grateful.

Lastly, I am grateful to my company TUSAŞ for providing me with resources, particularly the access to licensed software.

TABLE OF CONTENTS

ABSTRACT v

ÖZ vii

ACKNOWLEDGMENTS x

TABLE OF CONTENTS xi

LIST OF TABLES xiii

LIST OF FIGURES xv

CHAPTERS

1 INTRODUCTION 1

1.1 Motivation and Problem Definition 1

1.2 Literature Review 3

1.3 Proposed Method 4

2 MODEL DEVELOPMENT 7

2.1 Model A: Static Analysis Model 8

2.1.1 Landing Gears 10

2.1.1.1 Shock Absorbers 11

2.1.1.2 Tires 15

2.1.1.3 Unsprung Mass 17

2.2 Model B: Dynamic Analysis Model Without Rotor 17

2.3 Model C: Dynamic Analysis Model With Rotor 20
2.3.1 Rotor Aerodynamic Model 25
3 METHOD 35
3.1 3-Point Landing 39
3.2 Tail-Down Landing 42
3.3 Lateral Slope Landing 45
3.4 Running Landing 49
4 RESULTS 57
4.1 3-Point Landing 57
4.2 Tail-Down Landing 67
4.3 Lateral Slope Landing 76
4.4 Running Landing 84
5 CONCLUSIONS 95
REFERENCES 97

LIST OF TABLES

TABLES

Table 2.1 Shock absorber spring and damper design parameters 14

Table 2.2 Overall mass properties of the helicopter 18

Table 2.3 Mass breakdown of individual landing gear components 19

Table 2.4 Kinematic details of Model B 20

Table 2.5 Rotor components and their numbers 22

Table 2.6 Kinematic details of the rotor model 23

Table 2.7 Rotor model design parameters 24

Table 3.1 Summary of key landing parameters by maneuver 37

Table 3.2 Positions of the selected monitor stations in Body coordinate system 38

Table 3.3 MOG values for Model A in 3-point landing 40

Table 3.4 MOG values for Model A in tail-down landing 44

Table 3.5 MOG values for Model A in lateral slope landing 48

Table 4.1 Linear accelerations obtained in 3-point landing. Unit is [m/s^2] . . . 57

Table 4.2 Angular accelerations and velocities obtained in 3-point landing . . 58

Table 4.3 Maximum ground reactions obtained in 3-point landing, in Newtons 59

Table 4.4 Linear accelerations obtained in tail-down landing. Unit is [m/s^2] . . 67

Table 4.5 Angular accelerations and velocities obtained in tail-down landing . 67

Table 4.6 Maximum ground reactions obtained in tail-down landing, in Newtons 71

Table 4.7 Linear accelerations obtained in lateral slope landing. Unit is [m/s^2] 76

Table 4.8 Angular accelerations and velocities obtained in lateral slope landing 76

Table 4.9 Linear accelerations obtained in running landing. Unit is [m/s^2] . . . 85

Table 4.10 Angular accelerations and velocities obtained in running landing . . 85

Table 4.11 Maximum ground reactions obtained in running landing, in Newtons 86

LIST OF FIGURES

FIGURES

Figure 1.1 Main landing gear structure and drop test tower 4

Figure 1.2 Eurocopter Tiger helicopter bending moment values for different maneuvers during the limit load test campaign 6

Figure 2.1 Reference helicopters for geometric parameter selection 7

Figure 2.2 Basic schematic of Model A 8

Figure 2.3 Model A 10

Figure 2.4 The inner mechanism of an oleo-pneumatic shock absorber . . . 11

Figure 2.5 Spring and damper properties of MLG and NLG shock absorbers 15

Figure 2.6 Stiffness properties of MLG and NLG tires 16

Figure 2.7 Side (top), front (left) and isometric (right) views of Model B . . 17

Figure 2.8 Dimensions of the airframe as seen in side (left) and front (right) views 18

Figure 2.9 Schematic of Airbus H160 helicopter's main rotor 21

Figure 2.10 Front (top), side (middle) and isometric (bottom) views of Model C 21

Figure 2.11 Isometric view of the rotor model components 22

Figure 2.12 Velocities, angles and forces on a typical blade element 25

Figure 2.13 Free body diagram of the blade in the rotating non-inertial frame 29

Figure 2.14 Flowchart for the solution procedure of collective and flapping angles 29

Figure 2.15 Sectional tangential and perpendicular velocities on the blade . . 30

Figure 2.16 Sectional incident angles on the blade 30

Figure 2.17 Sectional lift and drag coefficients on the blade 31

Figure 2.18 Lift and drag distributions on the blade 32

Figure 2.19 Lift distribution across the blade span for different flapping rates, $\dot{\beta}$ 33

Figure 3.1 Minimum rate of descent in autorotation studies of Leishman (left) and Prouty (right) 37

Figure 3.2 Side view of 3-point landing analysis with Model A 39

Figure 3.3 Side view of 3-point landing analysis with Model B 41

Figure 3.4 Isometric view of 3-point landing analysis with Model C 41

Figure 3.5 Side view of tail-down landing analysis with Model A 42

Figure 3.6 Free body diagram for tail-down landing inertia relief method . . 43

Figure 3.7 Isometric view of tail-down landing analyses with models B (top) and C (bottom) 45

Figure 3.8 Free body diagram for lateral slope landing inertia relief method 46

Figure 3.9 Contour plot of the ratio of calculated MOG in one-wheel landing to the MOG in 2-point landing for a range of I_{xx} and y values, with the slope angle set to zero. The helicopter used in this study is represented by the red dot 47

Figure 3.10 Front view of lateral slope landing analysis with Model B 49

Figure 3.11 Front view of lateral slope landing analysis with Model C 49

Figure 3.12 Time histories of vertical and drag forces, as well as spin-up and spring-back loads during a running landing 50

Figure 3.13 Variation of friction coefficient with respect to slip ratio 51

Figure 3.14 Assumed profiles for the development of ground reactions in vertical and drag directions for the spin-up analysis 53

Figure 3.15 Free body diagram of the MOG in vertical axis during landing impact 54

Figure 3.16 Free body diagram of the wheel in rotation axis during landing impact 55

Figure 4.1 Time variation of ground reaction forces in Model C during 3-point landing 59

Figure 4.2 Comparison of ground reactions between the models in 3-point landing 60

Figure 4.3 Time variation of vertical acceleration of the CG and pitching acceleration of the helicopter during 3-point landing 61

Figure 4.4 Time variation of vertical acceleration of the monitoring stations on the nose and tail sections during 3-point landing 61

Figure 4.5 Time variation of left and right MLG ground reactions of Model C during 3-point landing 62

Figure 4.6 Velocities and accelerations around pitching and rolling axes in Model C during 3-point landing 63

Figure 4.7 Flap response of the rotor blades in Model C during 3-point landing 64

Figure 4.8 Flap response of an individual blade and rotor force acting on the airframe in Model C during 3-point landing 64

Figure 4.9 Flap rate of the blades and total aerodynamic lift acting on the blades in Model C during 3-point landing 65

Figure 4.10 Lead-lag damper force acting on the blades in Model C during 3-point landing 66

Figure 4.11 Comparison of ground reaction and shock absorber forces on left MLG unit in Model C during 3-point landing 66

Figure 4.12 Time variation of ground reactions, vertical accelerations and pitching acceleration in Model B during tail-down landing 68

Figure 4.13 Time variation of ground reactions, vertical accelerations and angular accelerations in Model C during tail-down landing 69

Figure 4.14 Comparison of MLG ground reactions between the models in tail-down landing 70

Figure 4.15 Time variation of vertical acceleration of the CG and pitching acceleration of the helicopter during tail-down landing 72

Figure 4.16 Time variation of vertical acceleration of the monitoring stations on the nose and tail sections during tail-down landing 72

Figure 4.17 Flap response of the rotor blades in Model C during tail-down landing 73

Figure 4.18 Flap response of an individual blade and rotor force acting on the airframe in Model C during tail-down landing 73

Figure 4.19 Flap rate of the blades and total aerodynamic lift acting on the blades in Model C during tail-down landing 74

Figure 4.20 Lead-lag damper force acting on the blades in Model C during tail-down landing 75

Figure 4.21 Comparison of ground reaction and shock absorber forces on left MLG unit in Model C during tail-down landing 75

Figure 4.22 Time variation of ground reactions, vertical accelerations and angular accelerations in Model B during lateral slope landing 77

Figure 4.23 Comparison of ground reactions between the models in lateral slope landing 78

Figure 4.24 Time variation of vertical and lateral accelerations of the CG during lateral slope landing 79

Figure 4.25 Time variation of angular accelerations of the helicopter during lateral slope landing 79

Figure 4.26 Time variation of vertical acceleration of the monitoring stations on the nose and tail sections during lateral slope landing 80

Figure 4.27 Time variation of lateral acceleration of the monitoring stations on the nose and tail sections during lateral slope landing 81

Figure 4.28 Flap response of the rotor blades in Model C during lateral slope landing 81

Figure 4.29 Flap response of an individual blade and rotor force acting on the airframe in Model C during lateral slope landing 82

Figure 4.30 Flap rate of the blades and total aerodynamic lift acting on the blades in Model C during lateral slope landing 83

Figure 4.31 Lead-lag damper force acting on the blades in Model C during lateral slope landing 83

Figure 4.32 Comparison of ground reaction and shock absorber forces on left MLG unit in Model C during lateral slope landing 84

Figure 4.33 Comparison of longitudinal ground reactions between the models in running landing 86

Figure 4.34 Comparison of vertical ground reactions between the models in running landing 87

Figure 4.35 Time variation of vertical, longitudinal and pitching accelerations during running landing 87

Figure 4.36 Time variation of vertical acceleration of the monitoring stations on the nose and tail sections during running landing 88

Figure 4.37 Time variation of longitudinal acceleration of the monitoring stations on the nose and tail sections during running landing 89

Figure 4.38 Comparison of vertical ground reactions between the 3-point and running landing maneuvers, in Model C 90

Figure 4.39 Evolution of vertical ground reactions to their maxima in running landing for models A and C 90

Figure 4.40 Evolution of longitudinal ground reactions to their maxima in running landing for models A and C 91

Figure 4.41 Flap response of the rotor blades in Model C during running landing 92

Figure 4.42 Flap response of an individual blade and rotor force acting on the airframe in Model C during running landing 92

Figure 4.43 Flap rate of the blades and total aerodynamic lift acting on the blades in Model C during running landing 93

CHAPTER 1

INTRODUCTION

1.1 Motivation and Problem Definition

The design of a helicopter's structure presents several difficulties, including the need to consider aspects such as maintenance, repairability, availability, and affordability, in order to guarantee safe and efficient operation of the aircraft [1]. However, the primary objective is to ensure the strength and load-bearing capabilities of the structure.

Loads play a crucial role in helicopter structural design. The structure's ability to withstand different loading conditions, including those encountered during take-off, flight, and landing, is a critical aspect in the design process. Accurately predicting the loads acting on the airframe is crucial for ensuring the structural integrity and safety of the vehicle. Furthermore, loads drive the structural design, influencing the choice of materials, the structural elements' size and shape, and the overall configuration of the helicopter.

Loads in a helicopter are categorized into two groups: limit and operational loads. Limit loads are the maximum loads the helicopter may encounter during its service life, including conditions such as aggressive pull-up maneuvers or landing with high sink speeds. These loads drive the design of the helicopter's primary structure and are used in the static sizing of elements such as the airframe and main equipment attachments. Since limit loads occur during the most extreme maneuvers and cannot always be verified through testing, mathematical accuracy in limit load analysis is essential.

On the other hand, operational loads are the loads experienced during regular use,

such as those encountered during hover and forward flight. These loads are used in the design against metal fatigue and, although analytically calculated, rely heavily on testing results due to the complexity of physical phenomena involved, such as unsteady aerodynamics, structure elasticity, and vibration.

This study focuses on the limit loads due to their crucial role in the static sizing of the helicopter's structure and the mathematical accuracy required in their analysis.

The loads acting on the helicopter's airframe are further classified into four categories: flight loads, landing loads, rotor loads, and miscellaneous loads [2]. Flight loads encompass the loads encountered during various flight conditions, such as forward flight or lateral flight. Landing loads refer to the loads experienced during landing and ground maneuvers, including landing on three wheels or tail-down landing. The loads on the rotor's specific components during flight are known as rotor loads, and miscellaneous loads include other load conditions such as towing or hoisting that don't fall under the other three categories.

The landing gear of a helicopter plays a critical role in the safe operation of the aircraft, as it supports the helicopter during various ground operations including takeoff, landing impact, taxiing, and maintenance. The design of the landing gear must strike a balance between minimal weight and structural integrity, as it also serves as a useless mass during flight. Accurate calculation of landing loads is essential in landing gear design as it ensures that the landing gear can perform its requirements while being as lightweight as possible. The landing gear system must be able to absorb the vertical energy of the aircraft during landing through the shock absorber and the horizontal kinetic energy through the braking system, while also supporting the aircraft on taxiways and runways of varying quality. The landing gear system is a crucial component and its dynamics must be understood in-depth for both aircraft design and safety, as it lacks redundancies and has multiple conflicting requirements [3].

In the current state of helicopter design, there exists a disconnection between the analysis of landing loads and rotor loads. Traditionally, rotor component loads are not considered in landing load analyses, and only flight conditions are considered in

rotor load analyses. This results in a lack of understanding of the interactions between the helicopter's airframe, landing gear, and rotor during landing maneuvers and ground operations. This disconnection in load analysis can lead to an underestimation of the loads experienced by the helicopter during landing, potentially leading to structural failure. Therefore, it is crucial for future research in helicopter design to consider the interaction between the airframe, landing gear, and rotor in order to ensure the safe and effective operation of the aircraft.

1.2 Literature Review

The structural implications of rotorcraft landing are under-explored in open scientific literature and there is a shortage of tools for landing simulation. The open literature lacks a comprehensive approach that can effectively simulate the landing event from both dynamic and structural perspectives [4].

The existing literature on helicopter landing loads tends to focus solely on the interactions between the landing gear and airframe, neglecting the impact of rotor dynamics. A study by Cristiani et al. [4] simulated and validated a full-scale, elastic helicopter drop test but did not include the rotor in the model. Similarly, Nicholas [5] performed a multi-body dynamics analysis of an elastic landing gear-airframe system and compared the results to those of a drop test method, but also excluded the rotor. In the similar study of McClintick and Darlington [6], a comparison was made with drop test results by including the elastic mode of the airframe in the analysis, yet the rotor was again not considered in the analysis. Vallone et al. [7] conducted a multi-body analysis that focused on the effects of hard landing conditions on fuselage damage, albeit without a rotor model.

On the other hand, studies that examine rotor component loads tend to focus solely on the rotor and disregard the airframe or landing gear. For instance, Özturan [8] created an elastic multi-body dynamics model of the rotor, but it was isolated from the rest of the helicopter and did not take into account landing conditions. Similarly, Guivarch et al. [9] studied rotor loads in a multi-body dynamics setting, but only considered

dynamic loads that were not related to landing events. Lastly, Lee et al [10] built a rotor model for structural dynamics analysis, but it was an isolated rotor model and investigated the aerodynamics of the rotor.

While some studies have integrated landing gear and rotor models, a comprehensive examination of airframe loads during limit landing maneuvers has yet to be done. Dong et al. [12] developed a multi-body model encompassing the rotor, airframe, and landing gear, however they focused on rotor startup events instead of landing. Stanisławski [11] created a similar multi-body model including all components and studied take-off and landing operations, but did not examine high-sink-speed limit landing maneuvers or assess critical airframe loads.

1.3 Proposed Method

The evaluation of loads during helicopter landing events is typically approached through simplifying the helicopter as a mass-spring-damper system. This method is favored for its simplicity and cost-effectiveness compared to full-scale landing tests with a real helicopter, which can be complex and expensive. To approximate landing events, a drop test tower is used in a specialized testing environment as depicted in Figure 1.1, which is deemed sufficient by certifying standards such as CS and FAR. If the load factors measured in a drop test exceed those calculated analytically, the helicopter is considered acceptable for certification per CS-29.473(b).

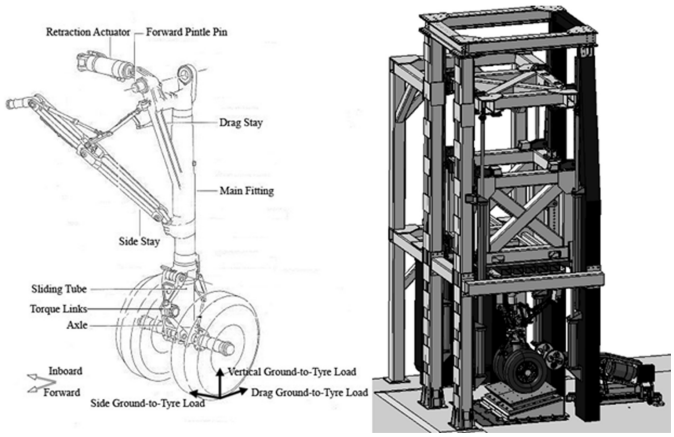


Figure 1.1: Main landing gear structure and drop test tower [13]

In drop test, the primary focus is typically on the evaluation of the vertical loads and accelerations, while other acceleration components such as angular accelerations are ignored. A lift force is applied to the drop mass to simulate the lift experienced by the helicopter during landing, and the lift force is assumed to be constant, as per certification standard article 29.473(a) of CS and FAR. To simplify the testing procedure, the practice of disregarding the lift force and calculating an equivalent drop mass without lift was introduced in a NACA report in 1955 [14]. This approach further simplifies the landing problem and has been widely used and deemed reliable in representing landing load conditions in numerous studies and practical applications, as well as accepted by certification authorities like CS and FAR. However, the validity and accuracy of this method should continue to be evaluated to improve the understanding of helicopter landing loads and enhance aircraft design and airworthiness.

In this scholarly investigation, the conventional method of calculating landing loads, which overlooks the interactions between the helicopter's multiple landing gears and its main rotor, will be scrutinized through the utilization of three diverse multi-body dynamics models. In order to obtain a comprehensive understanding of the helicopter's dynamic behavior during landing and pinpoint potential areas for enhancement or optimization, it is imperative to integrate the rotor into the analysis as a paramount component. The first model to be established is a two-degree-of-freedom system that exemplifies a drop test scenario and adheres to the widely accepted approach. The second and third models are 6 degree of freedom helicopter models, with the second model accounting for the interactions between the landing gear and the airframe, and the third model incorporating the main rotor and enabling a full-scale examination. Thus, examination of the force that is transferred from the rotor to the airframe and its temporal change through landing is to be performed, by taking the inertial effects of the blades, rotor components and the aerodynamic force exerted on the rotor into consideration. This results in an opportunity to evaluate the fidelity of the constant lift assumption. Consequently, the objective of these models is to assess the validity of the conventional approach and evaluate the effect of including the rotor and other interactions on the calculated landing loads.

In summary, this study aims to examine the validity of the current method of cal-

culating landing loads, which is based on drop tests, through the use of three distinct models. The first model represents the conventional approach with a 2 degree of freedom system for drop test events, while the second and third models are 6 degree of freedom helicopter models that account for the interactions between the landing gear and airframe, and include the main rotor for a comprehensive analysis, respectively. The comparison between the first and second models will highlight the impact of different analytical methods on the calculated landing loads, and the comparison between the second and third models will evaluate the effect of rotor dynamics on the landing problem.

This study will also offer the capability to calculate the loads on rotor components during landing conditions. As demonstrated by Figure 1.2, the Tiger helicopter experiences the highest main rotor shaft bending moment during taxi and sloped surface landings. The models developed will provide insights into such scenarios, expanding the scope of the study beyond what is covered in this report.

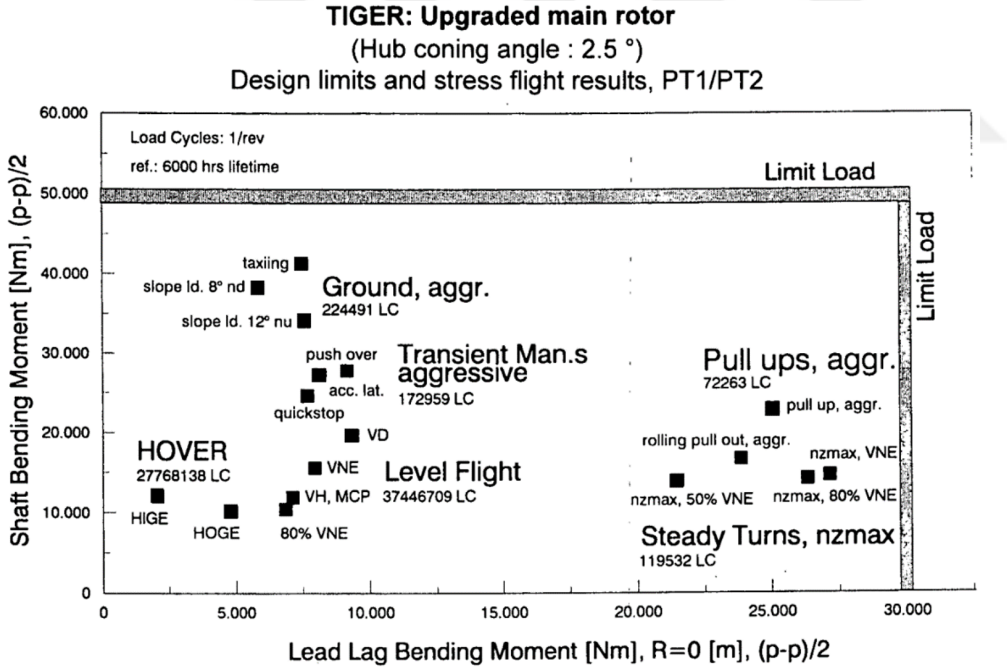


Figure 1.2: Eurocopter Tiger helicopter bending moment values for different maneuvers during the limit load test campaign [15]

CHAPTER 2

MODEL DEVELOPMENT

Simcenter Motion software was used for multi-body dynamics modeling. Simcenter is a multi-disciplinary computer-aided engineering (CAE) software that includes finite element, thermal, fluid, and electronic analysis capabilities, in addition to the Motion environment used for dynamic motion analysis. The Motion environment within Simcenter is preferred due to its ability to directly work on CAD models, easily specify the mass properties of objects, clearly define the joints that interact with them, and easily define external forces and initial conditions.

A conceptual helicopter with a maximum takeoff mass of 6 tons, wheeled landing gear, and a fully articulated rotor was studied. Geometric parameters of the conceptual helicopter's airframe, landing gear placement and rotor design were determined by averaging values from similar weight class helicopters, including H160, H175, T625, and AW169, which can be seen in Figure 2.1.



Airbus – H160 | TUSAŞ – T625

Airbus – H175 | Agusta Westland – AW169

Figure 2.1: Reference helicopters for geometric parameter selection

In this study, three different models were studied with varying levels of complexity. These are (A) a model where only one landing gear can be displaced in the direction of gravitational force, (B) a model where the landing gear and the airframe have 6 degrees of freedom, and (C) a model where the landing gear, the rotor, and the airframe have 6 degrees of freedom. The details of each model are discussed in more detail in the subsequent chapters.

2.1 Model A: Static Analysis Model

This model was created in order to provide the required inputs for the generally accepted static analysis method explained in Chapter 1.3. Additionally, this model will serve as a reference for comparing the results of the more complex models B and C. A schematic representation of Model A is depicted in Figure 2.2.

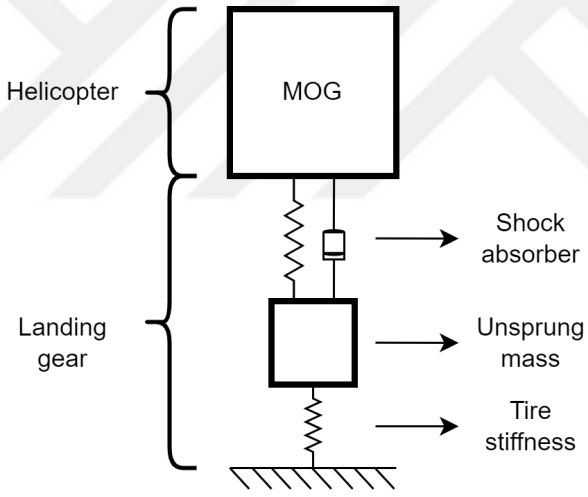


Figure 2.2: Basic schematic of Model A

As can be seen, Model A is a simplified representation of the helicopter during landing, comprising a single landing gear and a mass element representing the helicopter's mass supported by that specific landing gear. This mass element is commonly referred to as the *mass over gear* or, alternatively, the acronym MOG. Calculation of MOG for various types of landing maneuvers is discussed in Chapter 3.

This method focuses on identifying the linear and angular accelerations at the cen-

ter of gravity (CG) of the helicopter. Upon determination of these acceleration terms, the linear acceleration of any point on the airframe with respect to an inertial frame can be calculated using Equation 2.1.

$$\vec{a}' = \vec{a} + \vec{\alpha} \times \vec{r} + \vec{\omega} \times (\vec{\omega} \times \vec{r}) + 2\vec{\omega} \times \vec{v} \tag{2.1}$$

In this context, certain vectors are defined to represent various physical quantities. The vectors $\vec{a}'$, $\vec{a}$, $\vec{\alpha}$, and $\vec{\omega}$ are defined with respect to an inertial frame, while the vectors $\vec{r}$ and $\vec{v}$ are defined with respect to the helicopter reference frame. Specifically, $\vec{a}'$ represents the linear acceleration at the point of load measurement, $\vec{a}$ represents the linear acceleration at the CG, $\vec{\alpha}$ represents the angular acceleration of the helicopter, and $\vec{\omega}$ represents the angular velocity of the helicopter. Finally, $\vec{r}$ represents the position and $\vec{v}$ represents the velocity of the point of load measurement.

A vector equation is independent of any specific coordinate frame, which means that it holds true regardless of the reference frame in which it is expressed. However, when making quantitative calculations, it is necessary to represent the vectors in a specific coordinate system in order to have a clear understanding of the physical quantities being represented and to be able to perform the calculations accurately.

To facilitate these calculations, all the vectors in Equation 2.1 are expressed in the body coordinate system. The body coordinate system is a non-inertial frame that is fixed to the helicopter and moves and rotates with it. The origin of the body coordinate system is located at the CG of the helicopter. The x-axis of the body coordinate system is parallel to the helicopter's stationline, with the positive direction pointing forward. The z-axis is parallel to the waterline, with the positive direction pointing downward and y-axis completes the right-handed coordinate system.

Since this method is a static analysis technique, angular velocities are not taken into account. Also, loads are measured at fixed points in the body coordinate system. As a result, vectors $\vec{\omega}$ and $\vec{v}$ and the corresponding centrifugal and Coriolis acceleration terms are not present. This leads to the simplification of Equation 2.1 to Equation 2.2 for this specific problem.

$$\vec{a}' = \vec{a} + \vec{\alpha} \times \vec{r} \tag{2.2}$$

In order to determine the vectors $\vec{a}$ and $\vec{\alpha}$, it is necessary to calculate the net force and moment on the helicopter. The forces acting on the helicopter include the ground reaction forces on the three landing gears, the lift force, and the weight. The lift force is applied at the CG as per CS 29.473(a) and does not generate a moment. To determine the forces on the landing gears, models of the main landing gear (MLG) and the nose landing gear (NLG) with two degrees of freedom were created in Simcenter Motion and are shown in Figure 2.3. These models will be used to calculate the ground reaction forces on the landing gears.

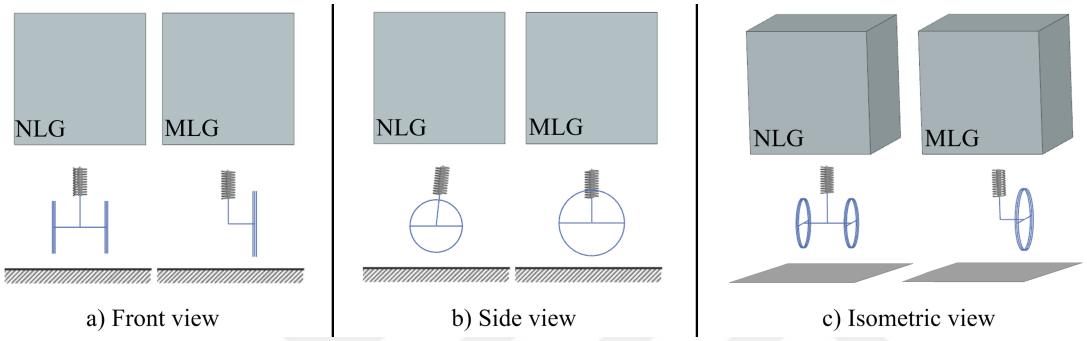


Figure 2.3: Model A

As illustrated, in this model, the NLG and MLG are treated as distinct and isolated from one another.

As the landing gears are the primary sources of force acting on the helicopter during landing, it is important to model them accurately. The details of the landing gear models, including the assumptions and simplifications made in their development, will be discussed in the next sub-chapter.

2.1.1 Landing Gears

Landing gears are essential components of a helicopter, responsible for supporting the aircraft during takeoff, landing, and ground operations. These systems are typically composed of two main parts: the shock absorber and the tire, as illustrated in Figure 2.2.

2.1.1.1 Shock Absorbers

The design of the shock absorber is a critical factor in the determination of forces acting on the landing gear. For this study, the use of oleo-pneumatic shock absorbers was chosen. Oleo-pneumatic landing gear technology has gained widespread adoption in modern aviation due to its effectiveness in efficiently dissipating large amounts of energy over a short period of time. This technology has enabled the continued expansion of aircraft dimensions, weight, and flight speed, while maintaining safe landing capabilities throughout the operational life of the vehicle. Oleo-pneumatic struts offer a compact size, competitive weight, and long fatigue life, making them a preferred alternative to classical solutions [16]. Main components of a oleo-pneumatic shock absorber can be see in Figure 2.4

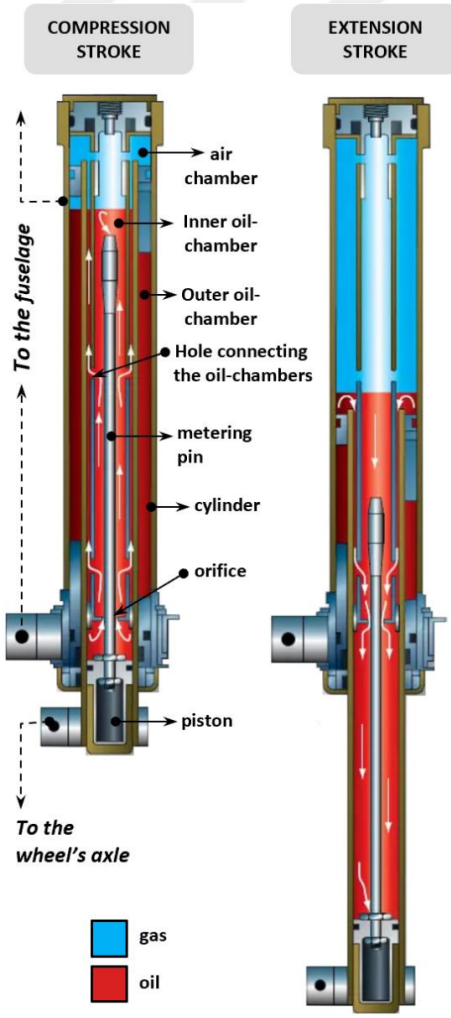


Figure 2.4: The inner mechanism of an oleo-pneumatic shock absorber [16]

The inner mechanism of an oleo-pneumatic shock absorber consists of a piston that moves within a cylinder and is sealed by a set of seals. The cylinder is filled with a mixture of gas and oil, which is separated by the piston. The gas, typically air or nitrogen, is compressed as the shock absorber is subjected to load and helps to reduce the amount of oil that is displaced. The oil, on the other hand, helps to absorb the energy of the load and acts as a damping mechanism. The movement of the piston is controlled by a set of valves, which regulate the flow of oil through the shock absorber and determine its damping characteristics. The overall performance of the shock absorber can be adjusted by varying the size of the cylinder, the composition of the gas and oil, and the design of the valves [17].

The spring and damping characteristics of an oleo-pneumatic shock absorber are commonly determined by the thermodynamic properties of the gas and oil within it, as well as the internal mechanical design of the shock absorber. In this study, a simplified approach will be utilized to model the oleo-pneumatic shock absorber as a spring-damper system. While a higher fidelity CFD analysis may be required to more accurately determine the spring and damping characteristics of the shock absorber, as demonstrated in the work of Du et al. [17], the simplified approach is suitable for the analysis being conducted.

The simplified approach for modeling the oleo pneumatic shock absorber as a spring-damper system involves using the gas compression law, as given in Equation 2.3, to determine the non-linear spring coefficient. This method has been previously described in the work of Krüger and Moradini [18].

$$F_s = F_0 \left(1 - \frac{s}{s_m}\right)^{-\gamma c_k} \tag{2.3}$$

where F_s represents the spring force, F_0 represents the preload force, s represents the amount of compression of the shock absorber, s_m represents the total length of the shock absorber, γ represents the polytropic coefficient, and c_k represents the correction factor, which is typically between 0.9 and 1.1 and is used when there is available test data.

The polytropic coefficient, γ, in the gas compression law determines how the tem-

perature of the gas changes during compression. For static loading conditions with a steady rate of compression, such as taxiing or loading the aircraft, the process can be assumed to be isothermal (constant temperature) and a value of $\gamma = 1$ may be used. On the other hand, for dynamic loading conditions with a rapid rate of compression, such as landing, the process is assumed to be adiabatic (no heat transfer) and a value of $\gamma = 1.4$ may be used [19].

The length of the shock absorber s_m can be determined by considering the energy absorbed during the landing impact. This energy is the sum of the kinetic energy due to the vertical velocity at the instant of impact and the potential energy, which is equal to the product of the weight and the vertical displacement of the unit occurring over the period of time from the instant of impact to when the shock absorber and tire reach their maximum deflections. This analysis was performed by Howe [20] for fixed wing aircraft, where lift is equal to weight. However, it can be adapted for helicopters as shown in Equation 2.4, by setting lift equal to 2/3 of the weight as per CS 29.473(a), and simplifying the analysis by neglecting the relatively insignificant tire deformation [19].

$$s_m = \frac{V_S^2}{2g\eta\left(n_{LG} + L_f - 1\right)} \tag{2.4}$$

where V_S denotes the landing speed, g denotes the gravitational acceleration, n_{LG} denotes the *landing gear load factor* (the ratio of the maximum landing gear load to the weight on the landing gear), L_f denotes the *lift factor* (ratio of lift to weight) and η denotes the landing gear efficiency coefficient. A typical efficiency coefficient for this type of shock absorber is 0.8. The landing gear load factor can be typically chosen in the range of 2 to 2.5 for this class of helicopter. Finally, to account for potential errors in the design process, the calculated shock absorber length may be increased by 10% [21].

The minimum limit sink speed for a helicopter, as per CS 29.725, is 6.5 ft/s (2 m/s). However, in the design and analysis of landing gear, as well as in aircraft load related literature (such as [19, 20, 21, 22]), sink speeds of up to 10 ft/s (3 m/s) are commonly considered. In this study, a sink speed of 8.2 ft/s (2.5 m/s) was chosen as a compromise between these two values.

Similar to the modeling of the spring, the modeling of the damper can also be carried out using the simplified equation given below as suggested by Krüger and Moradini [18].

$$F_d = \begin{cases} c_c \dot{s}^2 & \dot{s} \geq 0 \\ -c_r \dot{s}^2 & \dot{s} < 0 \end{cases} \tag{2.5}$$

In Equation 2.5, the damper force F_d is expressed as a function of the shock absorber compression rate $\dot{s}$ and the viscous damping coefficients c_c and c_r for the compression and recoil phases, respectively. These coefficients, which are dependent on factors such as the density of the damper fluid and the hydraulic area [23], are typically larger for the recoil phase to prevent rebounding of the aircraft [19].

The damping coefficients and preload force values for a 6-ton class aircraft are typically obtained from various sources in the literature [22, 23, 24]. The shock absorber parameters are then determined using these values, and the shock absorber is modeled using the parameters shown in Table 2.1.

Table 2.1: Shock absorber spring and damper design parameters

Parameter	**Symbol**	**Value**	**Unit**
Sink speed	V_S	2.5 & 8.2	m/s & ft/s
Shock absorber efficiency	η	0.8	n.d.
Lift factor	L_f	2/3	n.d.
Landing gear load factor	n_{LG}	2	n.d.
Shock absorber length	s_m	25	cm
Preload force	F_0	6000	N
Correction factor	c_k	1	n.d.
Polytropic coefficient (isothermal)	γ	1	n.d.
Polytropic coefficient (adiabatic)	γ	1.4	n.d.
Damping coefficient (compression)	c_c	10000	N/m/s
Damping coefficient (recoil)	c_r	60000	N/m/s

The spring-damper properties of the resulting shock absorber model can be observed in Figure 2.5.

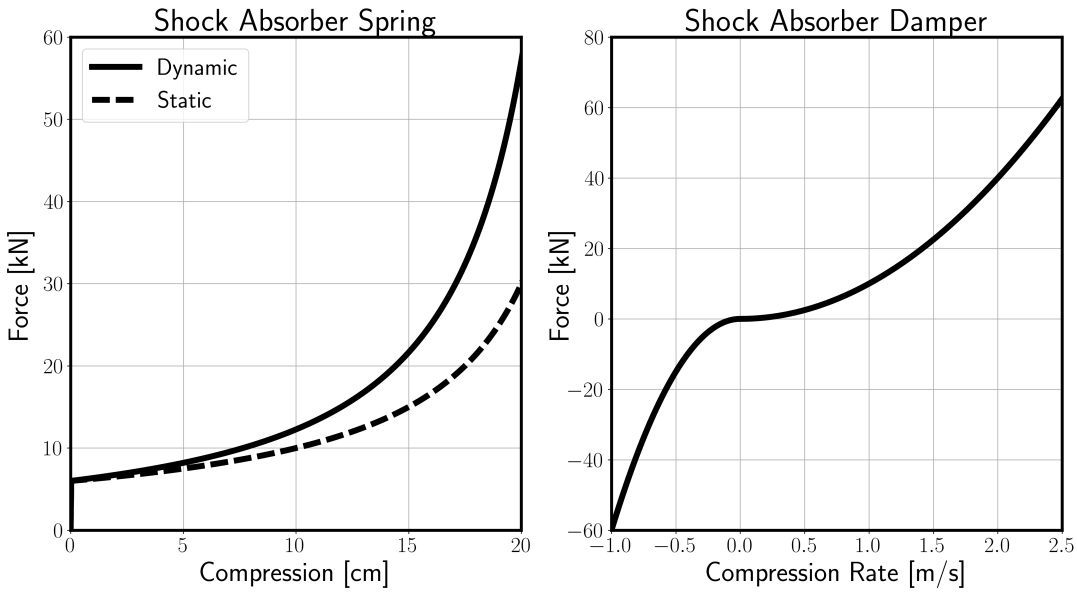


Figure 2.5: Spring and damper properties of MLG and NLG shock absorbers

Note that, in this study, the same set of parameters were applied to model the shock absorbers for both the NLG and MLG units.

In addition to the spring and damper forces generated in the shock absorber during landing, internal friction forces also contribute to the overall behavior of the system. However, these friction forces are proportional to the normal force acting on the landing gear strut [25], and as such can be neglected in this study, which primarily focuses on vertical, or *along* the strut, loading conditions.

2.1.1.2 Tires

In this study, a simplified model of the tires is utilized, as the primary focus is on vertical loading conditions. While it is important to accurately model tires in the analysis of ground dynamics due to their role in providing ground contact and support, and the various loads and deformations they undergo during takeoff, landing, and ground handling, this simplified approach is sufficient for the purposes of this work.

The wheel and tire combination has a high stiffness and low damping, which means it is not effective at dissipating energy during a heavy landing. The shock absorber,

with its lower stiffness and high inherent damping, is better equipped to absorb the energy and reduce the high sink rate to zero [26]. Therefore, the tire is modeled as a spring system with a stiffness coefficient k, neglecting its damping properties. In addition, although nonlinear in reality, tire stiffness can be approximated as linear [25], allowing the use of a constant stiffness coefficient for the tire. Then, the tire force can be calculated using Equation 2.6.

$$F_t = kd \tag{2.6}$$

where F_t is the tire force or ground reaction, k is the tire stiffness coefficient and d is the tire deflection. The tire stiffness coefficient is typically chosen from data available in literature, such as [20, 21, 22]. For this study, a value of 500 kN/m for the NLG tires and double that for the MLG tires were used. Resulting spring characteristics of both MLG and NLG tires are shown in Figure 2.6.

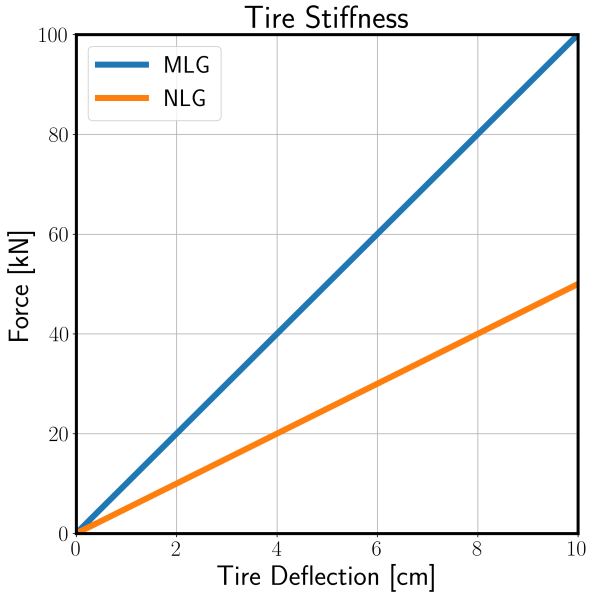


Figure 2.6: Stiffness properties of MLG and NLG tires

It should be noted that the NLG has two wheels as shown in Figure 2.3. This means that although the NLG tire stiffness is half that of the MLG, both landing gears effectively have the same tire stiffness due to the presence of two NLG wheels.

While tires are represented as springs in the analysis, their radii also play a significant role in the spin-up analysis discussed in Chapter 3.4. Reference helicopter data (Figure 2.1) was used to establish typical values for this class of helicopter, resulting

in a 25 cm MLG tire radius and 20 cm NLG tire radius.

2.1.1.3 Unsprung Mass

The combined mass of all components under the shock absorbers, including the moving parts of the shock absorber, tires, rims, brakes etc., is referred to as the unsprung mass. In this static analysis model, this mass is set to zero and as a result, the ground reaction acting on the tire is directly transferred to the helicopter's airframe.

2.2 Model B: Dynamic Analysis Model Without Rotor

In the previous chapter, a static analysis model (Model A) was presented which consisted of a single landing gear and a mass representing the helicopter. This chapter introduces Model B, a full scale helicopter model (albeit without a rotor) which will be used for dynamic analysis. The interactions between multiple landing gears and the airframe are taken into consideration in this model. The airframe is allowed to move freely in 6 directions, and each landing gear has 1 degree of freedom for shock absorber displacement and another degree of freedom for tire rotation. As a result, the model has a total of 13 degrees of freedom, as depicted in Figure 2.7.

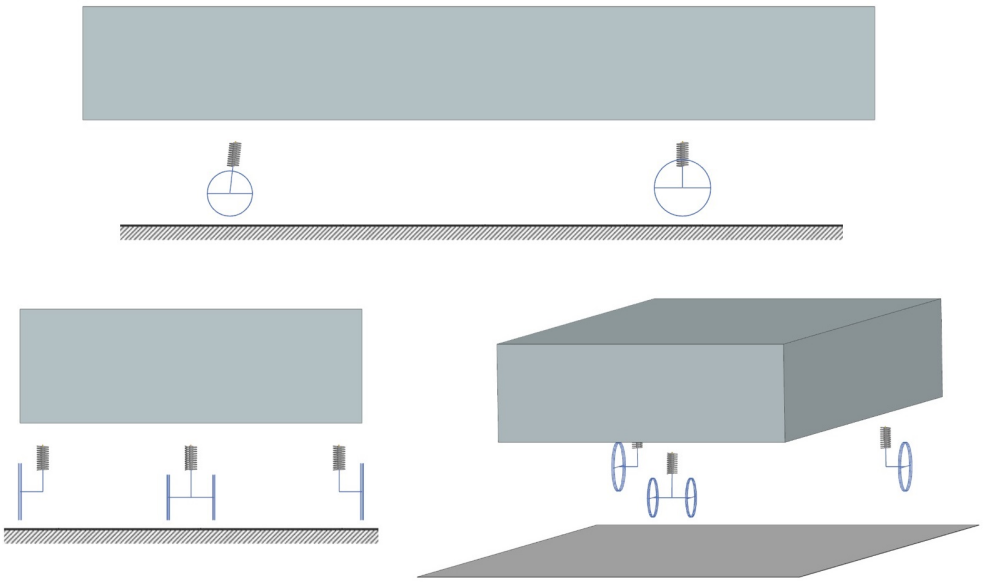


Figure 2.7: Side (top), front (left) and isometric (right) views of Model B

The airframe serves as the central hub for all components of the helicopter, such as the landing gears in the case of Model B. Measurements of loads are also taken at specific points on the airframe. Determining the CG location and placement of landing gears on the airframe are based on reference helicopters shown in Figure 2.1. The key dimensions pertaining to landing analysis are depicted in Figure 2.8.

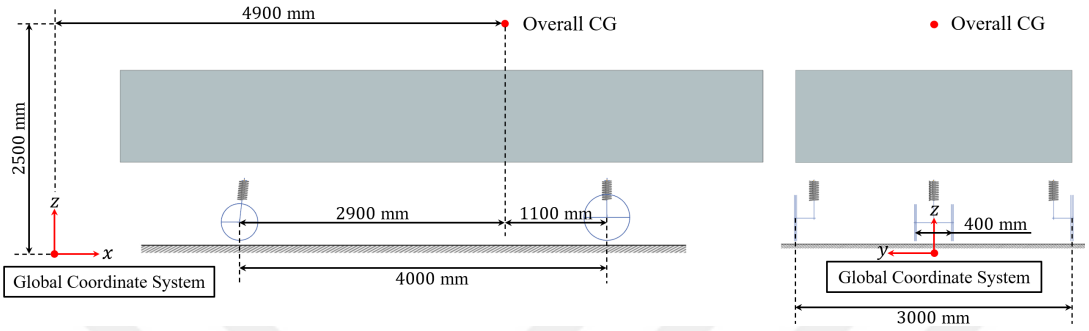


Figure 2.8: Dimensions of the airframe as seen in side (left) and front (right) views

Additionally, typical mass properties for this class of helicopter are used to represent the overall system, including the airframe and landing gears. The overall mass properties of Model B are shown in Table 2.2.

Table 2.2: Overall mass properties of the helicopter

Property	**Symbol**	**Value**	**Unit**	**Coordinate system**
Mass	m	6000	kg	N/A
CG-x	x_{cg}	4900	mm	Global
CG-y	y_{cg}	0	mm	Global
CG-z	z_{cg}	2500	mm	Global
Inertia-xx	I_{xx}	10000	kgm^2	Body
Inertia-yy	I_{yy}	30000	kgm^2	Body
Inertia-zz	I_{zz}	30000	kgm^2	Body
Inertia-xy	I_{xy}	0	kgm^2	Body
Inertia-xz	I_{xz}	-5000	kgm^2	Body
Inertia-yz	I_{yz}	0	kgm^2	Body

It should be noted that the mass moment of inertia terms in the table are given in the Body coordinate system, while the center of gravity location is given in the Global

coordinate system. Global coordinate system is a non-inertial reference frame that moves and rotates with the helicopter, with its origin located such that all components of the helicopter have positive x and z positions in this coordinate system and the xz plane is on the symmetry plane of the helicopter. Orientation of Global coordinate system can be seen in Figure 2.8.

In Model B, the landing gear models of Model A described in Chapter 2.1.1 are also utilized. However, unlike in Model A, the unsprung mass is not set to zero in Model B, as the analysis involves multibody dynamics where each body has its own mass properties. To determine the mass of the landing gear units, an empirical relation proposed by Schmidt [27] which is commonly used in the preliminary design of aircraft, as shown in Equation 2.7, was utilized.

$$m_{LG} = 62.61 \left(\frac{m}{1000}\right)^{0.84} \tag{2.7}$$

where m_{LG} denotes the total mass of the landing gears. Note that the given coefficients are valid if the unit of mass is pounds. Using Equation 2.7, the total landing gear mass for the 6 ton helicopter in this study is calculated to be 248 kg. According to Schmidt [27], the average weight of a complete landing gear system is approximately 4% of the aircraft's maximum weight, which also yields a value of 240 kg and is consistent with the result obtained from Equation 2.7. It is assumed that half of the total mass of the landing gear consists of non-moving parts or components that are not directly related to the dynamics of landing, such as those related to the retracting mechanism. The remaining mass is attributed to the wheels and shock absorbers. After rounding, this results in a total mass of 110 kg for these components. The mass breakdown of the individual landing gear components is presented in Table 2.3.

Table 2.3: Mass breakdown of individual landing gear components

Body	**Mass [kg]**
MLG shock absorber (each)	20
NLG shock absorber	10
MLG wheel (each)	20
NLG wheel (each)	10

The mass moment of inertia of the wheels, particularly around the axis of rotation, is significant for the spin-up analysis as discussed in Chapter 3.4. These values are calculated using Equation 2.8, which assumes the wheels to be disks with uniformly distributed mass.

$$I_w = \frac{1}{2} m_w r_w^2 \tag{2.8}$$

where I_w denotes the mass moment of inertia of the wheel around the axis of rotation, while m_w and r_w denote the mass and radius of the wheel. On the other hand, Mass moment of inertia components of the shock absorbers are neglected in this analysis.

The kinematic design of Model B, which includes the list of bodies and the types of joints connecting them, is an important aspect of the multibody dynamics analysis and is presented in Table 2.4.

Table 2.4: Kinematic details of Model B

Body 1	**Body 2**	**Joint Type**
Airframe	MLGL shock absorber	Slider
Airframe	MLGR shock absorber	Slider
Airframe	NLG shock absorber	Slider
MLGL shock absorber	MLGL wheel	Revolute
MLGR shock absorber	MLGR wheel	Revolute
NLG shock absorber	Left NLG wheel	Revolute
NLG shock absorber	Right NLG wheel	Revolute

Where MLGL and MLGR are left and right main landing gears, respectively.

2.3 Model C: Dynamic Analysis Model With Rotor

In this model, referred to as Model C, the full-scale helicopter model built as Model B is extended to include the components of the rotor. The type of rotor chosen for this model is an example of a fully articulated rotor, similar to the Airbus H160 helicopter's rotor as seen in Figure 2.9. The complete model, including the articulated rotor, is depicted in Figure 2.10.

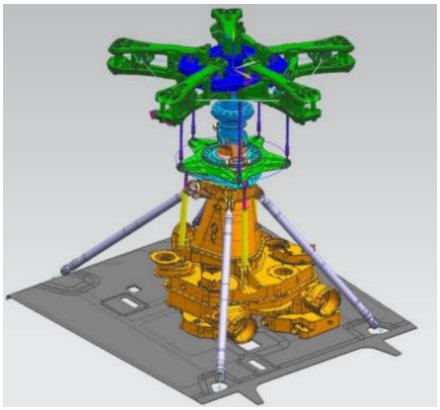


Figure 2.9: Schematic of Airbus H160 helicopter's main rotor [9]

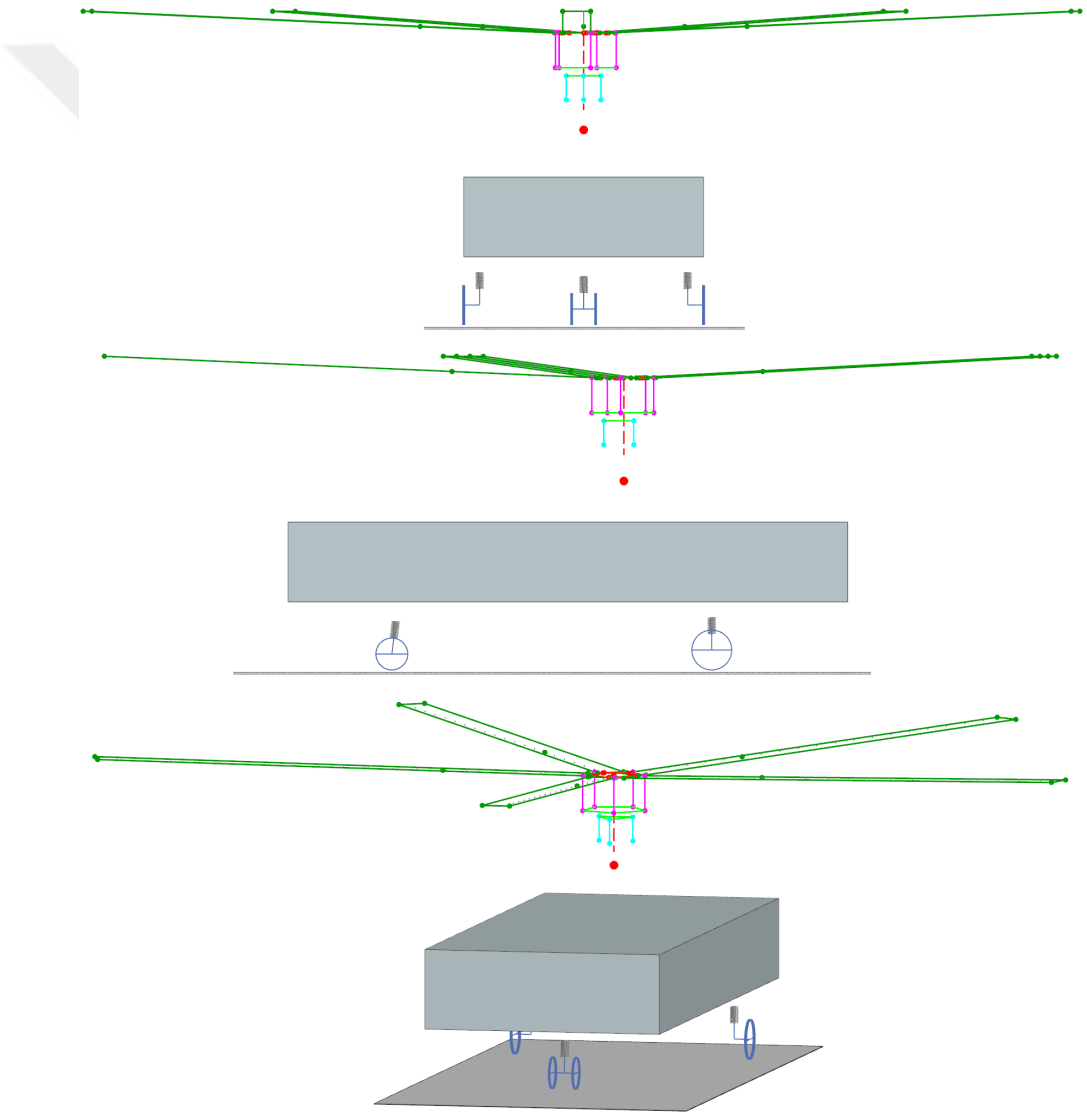


Figure 2.10: Front (top), side (middle) and isometric (bottom) views of Model C

In Model C, the airframe and landing gear models are the same as those in Model B. It should be noted that the CG of the overall system, depicted by the red dot in Figure 2.10, is positioned directly beneath the main rotor hub center. This simplifies the analysis, as the main rotor lift does not generate any moments around the center of gravity of the overall system. The components that make up the rotor and their numbers are listed in Table 2.5.

Table 2.5: Rotor components and their numbers

Body	**Number**
Rotor hub	1
Rotor shaft	1
Blade	5
Lead-lag damper	5
Pitch link	5
Rotating swashplate	1
Non-rotating swashplate	1
Actuator	3

Figure 2.11 provides a more detailed illustration of the components of the rotor.

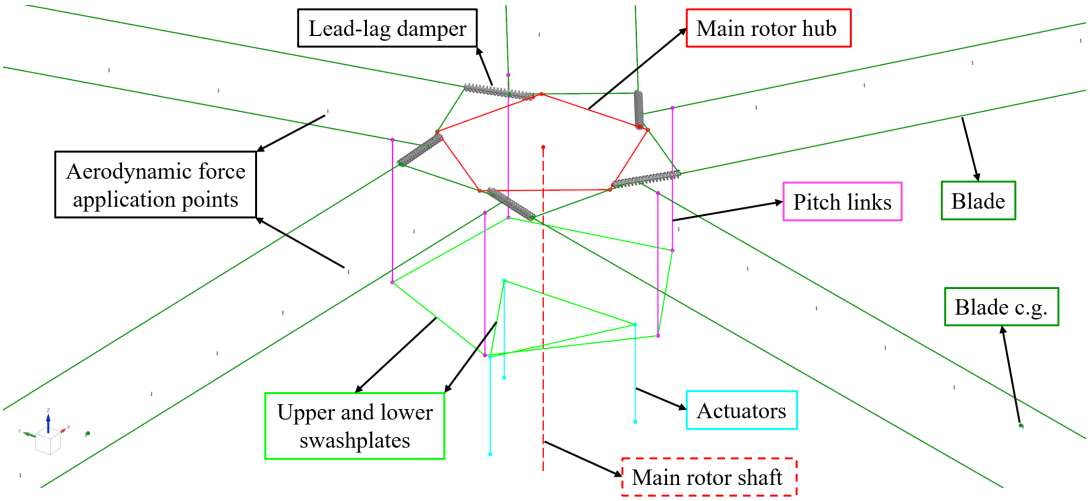


Figure 2.11: Isometric view of the rotor model components

In order to accurately determine the loads transmitted between the rotor components and to establish the load paths from the blades to the airframe of the helicopter, it

is necessary to have a correct kinematic design. The kinematic design is completed through the list of joints connecting the objects, which is provided in Table 2.6.

Table 2.6: Kinematic details of the rotor model

Body 1	**Body 2**	**Joint Type**	**Number**
Shaft	Airframe	Revolute	1
Hub	Shaft	Fixed	1
Blade	Hub	Spherical	5
Blade	Lead-lag damper	Spherical	5
Blade	Pitch link	Spherical	5
Lead-lag damper	Hub	Spherical	5
Pitch link	Rotating swashplate	Spherical	5
Rotating swashplate	Non-rotating swashplate	Revolute	1
Non-rotating swashplate	Actuator	Spherical	3
Actuator	Airframe	Spherical	3

To find the total degree of freedom (DOF) of the system, *Kutzbach-Grübler* formula given in Equation 2.9 is used.

$$\text{DOF} = 6n - (6j_0 + 5j_1 + 4j_2 + 3j_3 + 2j_4 + j_5) \tag{2.9}$$

where n is the number of movable rigid bodies and the variable j_k represents the number of joints in the system, each of which has k degrees of freedom. These joints allow k independent relative motions between the connected rigid bodies, which reduces the total number of degrees of freedom in the system by $(6 - k)$. In this case, Model C is determined to have 36 degrees of freedom.

In the model, all components are treated as rigid, with the exception of certain joints that are modeled as elastic in order to avoid statically indeterminate situations. High stiffness coefficients are applied to these elastic joints, with the exception of the spherical joint that connects the rotor hub and blade.

The spherical joint that connects the rotor hub and blade, known as a elastomeric bearing, plays a crucial role in the rotor's dynamics. The stiffness and damping co-

efficients of the bearing and the lead-lag damper, as well as parameters such as the blade's weight and moment of inertia, the rotor's radius, and the rotational speed are entered as typical values. Parameters of the rotor model are listed in Table 2.7.

Table 2.7: Rotor model design parameters

	Parameter	**Value**	**Unit**
General	Rotor angular speed	320	RPM
	Rotor radius	6500	mm
	Tip speed	217.8	m/s
	Lock number	7.22	n.d.
	Hinge offset	300 & 4.6%	mm & n.d.
	Torque offset	30 & 0.46%	mm & n.d.
Blade (each)	Span	6200	mm
	Chord (constant)	35	cm
	Mass	100	kg
	CG station	1860 & 30%	mm & n.d.
	First moment of mass	186	kgm
	Flap inertia	666	kgm^2
	Linear twist	1.61	°/m
Elastomeric bearing	Flap stiffness	1200	Nm/rad
	Lag stiffness	1200	Nm/rad
	Pitch stiffness	400	Nm/rad
Lead-lag damper	Stiffness	1000	kN/m
	Damping	50	kN/m/s

Lock number, γ, is a dimensionless parameter that represents the ratio of aerodynamic forces to inertial forces in the blade of a rotor. This parameter plays a crucial role in the flap dynamics of the rotor, as the damping of the flapping motion exhibits a strong dependence on Lock number [28]. It is given as:

$$\gamma = \frac{\rho a c R^4}{I_\beta} \tag{2.10}$$

where ρ denotes the air density, a denotes the lift curve slope of the blade airfoil, c denotes the chord length of the blade, R denotes the radius of the rotor, and I_β denotes

the flap inertia of the blade. Typically, Lock number for articulated rotors falls in the range of 6 to 10 according to Johnson [29]. In the model, the air density is taken as 1.225 kg/m^3 and the lift curve slope is taken as 2π, resulting in a Lock number of 7.22, which is within the typical range.

In contrast to models A and B, the lift force is not applied on the CG of the helicopter, but rather a distributed lift force is applied to the blades in this model. This distribution of force is determined by developing an aerodynamic model for the rotor, as detailed in the subsequent subchapter.

2.3.1 Rotor Aerodynamic Model

A blade element theory (BET) model with an appropriate level of complexity for this study is developed to analyze the distribution of aerodynamic forces acting on the blade. BET is a widely utilized methodology in contemporary analyses of helicopter rotor aerodynamics, as it facilitates the estimation of the radial and azimuthal distributions of aerodynamic loads acting on the rotor disk. BET is predicated on the assumption that each section of the blade behaves as a quasi-2D airfoil, thereby generating aerodynamic forces and moments. The overall rotor loads can be obtained by integrating the sectional airloads at each blade element over the length of the blade and averaging the result over a rotor revolution [30]. Figure 2.12 illustrates a diagrammatic representation of the flow environment and aerodynamic forces at a representative blade element on the rotor.

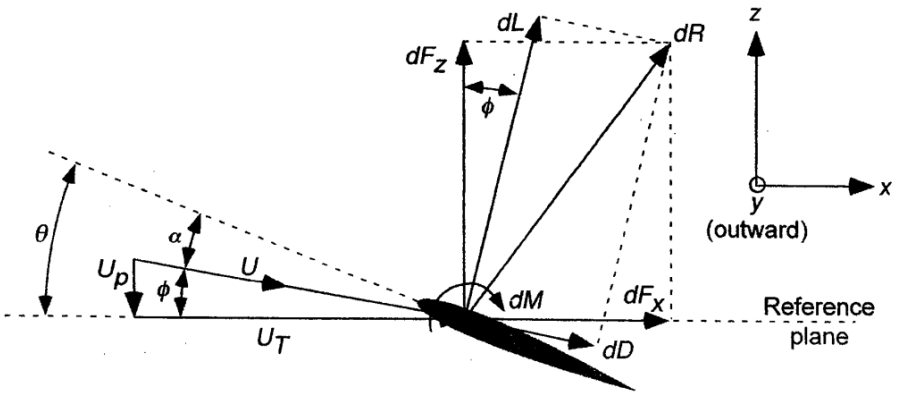


Figure 2.12: Velocities, angles and forces on a typical blade element [30]

The resultant air velocity acting on the blade, U, is the vector sum of the velocities perpendicular (U_P) and tangential (U_T) to the reference plane. In the present analysis, which examines a vertical descent case, the tangential velocity component is solely composed of the blade's rotational speed, as represented by Equation 2.11.

$$U_T = \Omega \left[eR + (r - eR) \cos \beta \right] \tag{2.11}$$

Where, Ω is the angular velocity of the rotor, e is the nondimensional hinge offset, β is the flapping angle, and r is the radial location of the blade element along the blade span, with the constraint $eR \leq r \leq R$.

On the other hand, the perpendicular velocity component, U_P, is comprised of three distinct contributions: the induced velocity, v_i, of the rotor as it displaces air downwards, the component arising from the sink speed of the helicopter, and the angular speed due to flapping rate, $\dot{\beta}$, as shown in Equation 2.12.

$$U_P = v_i \cos \beta - V_S + \dot{\beta} \left(r - eR \right) \tag{2.12}$$

As a steady descent analysis is performed in this study, the flapping angle, β, is assumed to be constant until touch down occurs. Therefore, the angular speed due to flapping rate, $\dot{\beta}$, is set to zero prior to touchdown.

In the present study, the induced velocity component is determined using a uniform inflow model. For a rotor in a descent scenario, v_i is represented by Equation 2.13, as proposed by Leishman [30].

$$\frac{v_i}{v_h} = \begin{cases} \kappa - \left(\dfrac{3}{4} \right) \dfrac{V_c}{v_h} & \dfrac{-8\kappa}{4\kappa + 1} \leq \dfrac{V_c}{v_h} \leq 0 \\ \\ \kappa \left(7 + 3 \dfrac{V_c}{v_h} \right) & -2 \leq \dfrac{V_c}{v_h} < \dfrac{-8\kappa}{4\kappa + 1} \end{cases} \tag{2.13}$$

Where v_h is the induced velocity in hover, κ is the *induced flow correction factor*, and V_c is the climb speed, with positive direction indicating upward motion. In the model, κ is taken to be 1.15 as a typical value and V_c is set to the negative of the sink speed, $-V_S$. In the momentum theory, the induced velocity in hover, v_h, is given by:

$$v_h = \sqrt{\frac{T}{2\rho A}} \tag{2.14}$$

Where T is the total thrust of the rotor, which is calculated as 2/3 of the weight of the helicopter for this study, and A is the rotor disk area.

To proceed with the computation of the aerodynamic load acting on the blade element, the angle of attack of the flow must be determined. As illustrated in Figure 2.12, the angle of attack, α, is represented as:

$$\alpha = \theta - \phi \tag{2.15}$$

Where θ is the local pitch angle of the blade, and ϕ is the inflow angle attack, which can be derived geometrically as:

$$\phi = \tan^{-1}\left(\frac{U_P}{U_T}\right) \tag{2.16}$$

The pitch angle of the blade, θ, is a function of both the pilot's input and the twist of the blade, and it is represented as:

$$\theta = \theta_0 - \theta_{1c}\cos\psi - \theta_{1s}\sin\psi - \theta_{tw}\frac{r}{R} \tag{2.17}$$

Where θ_0, θ_{1c}, θ_{1s} are the collective, lateral cyclic and longitudinal cyclic inputs, respectively and θ_{tw} represents the twist distribution of the blade, and ψ is the azimuth angle of the blade.

In this study, the effect of the tail rotor on the landing problem is assumed to be insignificant, and thus it is not modeled. Additionally, the CG of the overall system is positioned directly beneath the main rotor hub, resulting in no moments generated by the rotor lift. Furthermore, as the helicopter has no forward speed, the rotor forces generated will be azimuthally symmetric. Therefore, the longitudinal and lateral cyclic inputs are set to zero, and only the collective input is applied to the rotor, yielding an azimuthally symmetric force distribution. Consequently, Equation 2.17 is simplified as:

$$\theta = \theta_0 - \theta_{tw}\frac{r}{R} \tag{2.18}$$

In this study, an ideal airfoil is modeled, which is adequate for the purposes of this study. The lift and drag coefficients of this ideal airfoil are represented by:

$$C_l = \alpha a \tag{2.19a}$$

$$C_d = C_{d_0} + \frac{C_l^2}{\pi e_0 \,\mathrm{AR}} \tag{2.19b}$$

Where C_{d_0} is the zero-lift drag coefficient, assumed to be 0.01, e_0 is the Oswald's efficiency factor, set as 0.75, and AR is the aspect ratio of the blade.

In the model, tip losses are also taken into account by utilizing Prandtl's tip loss function, F, which is given by Shen [31] as shown in Equation 2.20.

$$F = \frac{2}{\pi}\cos^{-1}\left[\exp\left(-\frac{N_b(R-r)}{2R\sin\phi_R}\right)\right] \tag{2.20}$$

Where N_b is the number of blades and ϕ_R is the local inflow angle. As the model employs a uniform and perpendicular to rotor disk inflow model, the local inflow angle is equivalent to the blade flapping angle.

$$\phi_R = \beta \tag{2.21}$$

Finally, the differential lift and drag forces on a differential blade element are calculated as:

$$dL = \frac{1}{2}\rho\left(U_T^2 + U_P^2\right)c\,C_l F\,dr \tag{2.22a}$$

$$dD = \frac{1}{2}\rho\left(U_T^2 + U_P^2\right)c\,C_d\,dr \tag{2.22b}$$

Again, by using the geometry presented in Figure 2.12, the lift and drag forces are resolved into forces perpendicular and parallel to the reference frame, as shown in the following equations:

$$dF_Z = dL\cos\phi - dD\sin\phi \tag{2.23a}$$

$$dF_X = dL\sin\phi + dD\cos\phi \tag{2.23b}$$

It should be noted that F_Z is the force perpendicular to the blade's reference frame and not equal to the thrust force, which is perpendicular to the rotor hub plane. The total thrust force generated by all the blades combined can be calculated as:

$$T = N_b\cos\beta\int_{eR}^{R} F_Z\,dr \tag{2.24}$$

Thus far, the only unknowns in the analysis are θ_0 and β. To determine β, the free body diagram of the blade, as depicted in Figure 2.13, is considered.

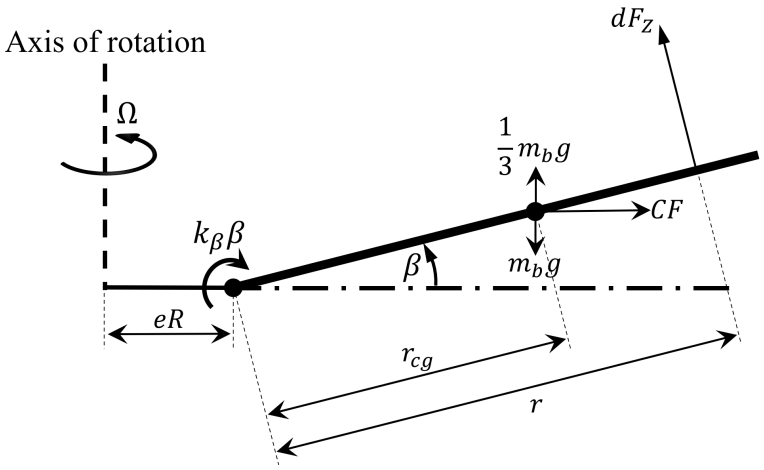


Figure 2.13: Free body diagram of the blade in the rotating non-inertial frame

As depicted in the free body diagram, the blade is under the influence of weight and aerodynamic forces. Additionally, as the free body diagram is drawn in a rotating non-inertial frame, the blade experiences inertial forces consisting of centrifugal (CF) and linear acceleration forces. The moment equation about the flapping hinge results in a non-linear expression in terms of β as shown in Equation 2.25.

$$k_\beta\beta + \frac{2}{3}m_b g r_{cg}\cos\beta + m_b\Omega^2\left(eR + r_{cg}\cos\beta\right)r_{cg}\sin\beta = \int_{eR}^{R} F_Z r dr \qquad (2.25)$$

Where k_β is the flap stiffness of the elastomeric bearing. As a result of the dependency of F_Z on β, a closed-form solution for β cannot be obtained. Therefore, a numerical solution procedure is implemented to simultaneously determine both β and the aerodynamic force distributions on the blade. This approach also includes iterating the collective input until the desired thrust is achieved, and until convergence of β is achieved. The procedure is demonstrated in Figure 5 as a flowchart 2.14.

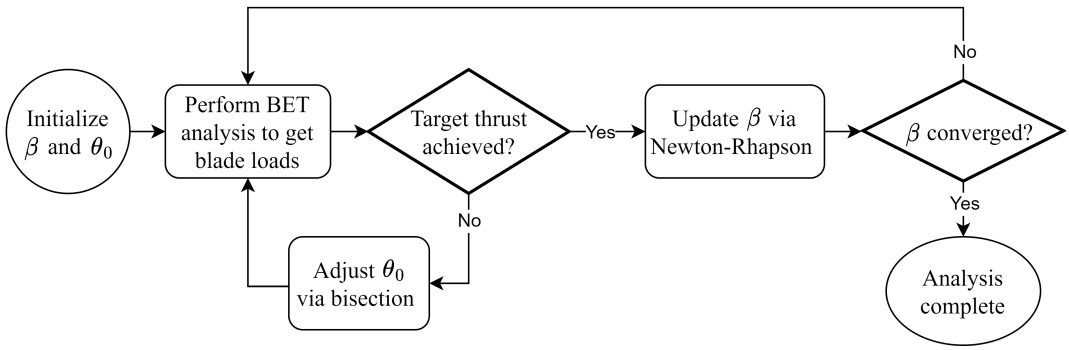


Figure 2.14: Flowchart for the solution procedure of collective and flapping angles

The flowchart demonstrates the procedure for performing the BET analysis, which produces the sectional incidence angles, flow velocities, and aerodynamic forces. These results are illustrated in Figures 2.15 to 2.18, providing a comprehensive understanding of the forces acting on the blades during descent portion of the landing analysis.

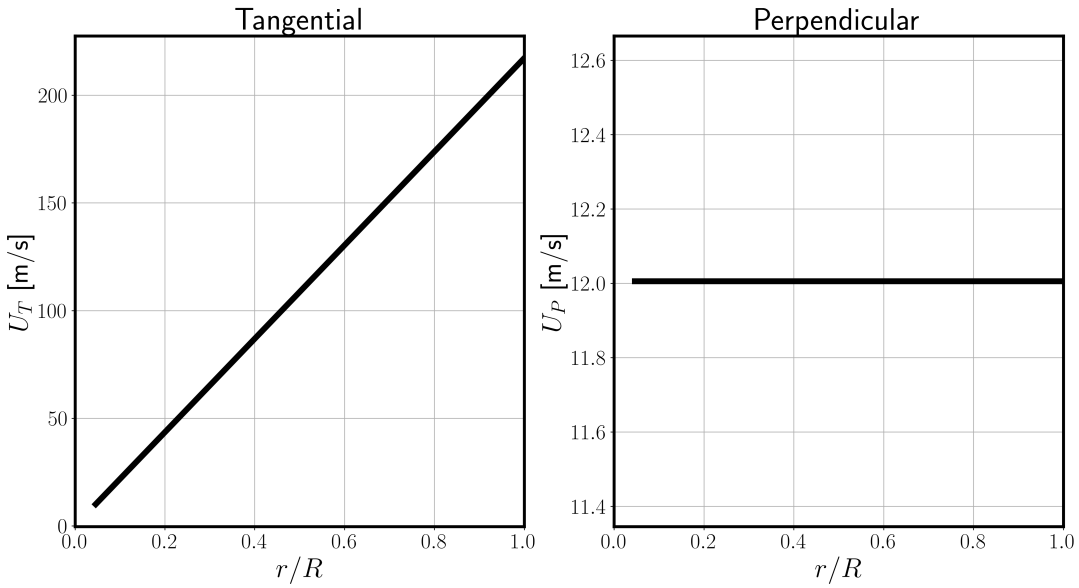


Figure 2.15: Sectional tangential and perpendicular velocities on the blade

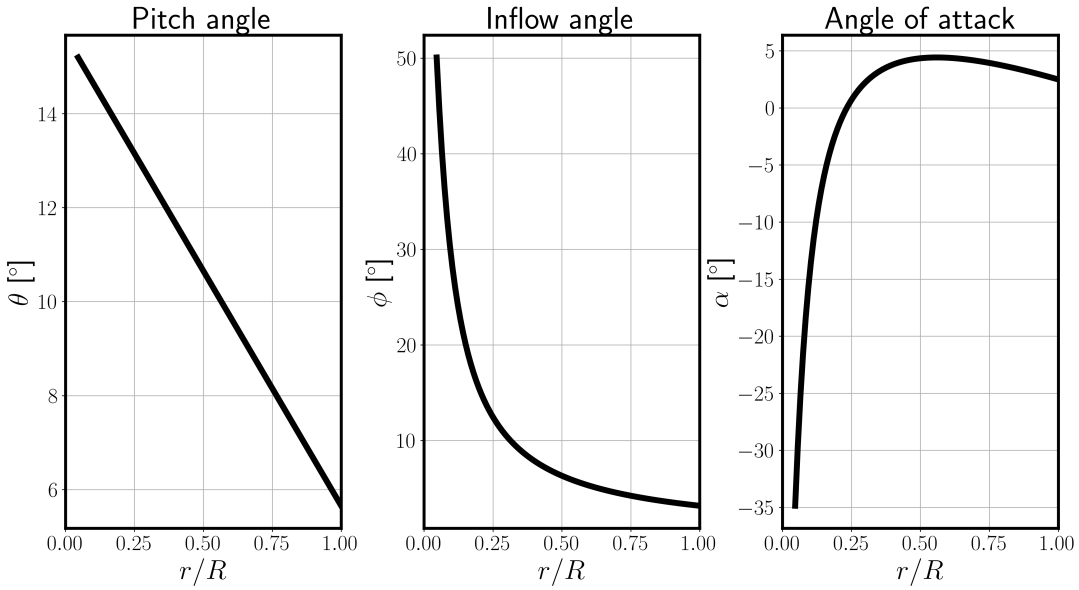


Figure 2.16: Sectional incident angles on the blade

As a uniform inflow model is employed, the perpendicular velocity component remains constant while the tangential velocity component, which is dependent on both the angular speed and the radial position, linearly increases along the blade as can be seen in Figure 2.15.

At the blade sections that are close to the hub, the contribution of perpendicular velocity to the resultant velocity is significant, as the tangential speed due to rotation is low at these sections. This results in a very large inflow angle and consequently, the angle of attack is very large in the negative direction at these sections, as illustrated in Figure 2.16. The lift and drag coefficients resulting from this distribution of angle of attack are presented in Figure 2.17.

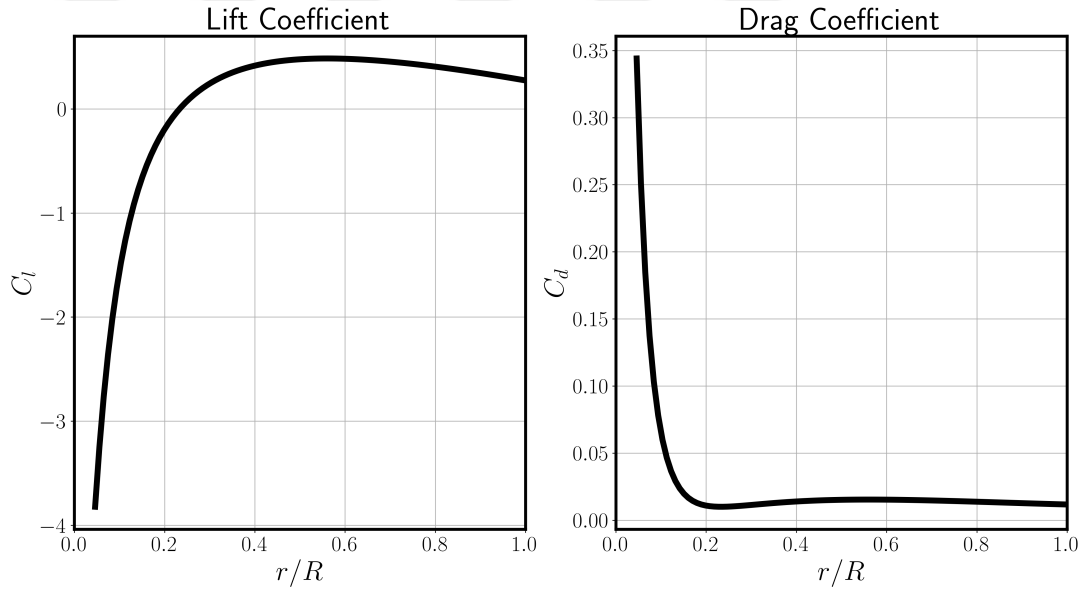


Figure 2.17: Sectional lift and drag coefficients on the blade

It should be noted that the linear model used, as shown in Equation 2.19, results in unphysical values for the lift coefficient at the blade sections closest to the hub. However, as the speed is low at these sections, the contribution of the aerodynamic forces generated at these sections to the overall force is insignificant and this approach can be considered acceptable.

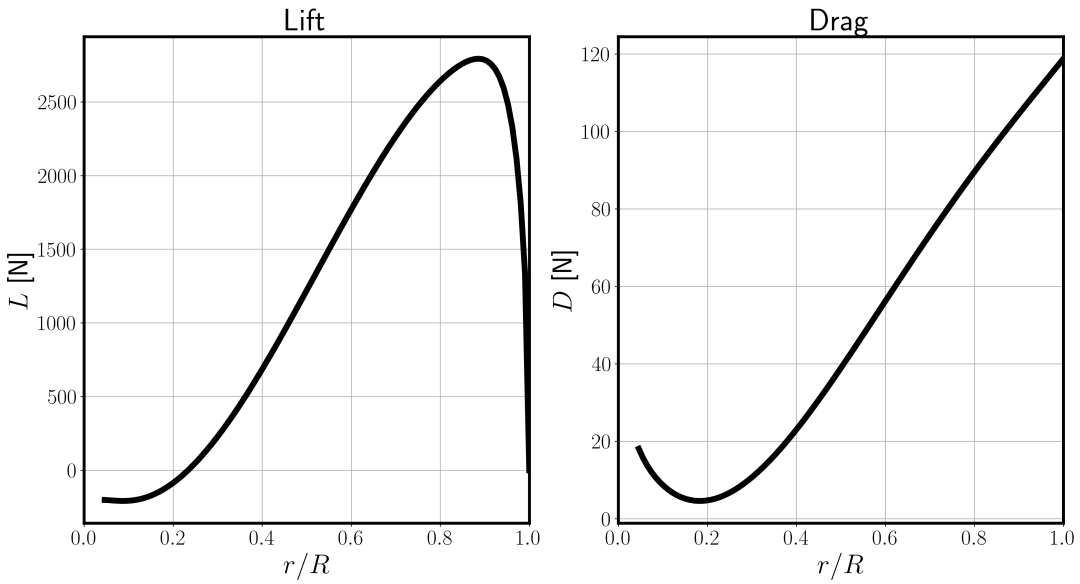


Figure 2.18: Lift and drag distributions on the blade

Finally, the lift and drag distributions along the blade are obtained as depicted in Figure 2.18. As can be observed, the forces generated at the sections closest to the hub are indeed insignificant when compared to the sections close to the tip of the blade. The effect of the Prandtl's tip loss function is also evident in the sharp decrease in lift towards the tip of the blade.

It is important to note that the results presented thus far pertain to the descent phase of the landing, prior to touch down. Upon touch down, the blades will experience a dynamic flapping motion, resulting in a non-uniform perpendicular velocity distribution along the blade as described by Equation 2.12. This leads to a change in inflow angle, angle of attack and ultimately lift distribution along the blade. Therefore, the study also includes an examination of the aerodynamic damping present in the flapping degree of freedom of the blades during the landing.

The lift distribution across the blade span for various values of the flapping rate, $\dot{\beta}$, are displayed in Figure 2.19 for reference purposes.

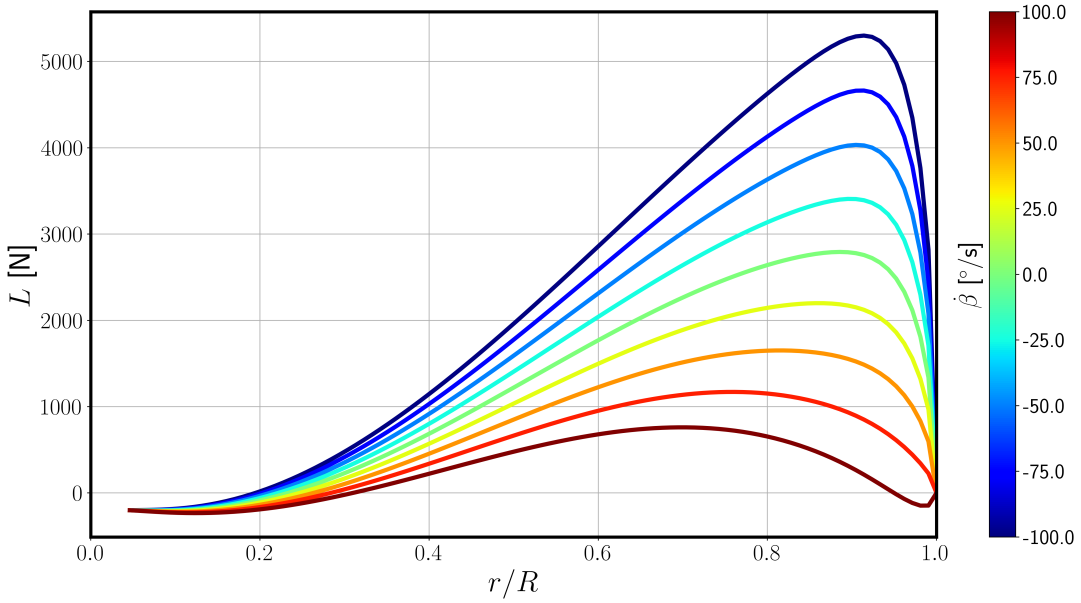


Figure 2.19: Lift distribution across the blade span for different flapping rates, $\dot{\beta}$

As the flap rate increases, the lift acting on the blade decreases due to the alteration of air flow direction on the blade towards the suction side of the airfoil, resulting in a decrease in angle of attack and therefore lift. Conversely, as the blade flaps downward, the effective angle of attack at each blade section increases, leading to an increase in lift. This mechanism serves to dampen the flapping motion of the blade and promote stability by exerting increased force during downward flapping and decreased force during upward flapping.

CHAPTER 3

METHOD

In this chapter, four primary landing conditions that were considered for the analysis of the models described in Chapter 2, are presented and explained in detail. The following section presents a brief overview of the four landing conditions under consideration.

- **3-point landing:** The helicopter lands on a level ground with a level attitude, with all its three wheels contacting the ground simultaneously, performing the maneuver with only vertical speed.
- **Tail-down landing:** The helicopter lands on a level ground with a pitch-up attitude, its main wheels contacting the ground simultaneously and the nose wheel clear of the ground and with vertical speed only.
- **Lateral slope landing:** The helicopter lands with a level attitude on a laterally inclined surface, with one of its main wheels contacting the ground and the other wheels clear of the ground, performing the maneuver with vertical speed only.
- **Running landing:** The helicopter lands with a forward and vertical speed, maintaining a level attitude, all its three wheels contacting the ground simultaneously on a level ground.

While other landing maneuvers, such as *lateral drift*, are considered in the certification standards, the four conditions described in this chapter provide a comprehensive understanding of the fundamental principles and dynamics involved in helicopter landings. It is worth noting that although lateral slope landing is not included in the

certification standards, its physics are highly similar to that of *one-wheel* landing which is included in the standards. Additionally, when examining the various load cases needed for certification, they can be broadly categorized into two types: *book-case* and *rational*. A bookcase load case involves an artificial state of the helicopter, where applied and inertia loads are balanced, whereas a rational load case involves modeling and simulating the helicopter's dynamic behavior as accurately as possible [19]. Accordingly, this thesis focuses on investigating rational landing types, which are physical.

In all landing analyses, the sink speed of the helicopter at the moment of touch down is fixed at 8.2 ft/s (2.5 m/s) and the lift force is equal to 2/3 of the helicopter's weight in accordance with the regulations outlined in CS-29.473(a). To simulate the landing process, the helicopter is dropped from a predetermined height, referred to as the drop height. The drop height is calculated using the principle of conservation of energy, as depicted in equation 3.1, to ensure that the helicopter's vertical speed at the moment of touch down is equal to the predetermined sink speed. During the drop, the helicopter experiences the forces of both gravity and lift.

$$\frac{1}{2}mV_S^2 = mg(1 - L_f \cos\theta)h \tag{3.1}$$

where m is the mass of the helicopter, V_S is the sink speed of the helicopter, g is the gravitational acceleration, L_f is the *lift factor* (ratio of lift to weight), θ is the helicopter's pitch angle and h is the drop height. Solving Equation 3.1 for the drop height, it is found as:

$$h = \sqrt{\frac{V_S^2}{2g(1 - L_f \cos\theta)}} \tag{3.2}$$

The pitch angle θ is included in the equations as the lift acts perpendicular to the helicopter's reference plane, rather than being perpendicular to the ground.

In all landing analyses, the forward speed is set to zero, with the exception of the running landing analysis. The forward velocity used in the running landing analysis is set at 75% of the optimal forward flight velocity for the minimum descent rate in autorotation, as specified in CS-29.479(3)(i). This value has been established through the examination of two sample helicopters with maximum takeoff weights comparable to the helicopter model under study, as conducted by Leishman [30] and Prouty

[32]. These analyses, illustrated in Figure 3.1, have determined that the optimal forward velocity for minimum descent rate in autorotation is approximately 70 knots, thus the forward velocity in the running landing analysis is set at 50 knots (25.7 m/s).

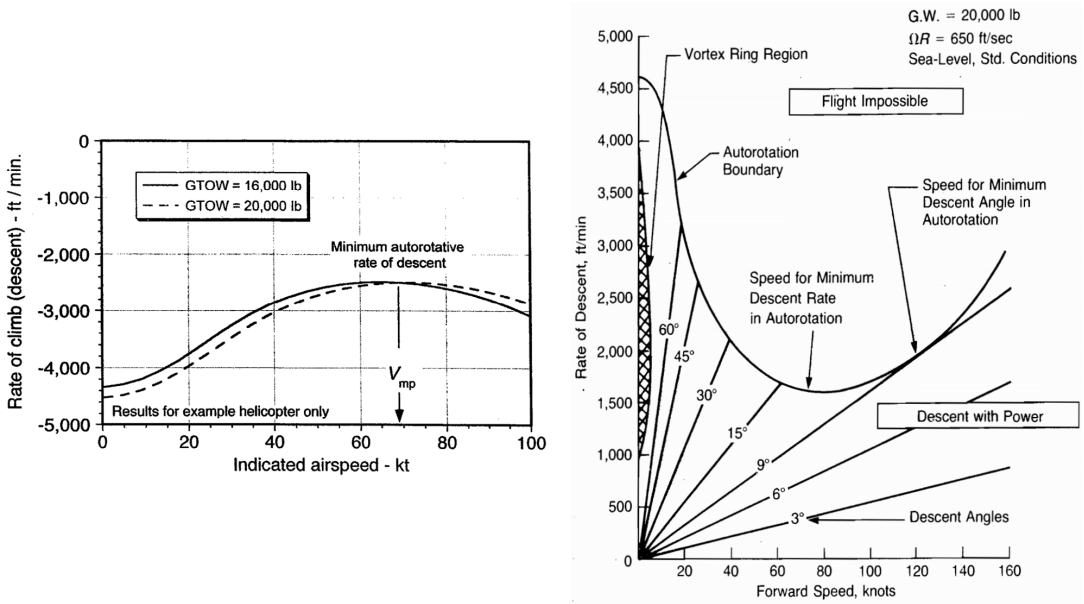


Figure 3.1: Minimum rate of descent in autorotation studies of Leishman [30] (left) and Prouty [32] (right) on example helicopters

To provide a clear and concise summary of the landing analyses and their respective conditions, the following table presents an overview of the parameters used in each analysis.

Table 3.1: Summary of key landing parameters by maneuver

Maneuver	**Pitch** [°]	**Sink speed** [ft/s]	**Forward speed** [kts]	**Lift factor** [n.d.]	**CS article**
3-point	0	8.2	0	2/3	29.479(b)(1)
Tail-down	15	8.2	0	2/3	29.481
Lateral slope	0	8.2	0	2/3	29.483 [1]
Running	0	8.2	50	2/3	29.479(b)(3)

[1] 29.483 refers to one-wheel, but also applies to lateral slope as the physics are comparable

In all the analyses, a comprehensive set of parameters are recorded during the time it takes for the helicopter to reach a static position. These parameters include the

ground reactions, shock absorber displacements and rates, tire deflections, Euler angles, linear and angular velocities and accelerations of all the bodies, as well as the helicopter's center of mass. For analyses with Model C, additional rotor dynamics outputs such as flapping angles and rates of the blades, total aerodynamic force acting on the blades, and loads transmitted by the rotor to the fuselage are also examined.

In addition to the helicopter's center of mass, two specific points, located on the nose and tail sections on the airframe were selected for analysis. These points, which are furthest away from the center of mass of the helicopter, were chosen as the effects of angular acceleration and angular velocity on them, as per Equation 2.1, are the greatest. This allows for the examination of effects of angular velocities and accelerations on the airframe loads. Positions of these points in the body coordinate system with the origin at the center of mass of the helicopter are detailed in Table 3.2.

Table 3.2: Positions of the selected monitor stations in Body coordinate system

Station	**Coordinate in Body frame [mm]**		
	x	y	z
Nose	3900	0	1000
Tail	-5100	0	-500

Acceleration at the specified points on the nose and tail, as well as at the center of gravity of the helicopter, can be used as a reliable metric for assessing the loads on the airframe. This is because acceleration can be treated as a specific force per unit mass, and thus the accelerations at these points can be used as a representative measure of the loads acting on the airframe. This information is crucial for understanding the dynamic behavior of the helicopter and for designing the airframe to withstand the loads it will experience during landing, as it allows for a direct quantification of the loads acting on the airframe.

The specific analysis methods for each landing maneuver will be discussed in the following subchapters.

3.1 3-Point Landing

In a typical helicopter landing scenario, various factors such as the rolling moment generated by the tail rotor's thrust, misalignment of the center of gravity with the rotor, and moments imparted by the main rotor due to non-neutral longitudinal or lateral cyclic inputs may result in an attitude that deviates from a level position. However, for the purposes of this study and also as described in the certification standards, an idealized scenario is considered in which the helicopter maintains a level attitude prior to touchdown and all three of its wheels make simultaneous contact with the ground.

To simulate this landing maneuver in the static analysis model, Model A, the separate and independent NLG and MLG models are released from the specified drop height under the influence of gravity and lift forces, as shown in Figure 3.2.

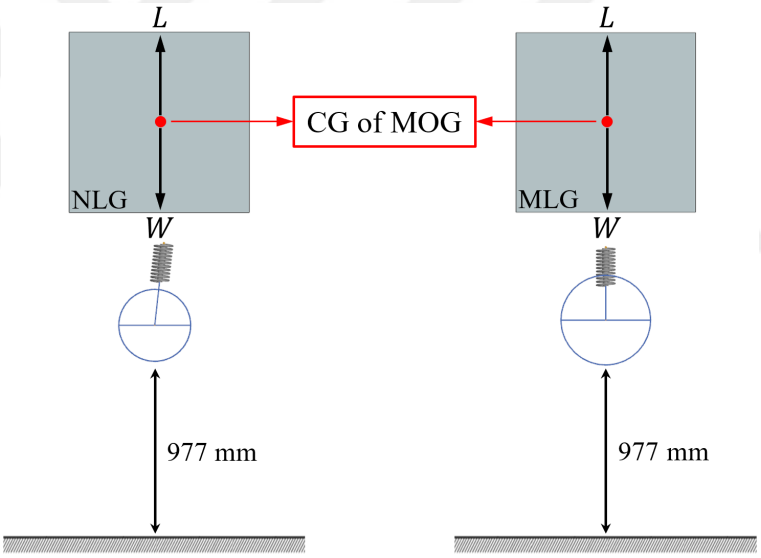


Figure 3.2: Side view of 3-point landing analysis with Model A

As these models only include a single landing gear, it is necessary to determine the values of MOG for both MLG and NLG, which represent the portion of the helicopter's mass over each gear. While MOG can be calculated through simple hand calculations based on the static position of the helicopter on the ground, in this study, it is determined using Model B, which accounts for the compression of the tires and shock absorbers. The MOG values for the helicopter in this study are presented in Table 3.3.

Table 3.3: MOG values for Model A in 3-point landing

Landing gear	**MOG [kg]**
NLG	1634
MLGL	2183
MLGR	2183

It is important to note that in Model A, the motion of the MOGs is restricted to vertical translation only. As a result, the ground reaction forces do not generate any moments and only act in the vertical direction. In this static analysis method, once the time histories of the ground reactions on the MLG and NLG wheels are obtained, only their maximum values are utilized and applied to the overall helicopter using Newton's Second Law, as represented in Equation 3.3. Thus, by neglecting the time histories, a single value, as opposed to time-varying values, is obtained in the analyses with Model A.

$$\vec{a} = \frac{1}{m}\left(\vec{F}_{\text{NLG}} + \vec{F}_{\text{MLGL}} + \vec{F}_{\text{MLGR}} + m\vec{g}\right) \tag{3.3}$$

In a similar manner, the angular accelerations can be determined by applying the forces obtained in the 2 DOF analysis with Model A to the overall 6 DOF helicopter and disregarding the angular velocities in the analysis, as shown in Equation 3.4.

$$\vec{\alpha} = \hat{I}^{-1}\left(\vec{r}_{\text{NLG}} \times \vec{F}_{\text{NLG}} + \vec{r}_{\text{MLGL}} \times \vec{F}_{\text{MLGL}} + \vec{r}_{\text{MLGR}} \times \vec{F}_{\text{MLGR}}\right) \tag{3.4}$$

Where, the inertia matrix $\hat{I}$ and the position vectors $\vec{r}_i$ are given in Chapter 2.2. After the linear and angular accelerations of the overall system have been determined, the accelerations at the monitor stations at the nose and tail locations are then calculated using Equation 2.2, thus completing the analysis with Model A.

In the dynamic analysis model without the rotor, Model B, the 3-point landing analysis is conducted by releasing the helicopter from the specified drop height under the influence of gravity and lift forces, as shown in Figure 3.3.

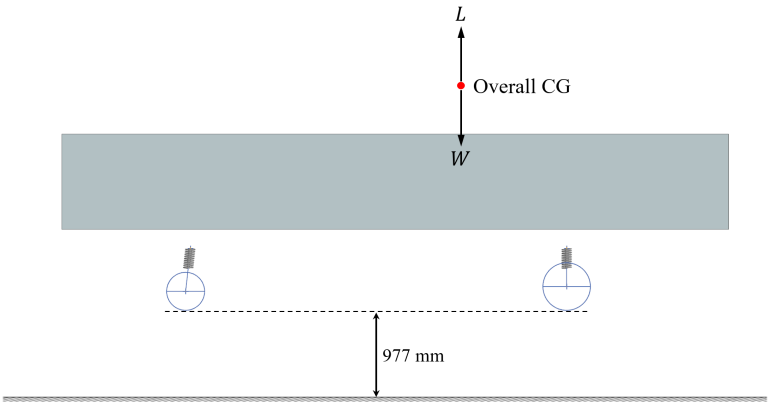


Figure 3.3: Side view of 3-point landing analysis with Model B

As depicted, the lift force is applied to the center of gravity of the helicopter, and its magnitude remains constant throughout the simulation. It is important to note that the line of action of the lift force is aligned with the z-axis of the helicopter's body frame, rather than being perpendicular to the ground. During the dynamics analysis, the simulation results, such as ground reactions, linear and angular accelerations, are recorded over time until the helicopter reaches a stable position on the ground.

In the Model C, in contrast to Model B, a distributed lift force is applied to each blade, accounting for one-fifth of the total lift, as depicted in Figure 3.4.

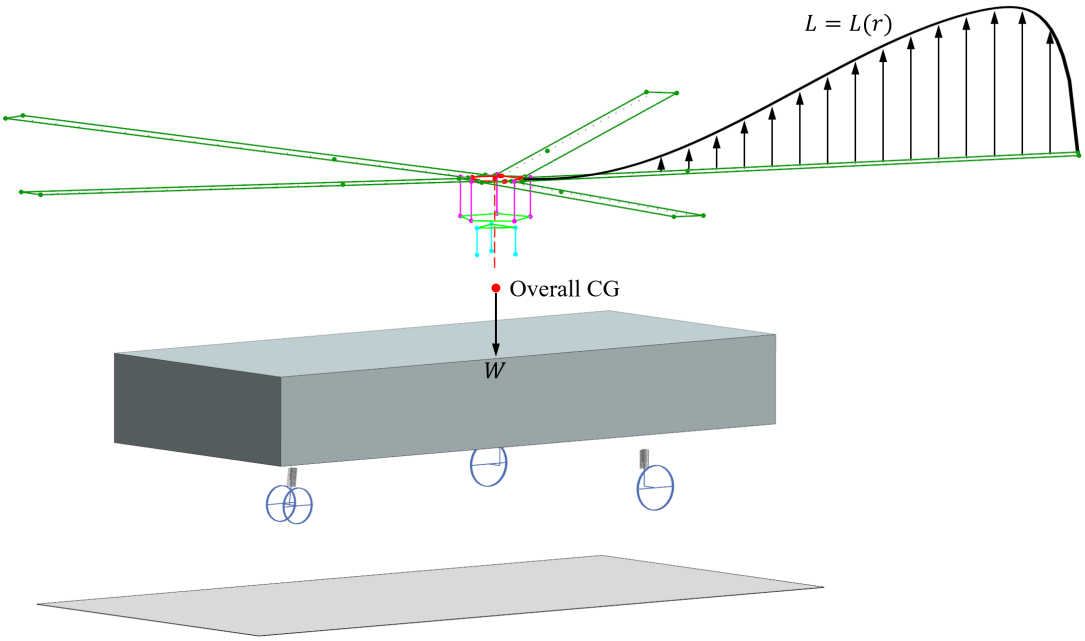


Figure 3.4: Isometric view of 3-point landing analysis with Model C

This distribution of lift force is illustrated in Figure 2.18. The implementation of this distributed lift force and the introduction of additional degrees of freedom by incorporating the rotor model represent the key distinction between the analysis performed using Model C and that of Model B. Additionally, it should be noted that the lift force in Model C does not remain constant subsequent to contact with the ground, as the dynamic flapping motion of the blades affects the aerodynamic force acting on them, as previously discussed in Chapter 2.3.1.

3.2 Tail-Down Landing

In the tail-down landing scenario, the helicopter is characterized by a pitch-up attitude prior to touchdown, with the main wheels making simultaneous contact with the ground while the nose wheel does not. The pitch angle for this maneuver is determined to be 15 degrees as an average value, as stipulated by the certification standard stating that the helicopter is assumed to be in the maximum nose-up attitude allowing ground clearance by each part of the helicopter. This angle is commonly referred to as the *tail-strike* angle, as the tail is the first part of the helicopter anticipated to come into contact with the ground in an excessive nose-up attitude.

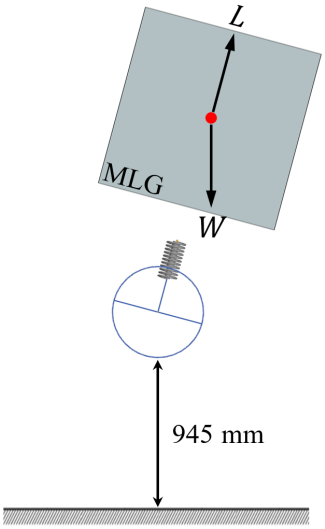


Figure 3.5: Side view of tail-down landing analysis with Model A

In the analysis utilizing Model A, the primary focus is on the MLG during a tail-down landing scenario, as the NLG is not considered to make contact with the ground.

While in actuality, the NLG may also come into contact with the ground following the initial contact of the MLG, this static analysis method assumes that critical loads occur at the initial point of contact and the effect of the NLG is disregarded. Additionally, the pitch attitude of the MLG model is adjusted to align with the tail-strike angle, as established by industry standards.

In this scenario, as the helicopter cannot maintain a static position without the support of the NLG, a dynamic analysis method known as *inertia relief* is utilized to determine the MOG values of the MLG units. This method involves the consideration of the planar (2D) motion of the helicopter, including linear acceleration in the vertical direction and angular acceleration in the pitch direction. This concept is illustrated through a free body diagram in Figure 3.6.

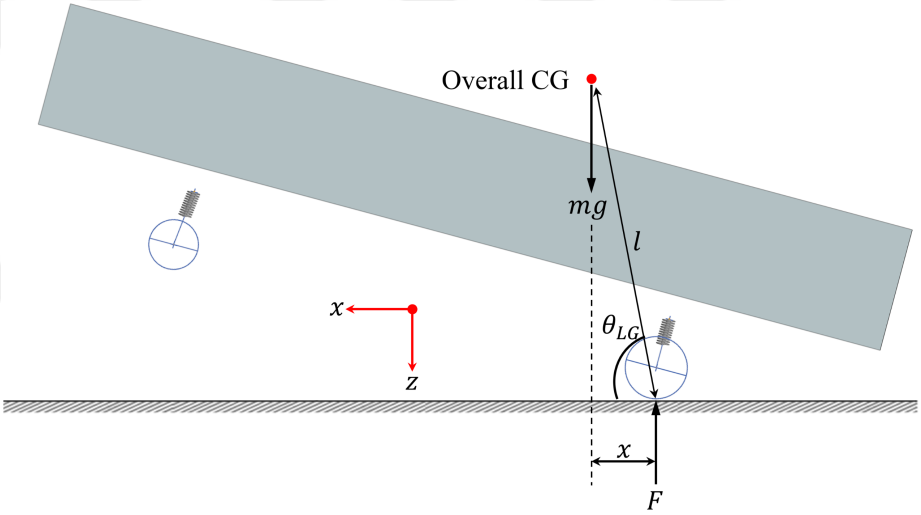


Figure 3.6: Free body diagram for tail-down landing inertia relief method

Where, the combined forces of the left and right MLG are represented by F. Newton's Second Law in the z-direction can be written as follows:

$$ma_z = mg - F \tag{3.5}$$

Similarly, in the pitch direction, the following equation applies:

$$-Fx = I_{yy}\alpha_y \tag{3.6}$$

Since the ground contact point serves as a pivot in this problem, a_z and α_y are related

to each other through the following equation:

$$a_z = -\alpha_y l \cos\theta_{LG} \tag{3.7}$$

By recognizing that $l\cos\theta_{LG} = x$, and substituting Equation 3.6 into Equation 3.7, a_z is obtained as:

$$a_z = \frac{1}{I_{yy}} F x^2 \tag{3.8}$$

Then, Equation 3.5 becomes:

$$m\frac{1}{I_{yy}} F x^2 = mg - F \tag{3.9}$$

Solving Equation 3.9 for F, the combined ground reactions of the MLGL and MLGR units are finally determined as follows:

$$F = mg\frac{I_{yy}}{I_{yy} + mx^2} \tag{3.10}$$

To calculate the individual MLG MOGs, the combined ground reaction force, F, is divided by two. Furthermore, as the unit of F is in Newtons, it is also divided by g to express the MOGs in terms of mass as shown below:

$$\text{MOG} = \frac{m}{2}\frac{I_{yy}}{I_{yy} + mx^2} \tag{3.11}$$

By implementing the procedure outlined above, the MOG values for Model A in the tail-down landing analysis are calculated and presented in Table 3.4.

Table 3.4: MOG values for Model A in tail-down landing

Landing gear	**MOG [kg]**
NLG	0
MLGL	2809
MLGR	2809

As illustrated in Table 3.4, the calculated total MOG is less than the actual weight of the helicopter, as the aircraft experiences a downward acceleration. Upon determining the MOG values for Model A, the analysis proceeds in a similar manner to that of the 3-point landing scenario, with the maximum ground reactions being calculated. Subsequently, the accelerations of the overall system are computed using Equations 3.3 and 3.4, thereby completing the analysis.

In the analyses with models B and C, the tail-down landing scenario is approached in a similar manner to that of the 3-point landing analysis. The only distinction is the inclusion of an initial pitch-up attitude for the models, as illustrated in Figure 3.7.

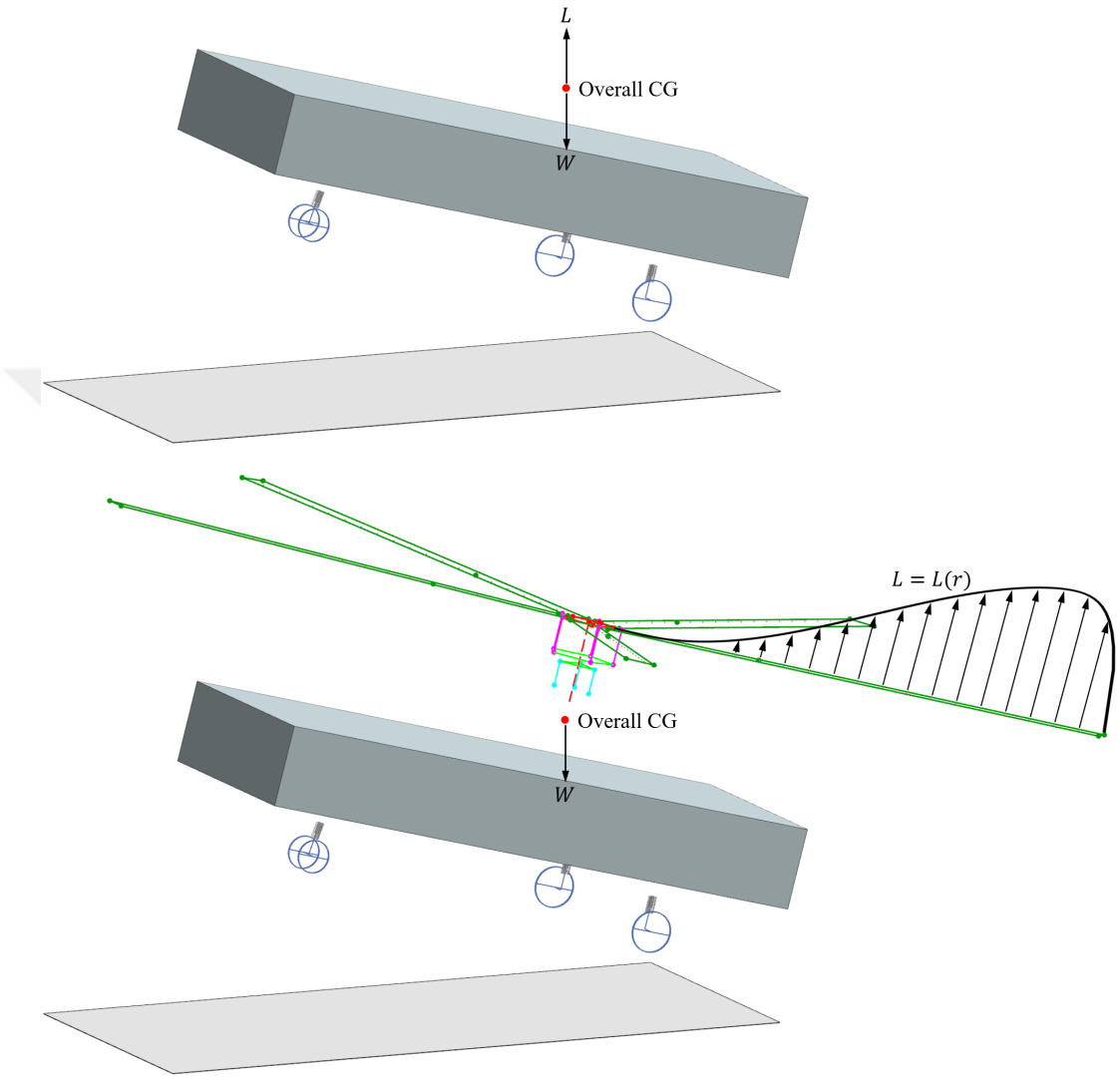


Figure 3.7: Isometric view of tail-down landing analyses with models B (top) and C (bottom)

3.3 Lateral Slope Landing

In the context of a lateral slope landing, the helicopter maintains a horizontal orientation upon approaching the ground. This scenario may arise in emergency situations,

where one of the main wheels of the helicopter makes contact with a laterally inclined surface, while the other wheels remain elevated.

The regulations outlined in article 29.483(a) of the CS stipulate that the vertical load during a lateral slope landing must be equivalent to that of a 2-point landing condition, which is similar to a tail-down landing scenario with the main wheels in contact with the ground while the nose remains clear of the ground. However, the utilization of Equation 3.11 as a bookcase method in this scenario is deemed to be an unnecessary assumption within the scope of this study. Therefore, a physics-based analysis will be conducted to determine the MOG values during a lateral slope landing. The 2-dimensional inertia relief method outlined in the previous chapter can be extended to include the roll axis, as depicted in the free body diagram in Figure 3.8.

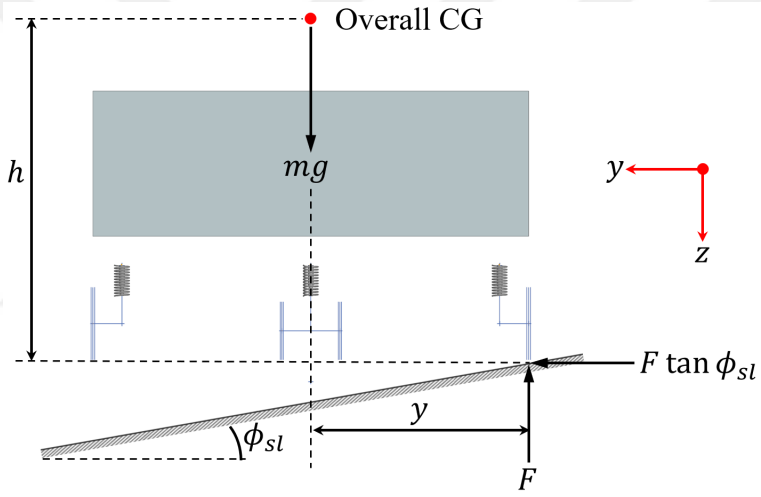


Figure 3.8: Free body diagram for lateral slope landing inertia relief method

The determination of the MOG for a lateral slope landing is achieved by extending the 2-dimensional inertia relief method previously described, to include the roll axis. This is accomplished by utilizing the decoupling of the pitching and rolling axes, and superposing their respective inertia relief factors, as outlined in Equation 3.12. The steps for this calculation are identical to those described in the previous chapter.

$$\text{MOG} = m\frac{I_{yy}}{I_{yy} + mx^2}\,\frac{I_{xx}}{I_{xx} + my\,(y - h\tan\phi_{sl})} \tag{3.12}$$

Where the variable ϕ_{sl} represents the inclination angle of the ground surface, which is chosen to be 10 degrees in this study. An examination of Equations 3.11 and 3.12

reveals that, in order for the assumption outlined in the CS that the vertical force on a one-wheel (or lateral slope) landing must be equivalent to that of a 2-point landing to be upheld, the fraction term on the right-hand side of Equation 3.12 must be equal to 0.5. In the case of the helicopter being analyzed, this assumption is nearly realized, with the fraction term equalling 0.486. However, it should be noted that the fraction term is dependent on multiple parameters and making such an assumption may lead to over or underprediction of loads during one-wheel (or lateral slope) landings.

The results displayed in Figure 3.9 further reinforce the aforementioned conclusion that, while the assumption in the CS is almost realized for the specific helicopter considered in this model, there is still a degree of variability and deviation present that must be taken into account when predicting loads during one-wheel (or lateral slope) landings. For reference, the contour plot in the figure illustrates the ratio of calculated MOG in one-wheel landing to the MOG in 2-point landing, with the slope angle set to zero and I_{xx} and y terms varied only, serving as a visual representation of the validity of the assumption in CS.

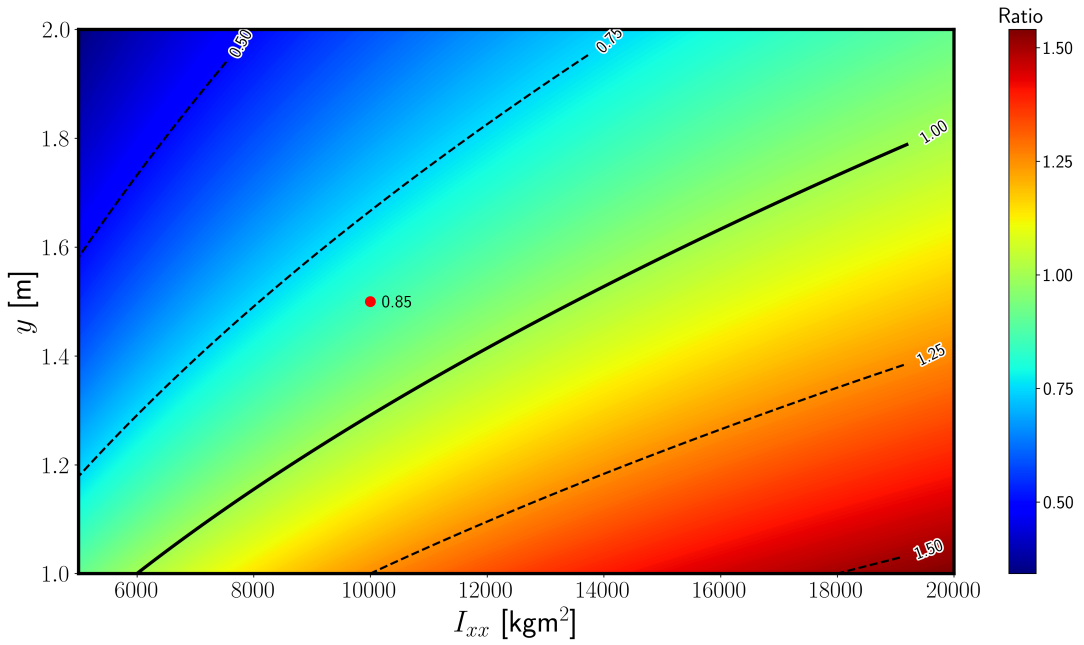


Figure 3.9: Contour plot of the ratio of calculated MOG in one-wheel landing to the MOG in 2-point landing for a range of I_{xx} and y values, with the slope angle set to zero. The helicopter used in this study is represented by the red dot

The MOG values that have been computed for Model A are presented in Table 3.5 as a result of the analysis conducted.

Table 3.5: MOG values for Model A in lateral slope landing

Landing gear	**MOG [kg]**
NLG	0
MLGL	2349
MLGR	0

It should be noted that, within the framework of this 2D method of analysis, it is assumed that the off-diagonal elements of the inertia matrix are negligible. In reality, as a helicopter is not a symmetric object, the product of inertia terms also contribute to the overall moment of inertia. However, although an exact 3D analysis that includes the product of inertia terms of the helicopter can also be performed to determine the MOG, as the product of inertia is relatively small compared to the moment of inertia terms, the use of the 2D inertia relief method as an approximation is deemed to be a valid assumption.

Upon determining the MOG values for Model A for the current landing condition, the maximum ground reactions are calculated in accordance with established methodology. Subsequently, the accelerations of the overall system are determined through application of Equations 3.3 and 3.4, thereby completing the analysis for Model A.

The analysis of lateral slope landing conditions for Models B and C were conducted by applying a slope angle to the ground, as depicted in Figures 3.10 and 3.11 respectively.

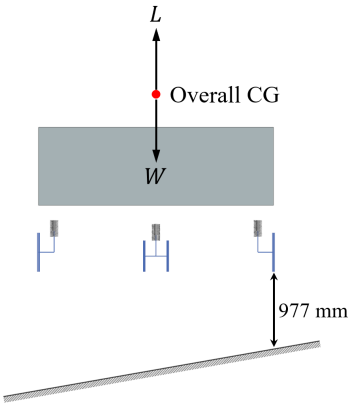


Figure 3.10: Front view of lateral slope landing analysis with Model B

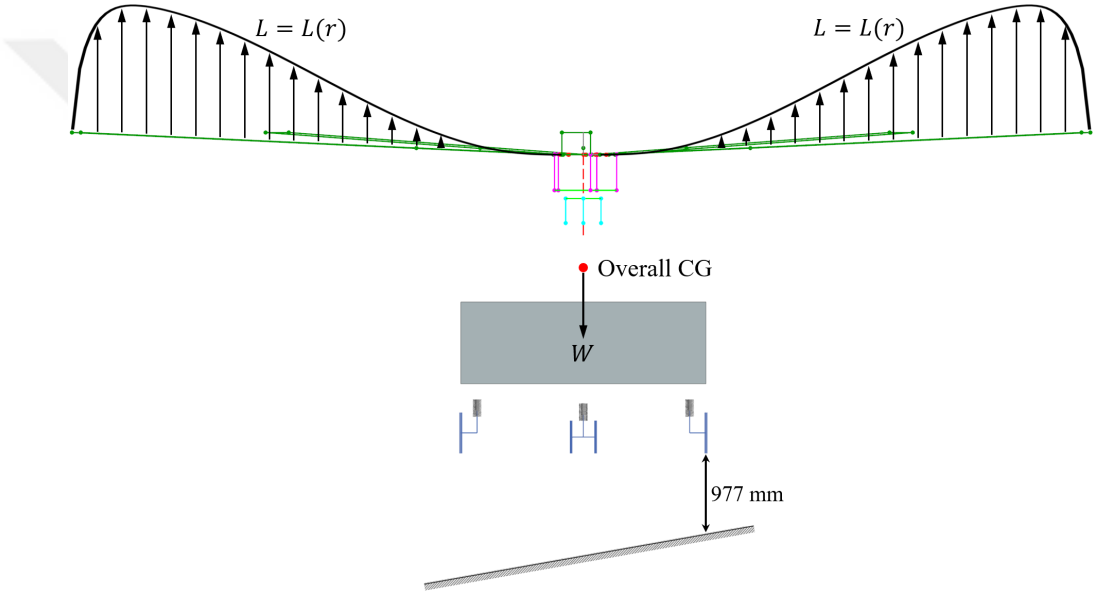


Figure 3.11: Front view of lateral slope landing analysis with Model C

3.4 Running Landing

Helicopters are capable of landing with forward speed, also known as a *run-on* or *running* landing. This type of landing can be useful in situations where the helicopter does not have enough power to hover in high-density altitude environments or when there are strong crosswinds that make it difficult to hover in one spot. Additionally, running landings can be utilized in emergency situations, such as when the helicopter loses power and the pilot needs to perform an autorotation landing.

During a running landing, the helicopter approaches the landing site with forward speed. As the helicopter touches down, the wheels of the helicopter, which were not rotating prior to landing, begin to spin due to the friction between the road and the tires. The force of friction that is generated by the relative motion between the ground and the tire surface continues to act on the wheels until the wheels are angularly accelerated to match the helicopter's rolling speed. After the peak drag load, known as the spin-up load, is reached, the rotational speed of the wheel is considered to have reached the helicopter's rolling speed and the drag load at the ground quickly diminishes to zero [33].

In reality, elasticity of the landing gear and the structure that attaches it to the fuselage can cause the gear to deflect rearward under the spin-up load, storing potential energy in the form of structural strain. Once spin-up is reached, the potential energy that was stored in the landing gear is released, causing the gear to *spring back* [5, 34]. Subsequently, the landing gear oscillates back and forth until friction with the ground and structural damping dissipate the stored potential energy [35]. Time histories of vertical and drag forces, as well as spin-up and spring-back loads during a running landing can be seen in Figure 3.12.

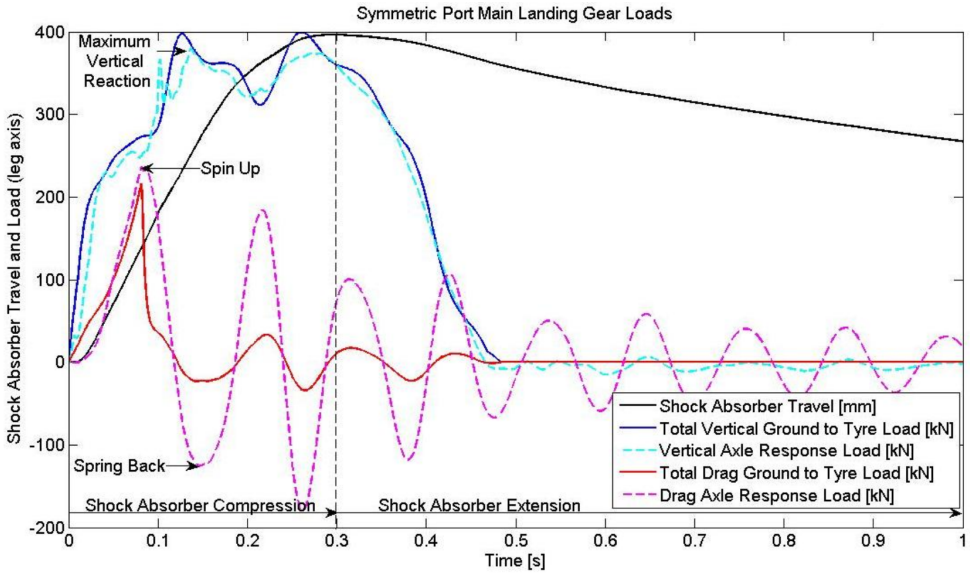


Figure 3.12: Time histories of vertical and drag forces, as well as spin-up and spring-back loads during a running landing [35].

As depicted in Figure 3.12, the drag force (represented by the pink dashed line) acts in both aft and forward directions. The spring-back load, which is similar in magnitude to the spin-up load, acts in the opposite direction. However, in the current study, which only considers rigid bodies, the spring-back effect cannot be modeled as it is dependent on the elasticity of the landing gear structure. Therefore, the analysis of running landing within this work is limited to the spin-up load.

Currently, Model A is a two degree of freedom system that is constrained to the vertical motion, allowing for the calculation of vertical ground reaction and acceleration. Nonetheless, by incorporating appropriate assumptions, Model A can be extended to analyze spin-up behavior. The drag force during spin-up, represented by F_D, is a result of friction and can be mathematically expressed as:

$$F_D(t) = \mu F_V(t) \tag{3.13}$$

Where μ is the coefficient of friction between the ground and the tire, and F_V is the vertical ground reaction force. Behavior of friction coefficient depends on slip ratio (SR), which is a measure of the wheel slip [19] and is given by:

$$\text{SR} = 1 - \frac{\omega_w r_w}{V_F} \tag{3.14}$$

Where r_w is the radius of the wheel, ω_w is the angular velocity of the wheel and V_F is the forward speed of the helicopter. Typical variation of the friction coefficient as a function of the slip ratio is shown in Figure 3.13.

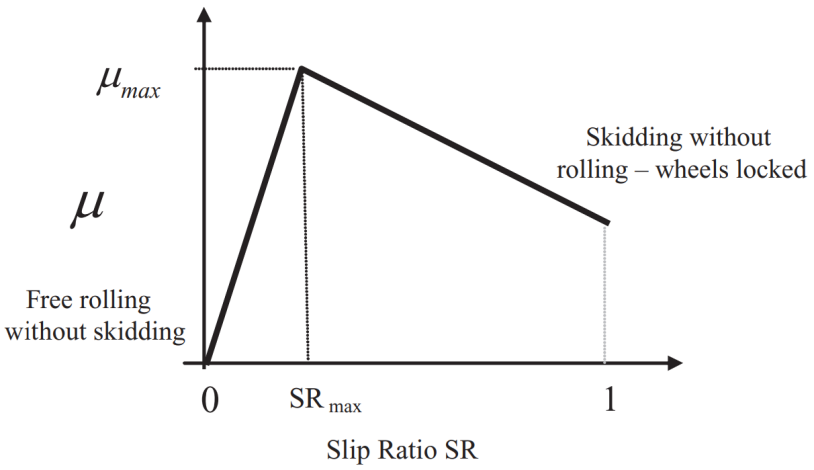


Figure 3.13: Variation of friction coefficient with respect to slip ratio [19]

Maximum friction coefficient, $\mu_{\max}$, is typically around 0.8 for a dry concrete runway [19]. Although the relationship between the coefficient of friction and the slip ratio is nonlinear and the friction coefficient can vary rapidly during spin-up, it can be assumed to be constant for the purposes of this analysis. A value of 0.55, which is in agreement with the values reported in previous studies (e.g., [21, 22, 33]), can be chosen as the average value for this constant.

Furthermore, it can be assumed that the vertical ground reaction follows a quarter sine wave profile and reaches its maximum value at a certain time t_V. If the maximum vertical ground reaction is $F_{V_{\max}}$, the vertical ground reaction can be obtained as shown in Equation 3.15 with respect to time.

$$F_V(t) = F_{V_{\max}} \sin\left(\frac{\pi}{2}\frac{t}{t_V}\right) \tag{3.15}$$

It is also assumed here that $F_{V_{\max}}$ is the same as in a purely vertical landing scenario without forward speed. The spin-up time, t_{SU}, is defined as the point at which the relative speed between the landing gear and the runway is zero. This is also the point at which the spin-up load is applied to the landing gear. By substituting Equation 3.15 into Equation 3.13 and setting $t = t_{SU}$, the spin-up load can be calculated as:

$$F_{D_{SU}} = \mu F_{V_{\max}} \sin\left(\frac{\pi}{2}\frac{t_{SU}}{t_V}\right) \tag{3.16}$$

Similarly, vertical ground reaction at the instant of spin-up can be obtained as:

$$F_{V_{SU}} = F_{V_{\max}} \sin\left(\frac{\pi}{2}\frac{t_{SU}}{t_V}\right) \tag{3.17}$$

The assumed trends for the ground reactions in vertical and drag directions are visualized in Figure 3.14.

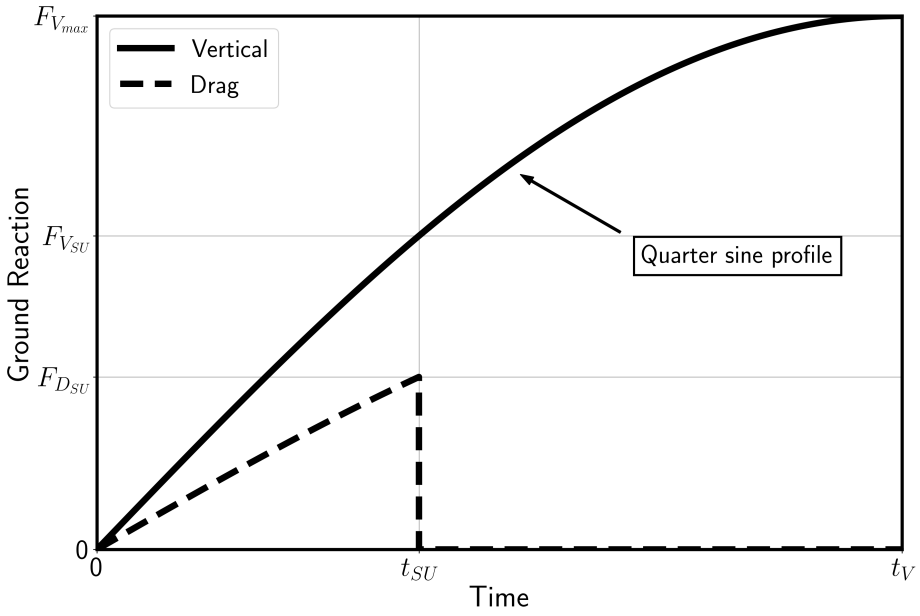


Figure 3.14: Assumed profiles for the development of ground reactions in vertical and drag directions for the spin-up analysis

As a result, the only unknowns at this point are the time of maximum vertical ground reaction, t_V, and the spin-up time, t_{SU}. To determine t_V, the outputs of the 3-point landing analysis performed with Model A can be utilized. By integrating the vertical speed, $V_V(t)$, with respect to time, the vertical deflection of the MOG at the instant of maximum ground reaction, d_V, can be obtained. This value, which is an output of the 3-point landing analysis and is known, can be used to calculate t_V as shown in the following equation:

$$d_V = \int_0^{t_V} V_V(t)dt \tag{3.18}$$

The vertical speed, $V_V(t)$, can be determined by combining the initial sink speed of the helicopter, V_S, with the integral of the vertical acceleration, $a_V(t)$, over time.

$$V_V(t) = V_S + \int_0^t a_V(t')dt' \tag{3.19}$$

Acceleration $a_V(t)$ can be determined by analyzing the free-body diagram of the MOG in the vertical axis, as illustrated Figure 3.15.

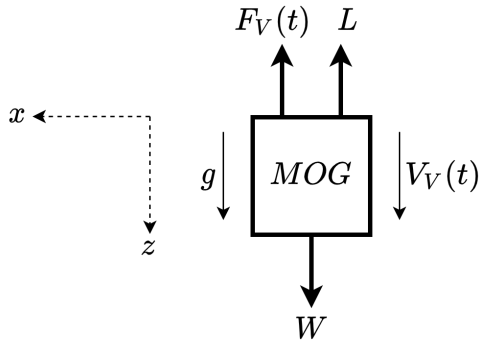


Figure 3.15: Free body diagram of the MOG in vertical axis during landing impact

The vertical acceleration of the MOG, which is subject to weight (W), lift (L), and ground reaction forces, can be calculated by using Newton's second law of motion as:

$$a_V(t) = \frac{1}{\text{MOG}} \left[W - L - F_{V_{\text{max}}} \sin\left(\frac{\pi}{2} \frac{t}{t_V} \right) \right] \tag{3.20}$$

Substituting Equations 3.19 and 3.20 into Equation 3.18:

$$d_V = \int_0^{t_V} \left\{ V_S + \int_0^t \frac{1}{\text{MOG}} \left[W - L - F_{V_{\text{max}}} \sin\left(\frac{\pi}{2} \frac{t'}{t_V} \right) \right] dt' \right\} dt \tag{3.21}$$

To continue, the *lift factor* (L_f) which is the ratio of lift force to weight force can be introduced:

$$L_f = \frac{L}{W} \tag{3.22}$$

To make further simplifications, *landing gear load factor* (n_{LG}) is also introduced as:

$$n_{LG} = \frac{F_{V_{\text{max}}}}{W} \tag{3.23}$$

By solving the integrals in Equation 3.21, the following expression that is quadratic in t_V is obtained:

$$\underbrace{g \left[\frac{1}{2}(1 - L_f) + n_{LG} \left(\frac{4}{\pi^2} - \frac{2}{\pi} \right) \right]}_{\text{a}} t_V^2 + \underbrace{V_S}_{\text{b}} \; t_V + \underbrace{d_V}_{\text{c}} = 0 \tag{3.24}$$

Finally, the solution of Equation 3.24 for t_V is obtained as shown below:

$$t_V = \frac{-V_S + \sqrt{V_S^2 - 4g \left[\frac{1}{2}(1 - L_f) + n_{LG} \left(\frac{4}{\pi^2} - \frac{2}{\pi} \right) \right] d_V}}{2g \left[\frac{1}{2}(1 - L_f) + n_{LG} \left(\frac{4}{\pi^2} - \frac{2}{\pi} \right) \right]} \tag{3.25}$$

With a similar analysis, the rotational dynamics of the wheel can be used to calculate t_{SU} by integrating the angular acceleration of the tire (α_w) with respect to time to determine the angular speed (ω_w) of the tire.

$$\omega_w(t) = \int_0^t \alpha_w(t')dt' \tag{3.26}$$

Angular acceleration $\alpha_w(t)$ can be found by considering the free body diagram of the wheel in rotational axis as shown:

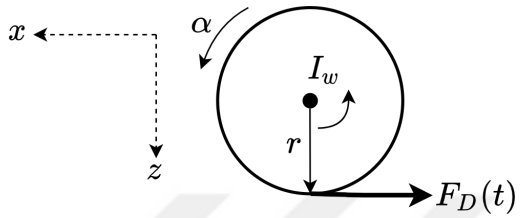


Figure 3.16: Free body diagram of the wheel in rotation axis during landing impact

By Euler's second law:

$$\alpha_w(t) = \frac{1}{I_w} r_w F_D(t) \tag{3.27}$$

Where I_w is the mass moment of inertia of the wheel in the axis of rotation. Thus, recalling Equations 3.13 and 3.15, Equation 3.26 can be written as:

$$\omega_w(t) = \int_0^t \frac{1}{I_w} r_w \mu F_{V_{\max}} \sin\left(\frac{\pi}{2}\frac{t'}{t_V}\right) dt' \tag{3.28}$$

It is known that at the instant of spin-up, wheel's rotational speed matches the helicopter's forward speed V_F. Thus, by setting $t = t_{SU}$ and rewriting wheel's angular speed in terms of its radius and V_F:

$$\frac{V_F}{r_w} = \int_0^{t_{SU}} \frac{1}{I_w} r_w \mu F_{V_{\max}} \sin\left(\frac{\pi}{2}\frac{t}{t_V}\right) dt \tag{3.29}$$

Finally, the solution of Equation 3.29 for t_{SU} is obtained as follows:

$$t_{SU} = \frac{2t_V}{\pi} \cos^{-1}\left(1 - \frac{\pi I_w V_F}{2\mu t_V r_w^2 F_{V_{\max}}}\right) \tag{3.30}$$

Once t_{SU} and t_V have been determined, the ground reactions in both the vertical and drag directions for the running landing condition can be calculated using Equations 3.17 and 3.16, respectively.

By utilizing the calculated ground reactions for each landing gear, the system's overall accelerations can be computed using Equations 3.3 and 3.4, thus completing the analysis with Model A.

The analysis for Models B and C are conducted in a similar manner as that of a 3-point landing, with the only distinction being the incorporation of an initial angular velocity to the wheels that corresponds to the specified forward speed of the helicopter. This approach is deemed suitable as the scenario of the helicopter not moving forward and the wheels rotating, as well as the scenario of the helicopter moving forward while the wheels are stationary with respect to the helicopter, exhibit analogous dynamics. Furthermore, this methodology is also in line with the method practiced in landing gear drop tests, where an initial angular speed to the wheels in the opposite direction of motion is given prior to the drop test to test spin-up behavior.

CHAPTER 4

RESULTS

The results of all the landing maneuvers described in Chapter 3, performed with each of the models, are presented in this section. Model A, being a static analysis model, only exhibits a single value for each parameter. Conversely, Models B and C provide time-based representations of the parameters throughout the simulations. Despite the availability of time histories, the design of the helicopter is based on the critical values of loads. As such, this study places emphasis on comparing the results from Model A with the extreme values from Models B and C.

4.1 3-Point Landing

The primary focus of this study in terms of airframe loads are the accelerations at the CG and nose and tail stations. The extreme values of the linear accelerations obtained in 3-point landing analysis are presented in Table 4.1.

Table 4.1: Linear accelerations obtained in 3-point landing. Unit is [m/s^2]

Model	**c.g.**			**Nose Station**			**Tail Station**		
	$\dot{u}$	$\dot{v}$	$\dot{w}$	$\dot{u}$	$\dot{v}$	$\dot{w}$	$\dot{u}$	$\dot{v}$	$\dot{w}$
A	0.0	0.0	-18.9	0.5	0.0	-20.9	-0.3	0.0	-16.3
B max.	0.3	0.0	5.8	0.8	0.0	10.7	0.9	0.0	4.5
B min.	-0.1	0.0	-18.8	-1.2	0.0	-21.9	-0.4	0.0	-17.6
C max.	0.2	0.3	3.9	0.7	0.7	4.7	0.5	1.0	4.3
C min.	-0.3	-0.9	-18.9	-1.0	-2.8	-21.7	-0.4	-0.9	-18.6

In the 3-point landing scenario, as a vertical landing onto a level ground surface is performed, the dominant acceleration term is the vertical acceleration, $\dot{w}$, at each monitoring station. Analysis reveals that the critical $\dot{w}$ term at the CG is consistent across all three models with an error of nearly 0%. However, a comparison of the $\dot{w}$ term at the nose and tail stations between the models reveals differences of approximately 4.8% and 14.1%, respectively. As linear accelerations at the nose and tail stations are influenced by angular velocities and accelerations, according to Equation 2.1, results for these parameters are also presented in Table 4.2.

Table 4.2: Angular accelerations and velocities obtained in 3-point landing

Model	**Acceleration [°/s²]**			**Velocity [°/s]**		
	$\dot{p}$	$\dot{q}$	$\dot{r}$	p	q	r
A	0.0	29.3	0.0	0.0	0.0	0.0
B max.	0.0	47.5	0.0	0.0	4.0	0.0
B min.	0.0	-67.8	0.0	0.0	-1.1	0.0
C max.	6.3	44.0	3.7	0.8	3.5	0.1
C min.	-14.0	-54.3	-1.2	0.0	-1.1	0.0

The results of the angular motion analysis of the helicopter indicate that the dominant term is the pitching acceleration, $\dot{q}$. Model A and B exhibit angular motion exclusively in the pitching axis, while Model C displays a combination of smaller magnitudes of motion in the rolling and yawing axes in addition to the dominant pitching motion.

To continue, the underlying factors that drive the acceleration terms studied in this work are the ground reactions, which represent the dominant forces acting on the helicopter and are investigated in Table 4.3.

Table 4.3: Maximum ground reactions obtained in 3-point landing, in Newtons

Model	NLG	MLGL	MLGR
A	40367	46235	46235
B	42513	44886	44886
C	42270	44383	44501

As can be seen, the error rates in the NLG, MLGL, and MLGR ground reactions have been recorded as 5.3%, 4.0%, and 3.7%, respectively. Despite the relatively small error in ground reactions, a deviation of 14.1% was observed in the vertical acceleration at the tail section. In order to delve deeper into this matter, the time histories of the ground reactions in the analysis with Model C are presented in Figure 4.1.

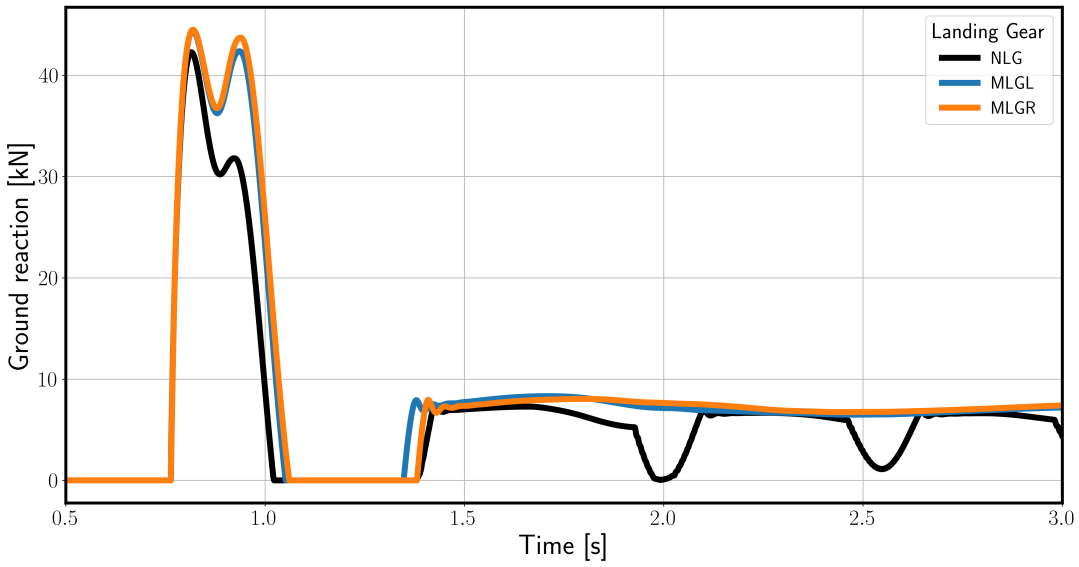


Figure 4.1: Time variation of ground reaction forces in Model C during 3-point landing

The results of the ground reaction analysis exhibit the rapid build-up and subsequent rapid decrease in the magnitude of ground reactions on each wheel upon initial contact. This occurrence signifies the rebounding of the helicopter from the ground, which was observed in the examination of limit landing scenarios with high descent rates in this study. Following the rebounding, the landing gears re-engage the ground and exhibit oscillatory motion until a steady state is achieved, dissipating energy

through the dampers. It is noteworthy that although the landing scenario analyzed in this study is symmetrical, an asymmetry between the left and right MLG reactions is observed in the analysis with Model C, which will be further examined later in the study.

The post-impact ground reactions, which are deemed critical, are analyzed and compared between the models in Figure 4.2.

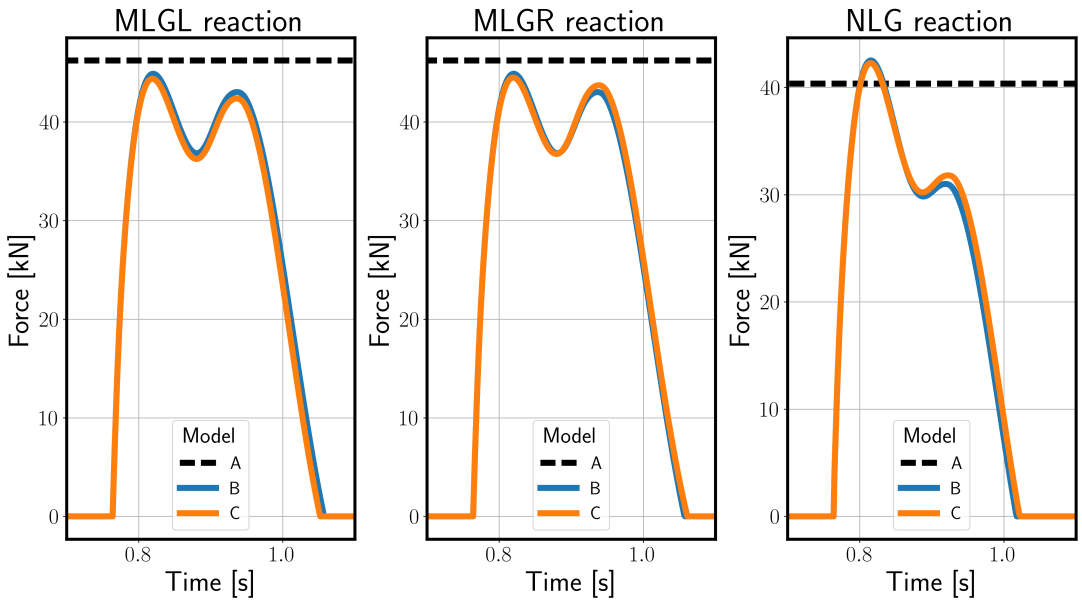


Figure 4.2: Comparison of ground reactions between the models in 3-point landing

The results indicate that Model A exhibited over-prediction of the MLG reactions, while under-predicting the NLG reactions when compared to Models B and C. Conversely, Model B and C displayed consistent agreement with one another in terms of ground reactions.

The temporal evolution of the vertical acceleration at the center of gravity and the pitching acceleration of the helicopter are analyzed in Figure 4.3.

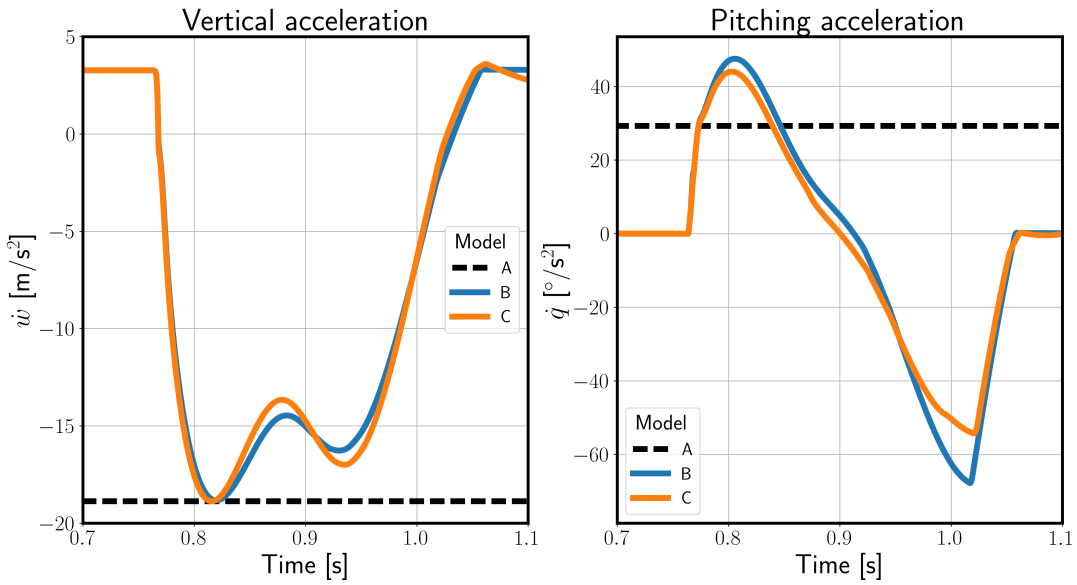


Figure 4.3: Time variation of vertical acceleration of the CG and pitching acceleration of the helicopter during 3-point landing

The time variation of the vertical accelerations at the nose and tail monitoring stations, which, along with the vertical acceleration of the CG, provide insight into the airframe loads, is depicted in Figure 4.4.

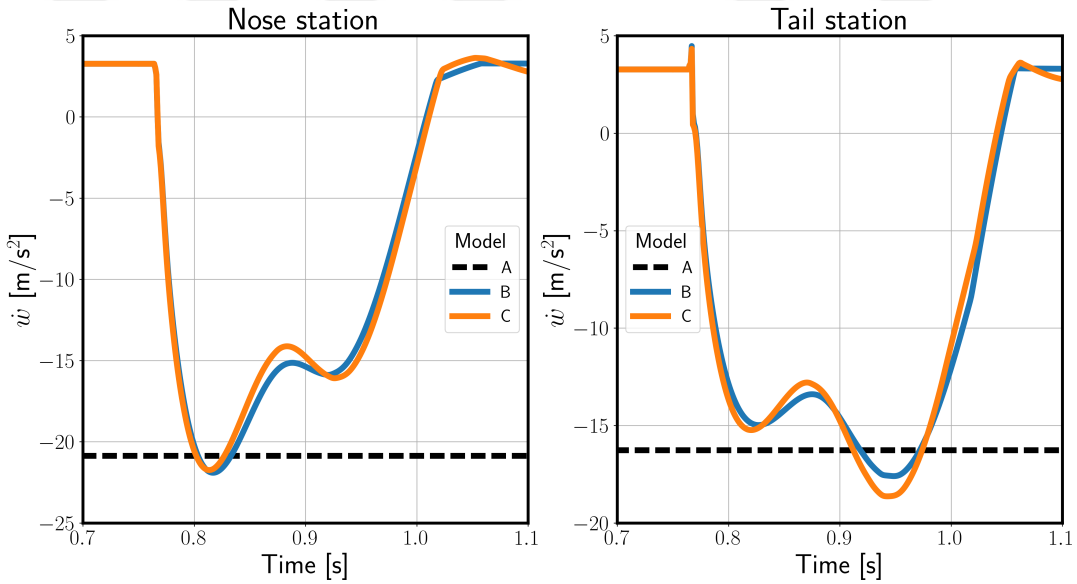


Figure 4.4: Time variation of vertical acceleration of the monitoring stations on the nose and tail sections during 3-point landing

It is observed that the static analysis model accurately captures the first and critical

peak of the vertical acceleration. On the other hand, for the pitching acceleration, while the static analysis model captures the first peak with relative accuracy, there is significant deviation among the models at the second peak. The limitation of the static analysis model, being non-time-dependent, lies in its inability to capture the second peak as this peak is not critical in terms of ground reactions. This, in turn, increases the error rate at the nose and tail stations, which are more sensitive to the $\dot{q}$ term according to Equation 2.2 due to their distance from the center of gravity.

A comprehensive examination of Figures 4.3 and 4.4 provides evidence that the deviation at the tail station is attributed to the second, negative peak of the pitching acceleration, acting as an upward vertical acceleration for the tail. This critical aspect is not captured by Model A.

A detailed examination of the MLG reactions of Model C, aimed at evaluating its asymmetry about the rolling axis, is presented in Figure 4.5.

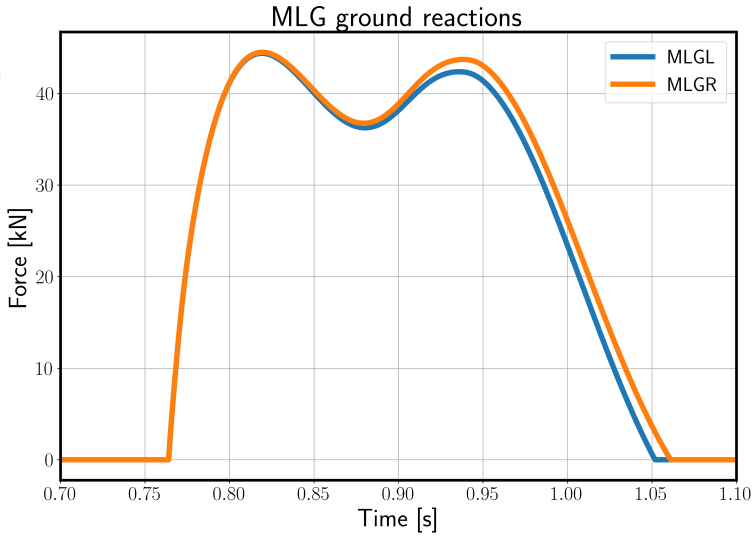


Figure 4.5: Time variation of left and right MLG ground reactions of Model C during 3-point landing

Additionally, Figure 4.6 presents the representation of the angular motion of the helicopter with respect to the rolling and pitching axes.

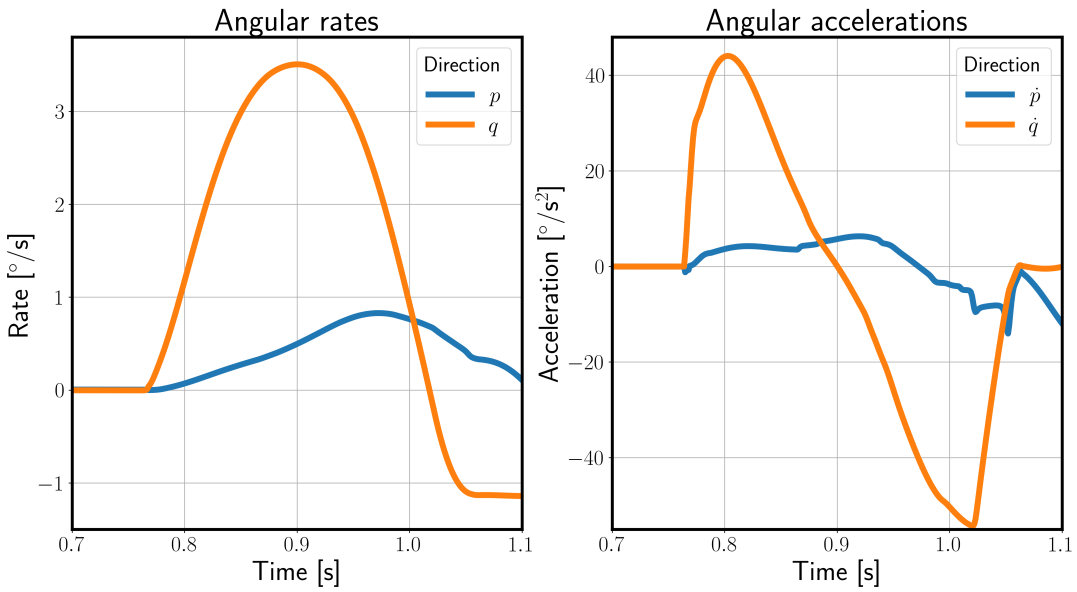


Figure 4.6: Velocities and accelerations around pitching and rolling axes in Model C during 3-point landing

The rolling motion of the helicopter as depicted in Model C, which is absent in Model B, is attributed to the gyroscopic effect of the rotor. Upon touch down, unbalanced moments caused by ground reactions initiate a pitching movement upwards, followed by a rolling movement towards the right. This is due to the rotor's gyroscopic moment acting on the airframe, which results in an increased load on the right MLG.

Examination of Figure 4.4 demonstrates that the acceleration in Model C undergoes greater oscillation when compared to Model B. This discrepancy is attributed to the varying lift force acting on the airframe in Model C, whereas in Model B the lift force remains constant. This variation in lift force is a result of the additional degree of freedom in blade flapping present in Model C, which leads to flapping motion of the blades upon touch down and ultimately results in a reduction of the force transferred to the rotor hub and airframe. The flapping response of the blades following touch down can be seen in Figure 4.7.

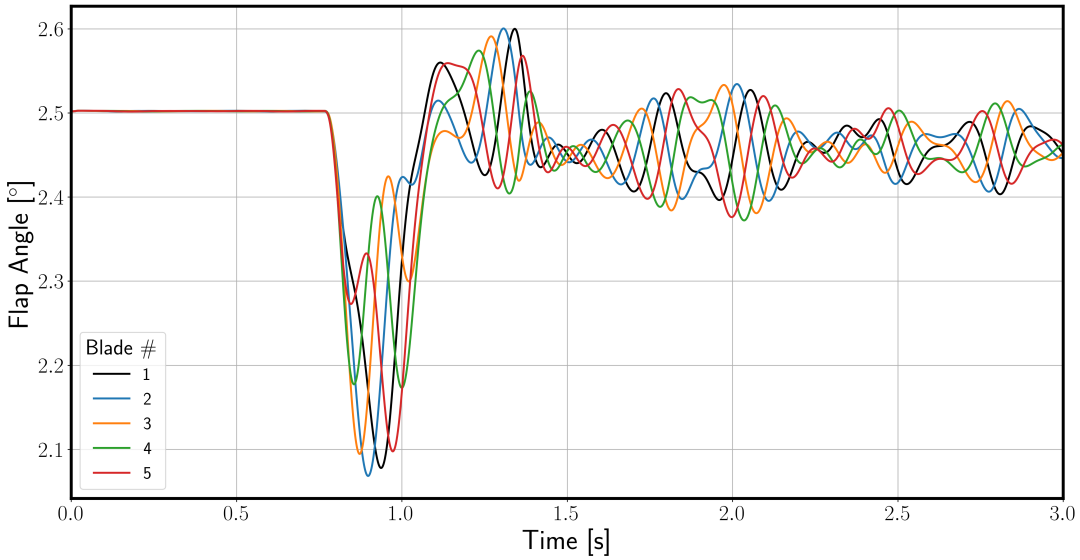


Figure 4.7: Flap response of the rotor blades in Model C during 3-point landing

Before touch down, the blades in Model C exhibit azimuthally symmetrical motion, as discussed in Chapter 2.3.1. However, upon touch down, each blade responds differently based on its azimuthal position at the moment of touch down, leading to a similar yet out-of-phase motion. The flapping motion of a single blade and the total lift force transferred to the airframe by the rotor can be seen in Figure 4.8.

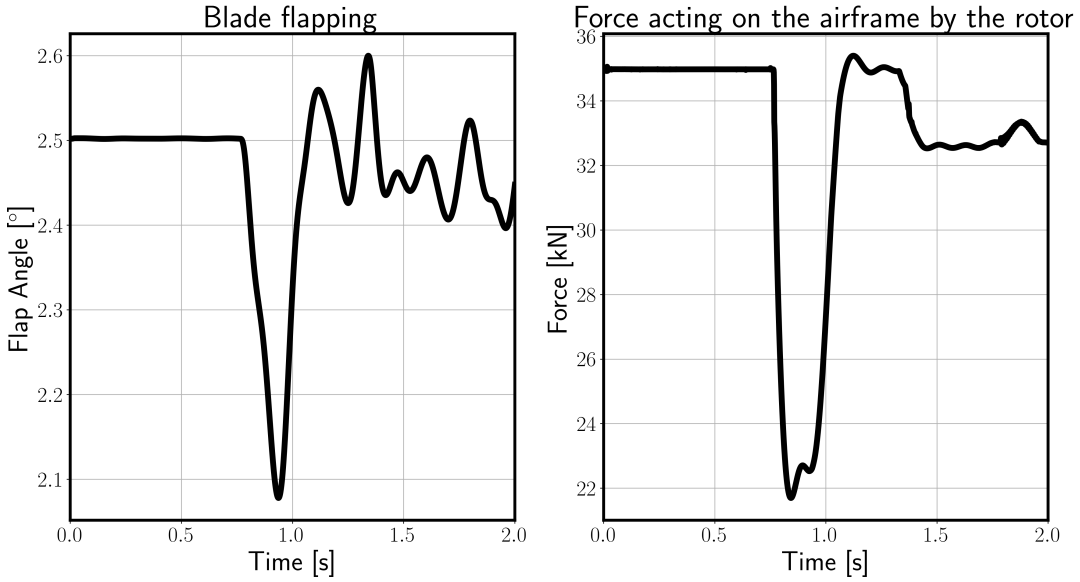


Figure 4.8: Flap response of an individual blade and rotor force acting on the airframe in Model C during 3-point landing

The examination of Figure 4.8 reveals that the lift force acting on the airframe during touch down rapidly decreases by approximately 35% below its nominal value, before rapidly returning to its nominal value. This fluctuation in the lift force leads to greater oscillations in the acceleration terms and results in higher critical loads, challenging the conventional assumption of constant lift throughout the landing process.

Aerodynamic forces acting on the blades also fluctuate during touch down. As the blades begin to flap down, they are subjected to increased air flow from their pressure sides, resulting in higher angle of attack and ultimately, lift. The rate of flapping and its impact on aerodynamic lift is depicted in Figure 4.9.

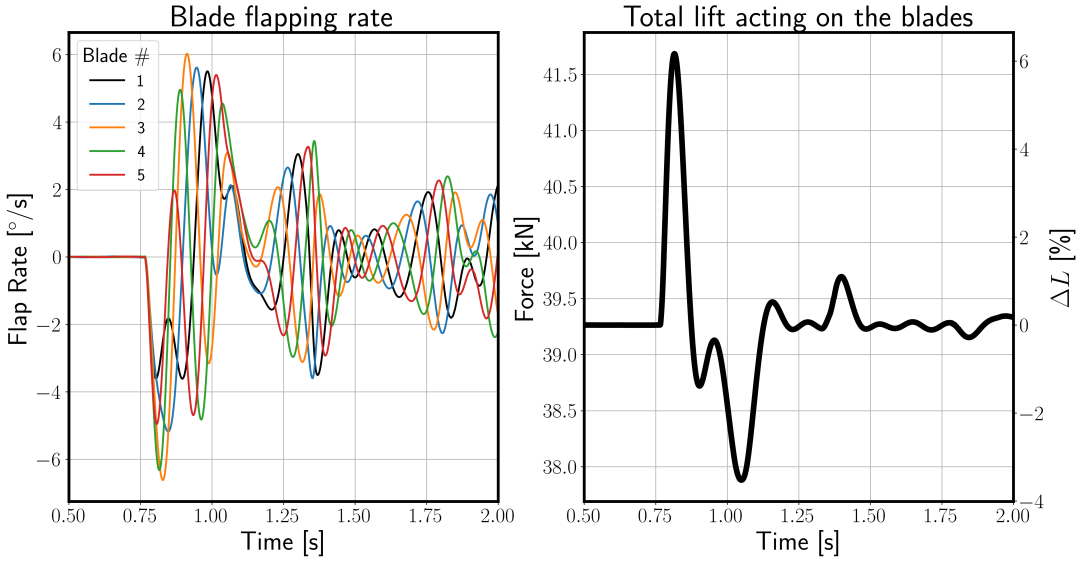


Figure 4.9: Flap rate of the blades and total aerodynamic lift acting on the blades in Model C during 3-point landing

It can be observed that the total aerodynamic lift acting on the blades experiences a fluctuation of approximately 10%. Furthermore, the flapping motion of the blades affects the lead-lag dynamics through the coupling of the Coriolis forces. The variation in the force acting on the blades by the lead-lag dampers is depicted in Figure 4.10. It is important to note that the forces generated by the lead-lag dampers on the rotor hub and blade are considered internal forces for the rotor in relation to the airframe. However, the interaction between the lead-lag and flapping motions can indirectly affect the overall rotor response on the airframe.

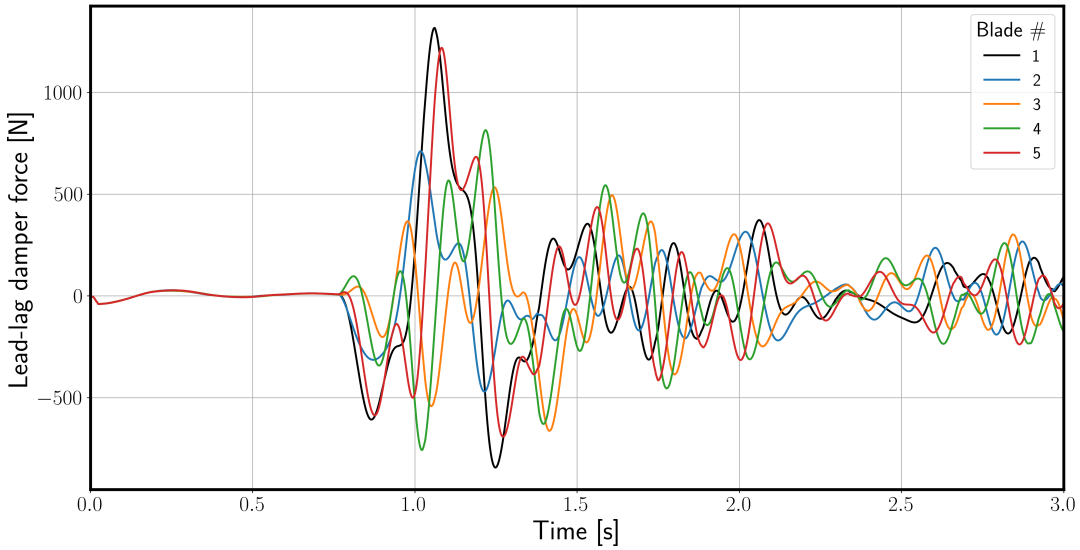


Figure 4.10: Lead-lag damper force acting on the blades in Model C during 3-point landing

In the case of Models B and C, multibody dynamics analysis is conducted and each component, including the wheels and shock absorbers, has its own acceleration. Thus, the ground reaction is not directly transmitted to the airframe. Instead, due to the acceleration experienced by the landing gear components, a force that is lower than the ground reaction acts on the airframe. Figure 4.11 shows the comparison between the ground reaction and the force acting on the airframe in the same landing gear.

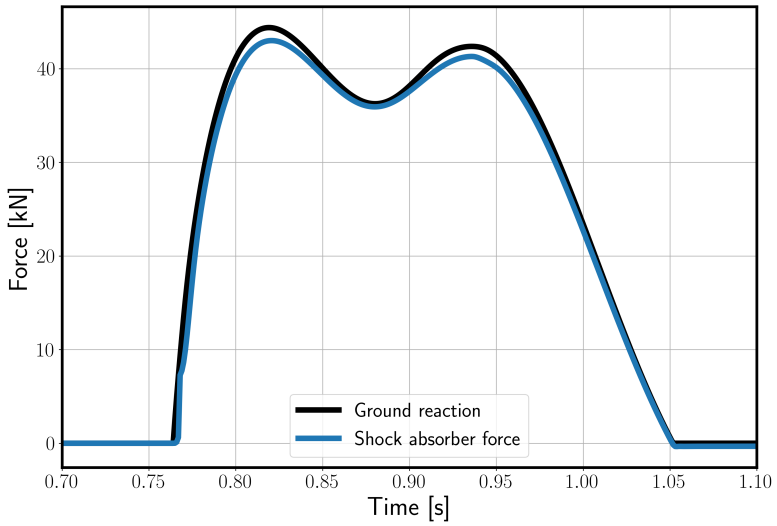


Figure 4.11: Comparison of ground reaction and shock absorber forces on left MLG unit in Model C during 3-point landing

As depicted in Figure 4.11, the force acting on the airframe via the attachment points of the landing gear is %3.1 less than the ground reaction force. Although the difference of %3.1 may appear to be small, it can be of significant value for the design engineer in the weight and structural optimization phase of the helicopter design process, facilitating the construction of a lighter structure.

4.2 Tail-Down Landing

In this subchapter, the outcomes of the tail-down landing analysis are evaluated through a comparable method as used in the 3-point landing analysis investigations. The linear and angular accelerations resulting from the tail-down landing analyses can be found in Tables 4.4 and 4.5, respectively.

Table 4.4: Linear accelerations obtained in tail-down landing. Unit is [m/s^2]

Model	**c.g.**			**Nose Station**			**Tail Station**		
	$\dot{u}$	$\dot{v}$	$\dot{w}$	$\dot{u}$	$\dot{v}$	$\dot{w}$	$\dot{u}$	$\dot{v}$	$\dot{w}$
A	5.9	0.0	-18.7	3.5	0.0	-9.5	7.1	0.0	-30.8
B max.	3.0	0.0	4.2	3.6	0.0	3.2	4.8	0.0	13.8
B min.	-2.5	0.0	-18.7	-2.9	0.0	-16.0	-2.5	0.0	-32.5
C max.	3.2	0.5	3.8	1.6	5.6	3.1	5.0	1.8	7.6
C min.	-2.5	-1.4	-19.3	-2.5	-3.2	-10.4	-2.6	-4.8	-31.1

Table 4.5: Angular accelerations and velocities obtained in tail-down landing

Model	**Acceleration [°/s^2]**			**Velocity [°/s]**		
	$\dot{p}$	$\dot{q}$	$\dot{r}$	p	q	r
A	0.0	-135.6	0.0	0.0	0.0	0.0
B max.	0.0	189.5	0.0	0.0	17.3	0.0
B min.	0.0	-156.1	0.0	0.0	-30.0	0.0
C max.	95.5	73.0	36.7	24.4	7.6	20.5
C min.	-160.3	-132.4	-13.1	-23.3	-25.4	0.0

The examination of the angular accelerations highlights that the angular motion is limited to the pitching axis for Models A and B. Meanwhile, Model C demonstrates a considerable level of motion in the rolling axis in addition to the pitching axis.

The analysis of linear accelerations indicates that, in the tail-down landing scenario, the dominant linear acceleration term is once again the vertical acceleration $\dot{w}$. However, the acceleration terms in the longitudinal direction, although still lower than $1g$, are higher in comparison to the 3-point landing scenario, as the ground reaction forces have components in the longitudinal axis of the helicopter. This is due to the helicopter having a pitched-up attitude during the initial impact. The comparison of the results from the analyses indicate that the error in the critical vertical acceleration at the cg station is 3.2%, while the error at the nose station is 68.4%, and the error at the tail station is 5.5%. A graphical representation of Model B's dynamics is provided in Figure 4.12 to enhance comprehension of the system's behavior.

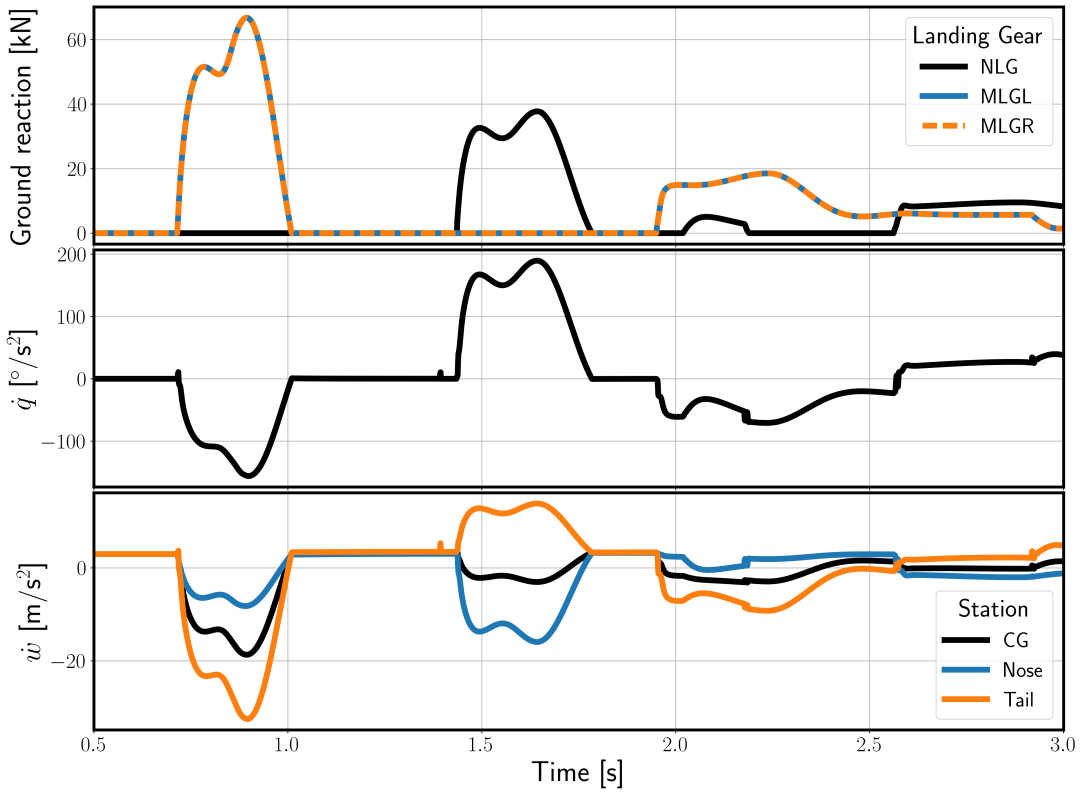


Figure 4.12: Time variation of ground reactions, vertical accelerations and pitching acceleration in Model B during tail-down landing

An examination of Figure 4.12 illustrates that after the MLG units make contact with the ground and reach their critical loads, they rebound. Upon approximately half a second of rebounding, the NLG makes contact with the ground, resulting in a noticeable pitch-up acceleration, as depicted by the positive $\dot{q}$. Additionally, due to the additivity of pitch-up acceleration and vertical acceleration in the nose section, the nose of the helicopter experiences the greatest acceleration during NLG contact. The static analysis model, Model A, only accounts for the initial impact of the MLG and therefore calculates only the pitch-down acceleration, leading to an underestimation of critical loads at the nose station. Thus, neglecting the impact of the NLG, which follows the impact of MLG, results in an incomplete assessment of critical loads, particularly for the nose section.

The ground reactions and accelerations of Model C are depicted in Figure 4.13 in a similar manner as Model B was analyzed.

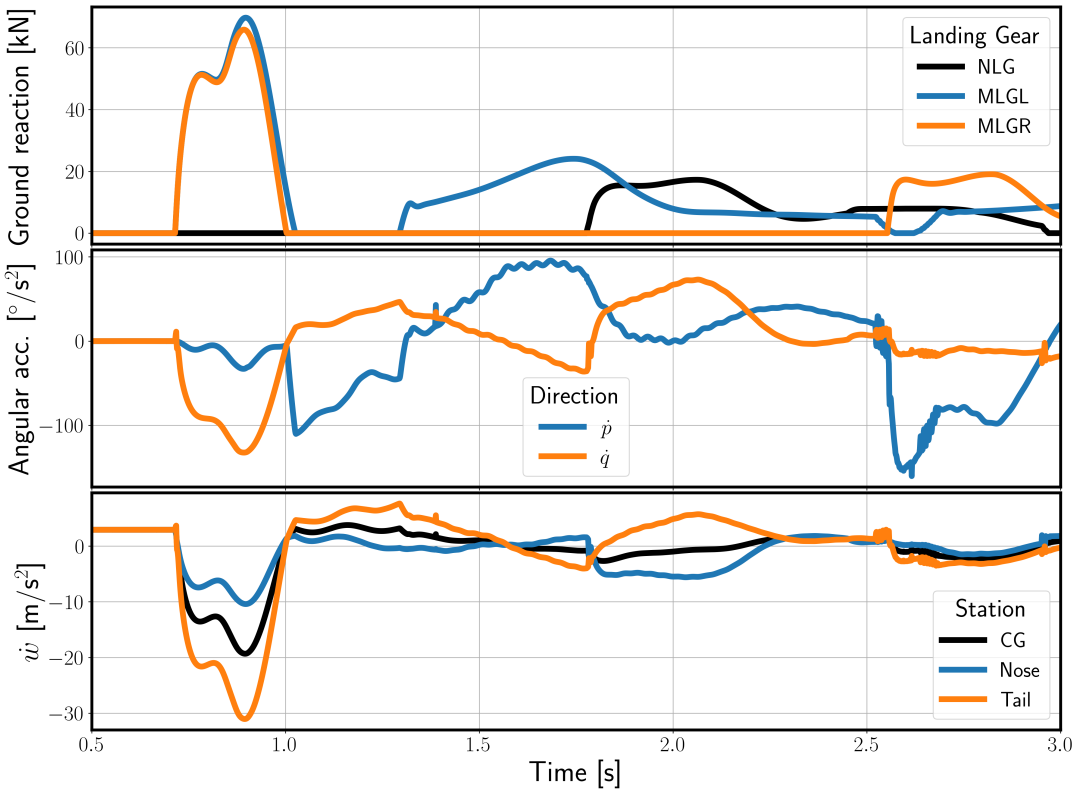


Figure 4.13: Time variation of ground reactions, vertical accelerations and angular accelerations in Model C during tail-down landing

In Figure 4.13, the ground reactions and accelerations of Model C are examined. Two notable differences compared to Model B are observed. Firstly, the MLG reactions are not symmetrical, and secondly, there is a more complex and oscillatory angular motion for Model C. This can be attributed to the pronounced effect of the rotor's gyroscopic effect during tail-down landing. The helicopter's pitch-down motion caused by the MLG touching the ground without NLG results in an increased angular velocity and more unbalanced moments acting on the system, leading to a tendency to roll left due to gyroscopic moments. After rebounding, the re-engagement of the wheels also occurs asymmetrically, leading to high rolling accelerations not present in Models B and C.

The comparison of the MLG ground reactions during the initial touchdown of the helicopter is presented in Figure 4.14 and the critical ground reactions are presented in Table 4.6.

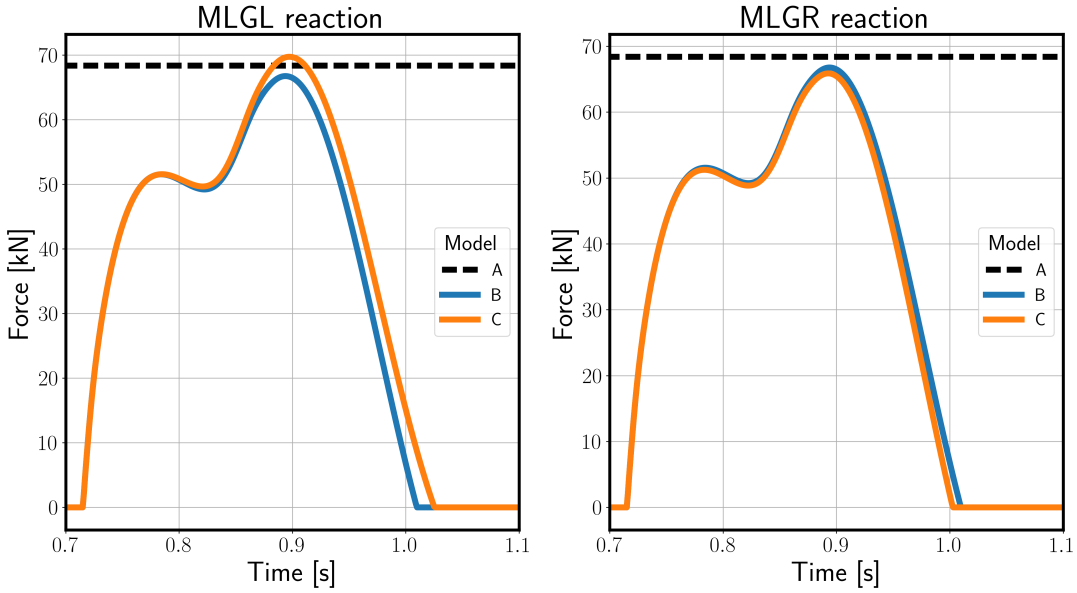


Figure 4.14: Comparison of MLG ground reactions between the models in tail-down landing

Table 4.6: Maximum ground reactions obtained in tail-down landing, in Newtons

Model	NLG	MLGL	MLGR
A	0	68381	68381
B	37726	66754	66754
C	17272	69737	65863

The low error rates observed in the computation of the MLGL and MLGR ground reactions, at 2.4% and 3.7% respectively, validate the efficacy of the inertia relief method utilized in Chapter 3.2 for the calculation of MOG. Furthermore, as depicted in Figure 4.14, asymmetrical reactions of the MLG units, caused by the gyroscopic effect, are evident and result in greater loads on the left MLG unit due to the rolling left motion of the helicopter, leading to an increase in critical ground reactions.

The comparison between the models reveals that while the NLG reaction is neglected in Model A, the results obtained from Models B and C do not concur with one another. This discrepancy is attributed to the observation that the helicopter's pitch acceleration and rate was found to be lower in Model C, resulting in a less severe contact of the NLG with the ground and thus, smaller loads acting on the NLG. The presence of the rotor, which has a substantial angular momentum, acts to resist angular disturbances and therefore results in a diminished angular response for a given moment imparted to the helicopter.

It is important to note that, although NLG reactions are disregarded in Model A, the ground reactions recorded in Models B and C are still lower than those encountered in the 3-point landing case. This highlights the fact that, as per certification standards, helicopter design must be based on multiple different loading conditions, and imperfections in one condition can be compensated by another. Hence, the omission of NLG reactions in the conventional method does not result in the critical loads going unacknowledged, as they were previously identified in the 3-point landing scenario.

The vertical and pitching accelerations acting on the CG are analyzed in Figure 4.15 and the vertical accelerations at the nose and tail stations are presented in Figure 4.16.

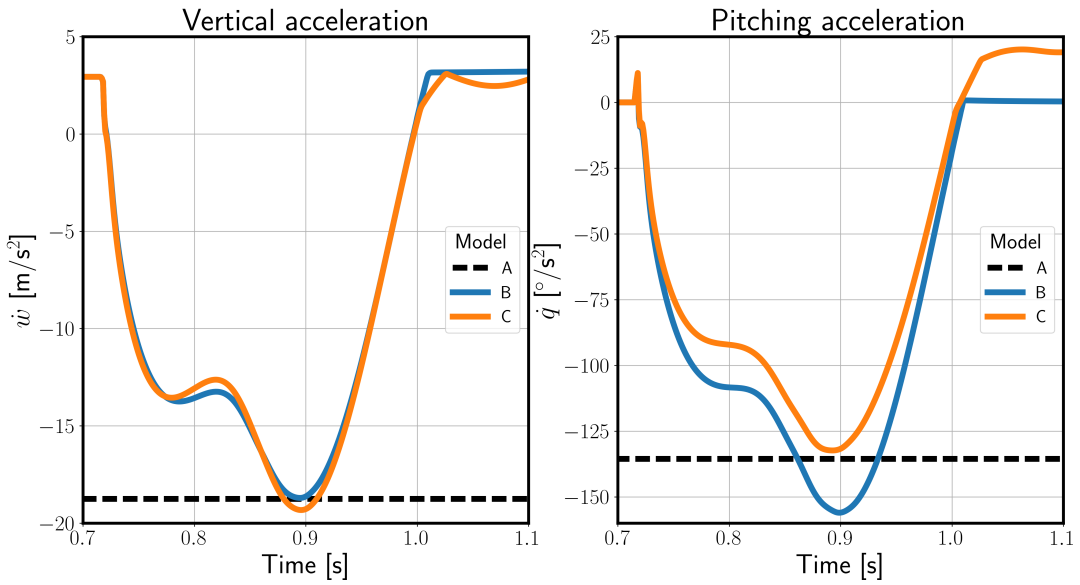


Figure 4.15: Time variation of vertical acceleration of the CG and pitching acceleration of the helicopter during tail-down landing

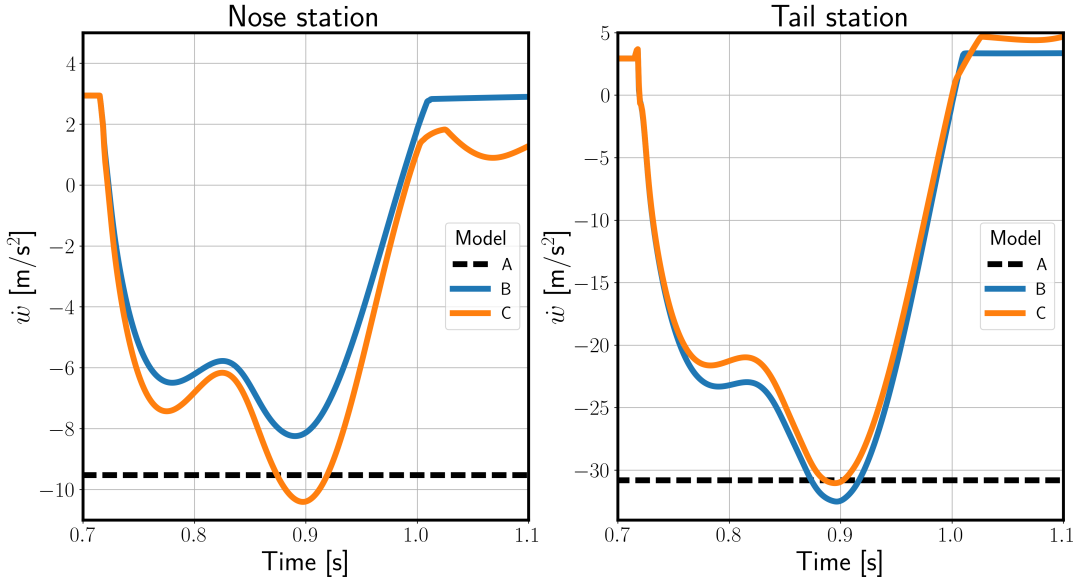


Figure 4.16: Time variation of vertical acceleration of the monitoring stations on the nose and tail sections during tail-down landing

The error rates of the CG, pitch, nose, and tail accelerations during the initial touch down are recorded as 3.2%, 15.1%, 9.5%, and 5.5%, respectively. The acceleration responses in Model C exhibit a more oscillatory behavior compared to Model B. This can be attributed to the flapping of the blades, which is depicted in Figure 4.17.

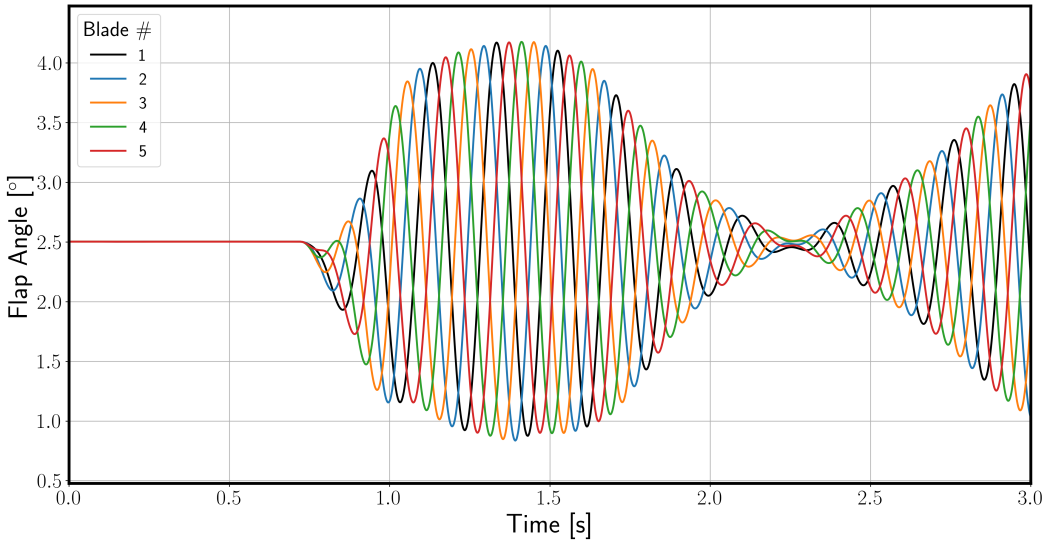


Figure 4.17: Flap response of the rotor blades in Model C during tail-down landing

In the tail-down landing scenario, a more significant flap response compared to the 3-point landing scenario was observed, with oscillations of magnitude 3 degrees. The trend of each blade was found to be the same but out of phase with each other, resulting in uneven forces across the rotor hub and generating moments on the airframe. The oscillatory behavior of the angular accelerations caused by the out-of-phase blade flapping was previously demonstrated in Figure 4.13.

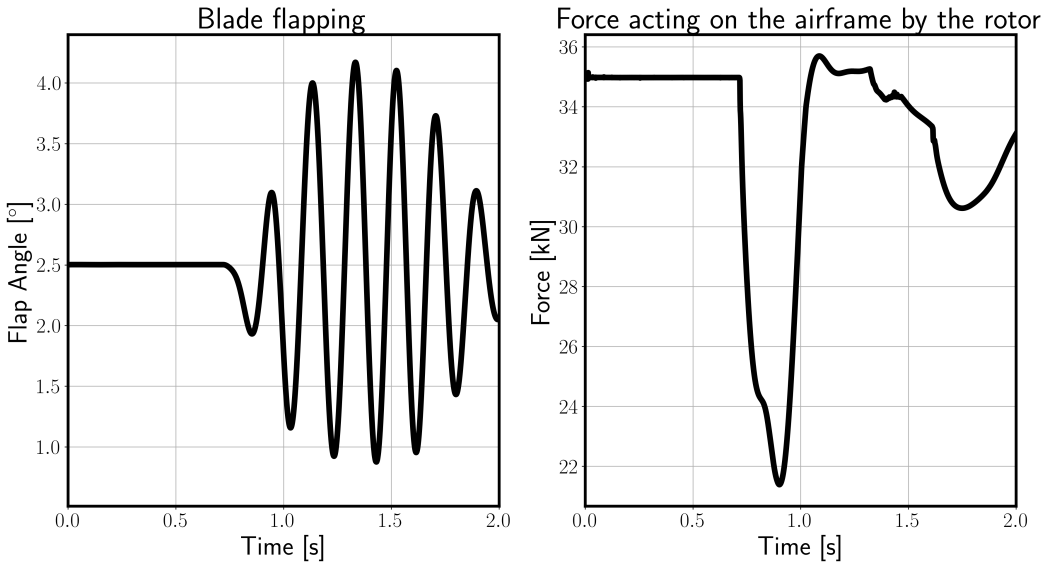


Figure 4.18: Flap response of an individual blade and rotor force acting on the airframe in Model C during tail-down landing

The flapping motion of an individual blade and the cumulative lift force transmitted to the airframe by the rotor is visualized in Figure 4.8. The decrease and subsequent rapid return to the nominal value of the lift force acting on the airframe during touch down results in greater oscillations in the acceleration terms, leading to higher critical loads. This behavior is similar to what was observed in the 3-point landing scenario, with a decrease of approximately 35% below its nominal value.

The flapping motion's effect on the aerodynamic lift during touch down can be observed in Figure 4.19.

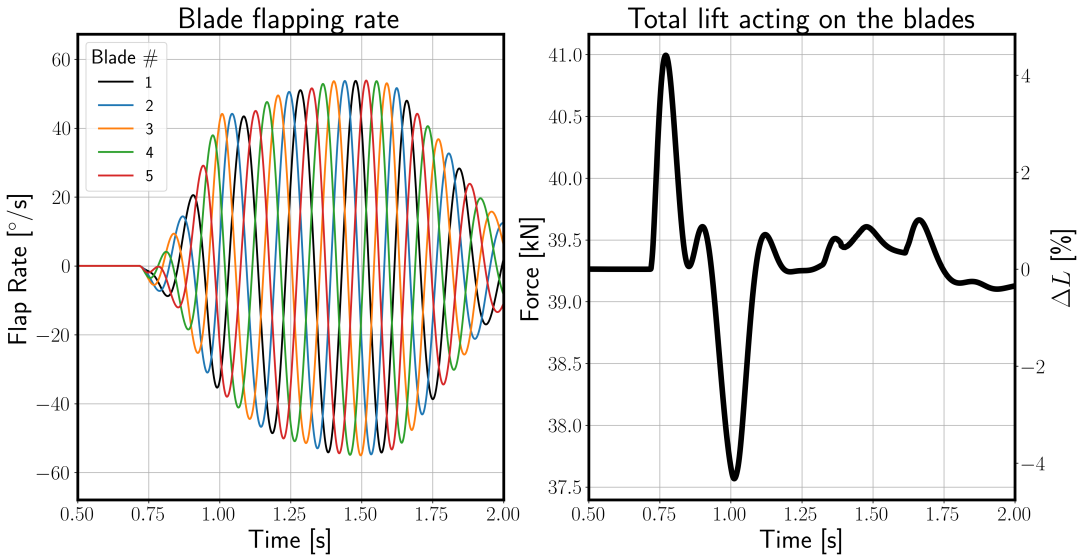


Figure 4.19: Flap rate of the blades and total aerodynamic lift acting on the blades in Model C during tail-down landing

As can be seen, despite the higher flap rates observed in tail-down landing as compared to 3-point landing, the change in total aerodynamic lift remains relatively small, at around $\pm 4\%$. This is due to the out-of-phase nature of the flap motions, which tend to cancel each other out.

As a result of the increased flapping motion of the blades, the lead-lag damper forces, depicted in Figure 4.20, are also higher in tail-down landing due to the coupling between flapping and lead-lag motions through the effect of Coriolis forces.

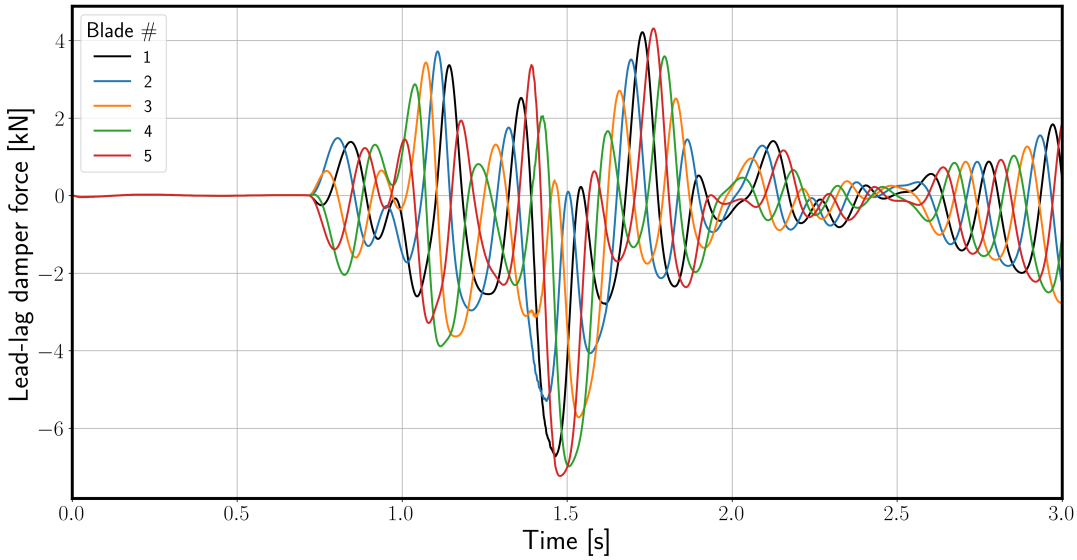


Figure 4.20: Lead-lag damper force acting on the blades in Model C during tail-down landing

Finally, a comparison was made between the ground reaction force and the force transmitted to the airframe through the landing gear attachment points. It is found that, like in the 3-point landing scenario, the shock absorber force acting on the helicopter was 3.7% less than the ground reaction force, offering valuable insights for the structural design engineer to optimize the airframe weight.

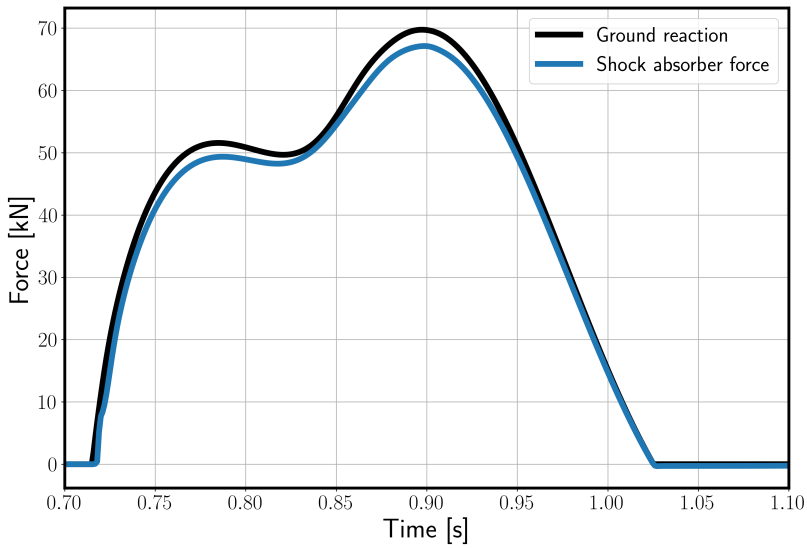


Figure 4.21: Comparison of ground reaction and shock absorber forces on left MLG unit in Model C during tail-down landing

4.3 Lateral Slope Landing

In this subchapter, the results of the lateral slope landing analysis are presented using a comparable methodology to the previous landing scenarios. This landing maneuver exhibits a more complex motion that involves both pitching and rolling on an inclined surface, as only one MLG unit initially comes into contact with the ground. The linear and angular acceleration data acquired during this maneuver can be found in Tables 4.7 and 4.8, respectively.

Table 4.7: Linear accelerations obtained in lateral slope landing. Unit is [m/s^2]

Model	**c.g.**			**Nose Station**			**Tail Station**		
	$\dot{u}$	$\dot{v}$	$\dot{w}$	$\dot{u}$	$\dot{v}$	$\dot{w}$	$\dot{u}$	$\dot{v}$	$\dot{w}$
A	0.0	1.5	-5.4	-1.9	-10.7	2.0	1.0	12.1	-15.1
B max.	1.0	2.9	3.5	2.0	12.1	3.3	3.1	11.7	4.8
B min.	-0.2	0.0	-17.1	-3.5	-9.4	-24.9	-1.1	-6.9	-13.7
C max.	0.9	3.2	3.8	2.1	10.6	4.0	3.8	9.1	4.6
C min.	-0.8	0.0	-16.5	-3.3	-7.6	-23.1	-1.0	-5.1	-13.4

Table 4.8: Angular accelerations and velocities obtained in lateral slope landing

Model	**Acceleration [°/s^2]**			**Velocity [°/s]**		
	$\dot{p}$	$\dot{q}$	$\dot{r}$	p	q	r
A	377.7	-109.2	-82.2	0.0	0.0	0.0
B max.	426.7	131.7	56.3	64.6	8.3	4.1
B min.	-355.3	-100.9	-71.0	-24.1	-8.1	-10.8
C max.	364.9	104.8	54.7	59.4	12.3	10.0
C min.	-252.4	-94.6	-57.1	-25.1	-7.7	-8.0

Upon examination of Table 4.7, it can be observed that there is a substantial error rate in almost all linear acceleration terms. In this landing scenario, vertical acceleration still remains the most dominant term, with lateral acceleration, $\dot{v}$, also being prominent in the nose and tail sections. On the other hand, examination of Table 4.8 reveals that rolling acceleration dominates among the angular accelerations, while pitching

and yawing accelerations also exhibit notable values.

In order to gain a comprehensive understanding of the dynamics of the lateral slope landing scenario, the ground reactions and accelerations of Model B have been visualized in Figure 4.22.

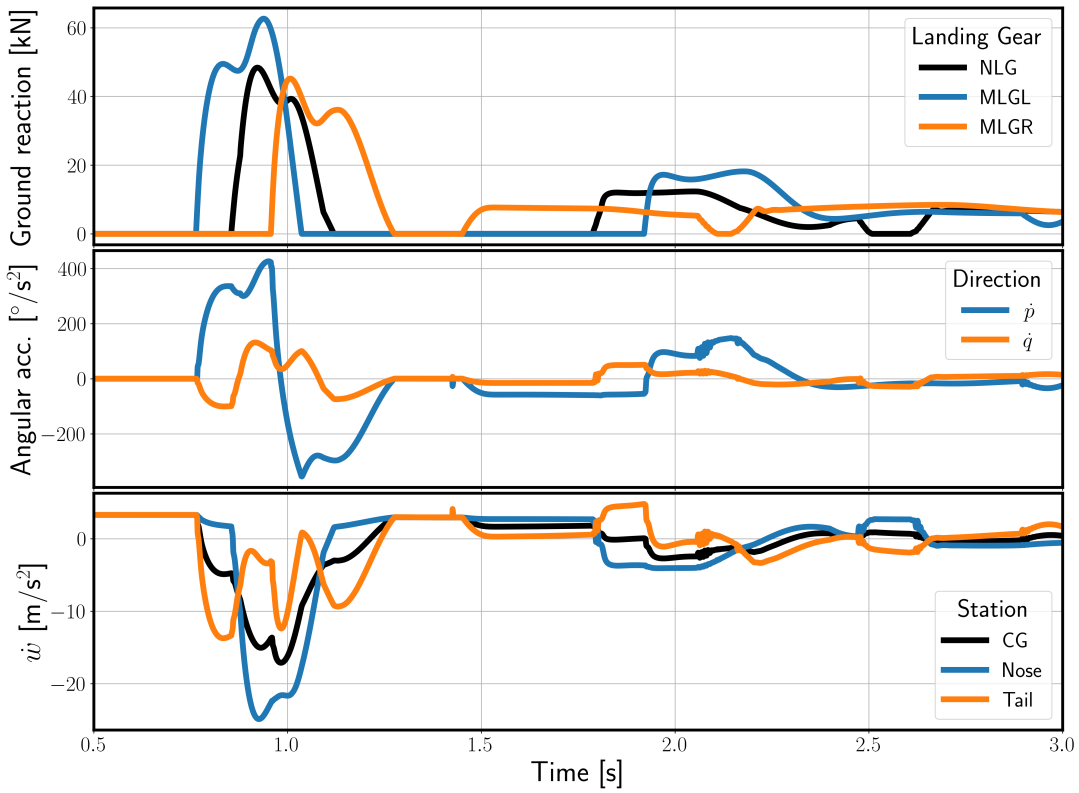


Figure 4.22: Time variation of ground reactions, vertical accelerations and angular accelerations in Model B during lateral slope landing

A review of the ground reactions indicates that prior to the MLGL reaching its maximum reaction, NLG and MLGR also touch the ground due to the aircraft's rapid rolling and pitching motion, leading to a higher overall ground reaction than that of the MLGL alone. This underprediction of $\dot{w}$ terms by Model A, which only considers the MLGL reaction, can be attributed to the additional ground contact made by the NLG and MLGR. Furthermore, as different wheels make contact with the ground at various moments during landing, unbalanced moments and shifts in direction result in high angular acceleration in both positive and negative directions. Model A, however, only captures one peak, specifically the first peak of MLGL reaction.

The comparisons of ground reactions between the models during the first touch-down event are presented in Figure 4.23.

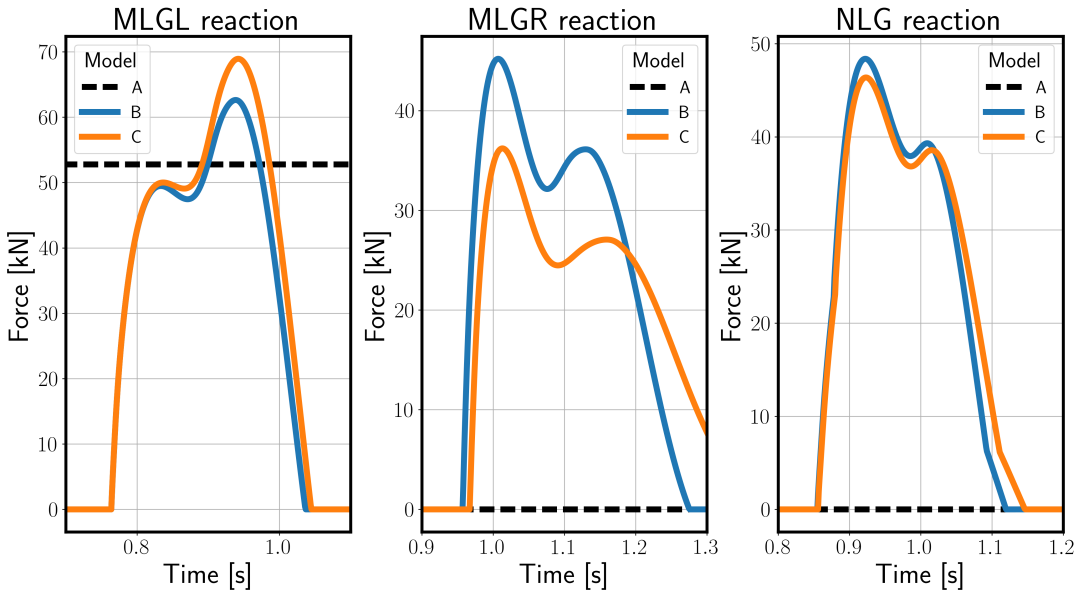


Figure 4.23: Comparison of ground reactions between the models in lateral slope landing

The application of the inertia relief method, which had proven successful in tail-down landing condition, is not effective in the current scenario. This is attributed to the method's assumption of zero angular velocity, which is not fulfilled during this landing event as indicated by the high angular velocities recorded in Table 4.8. The helicopter's geometry and mass distribution lead to a lower moment of inertia around the rolling axis, resulting in greater angular acceleration and velocity in the rolling direction for a given moment during landing. This discrepancy between the assumed zero angular velocity and the actual high angular velocities invalidates the applicability of the inertia relief method, thus contributing to the underprediction of ground reactions shown in Figure 4.23.

Additionally, the gyroscopic effect of the rotor, which causes the helicopter to roll left during pitch-down motion, can be observed in the asymmetrical MLG reactions of Model C, with the left MLG exhibiting a higher load compared to the right, resulting in a critical load on the left MLG unit.

The linear acceleration of the center of gravity and the angular acceleration of the helicopter during the lateral slope landing are depicted in Figures 4.24 and 4.25, respectively.

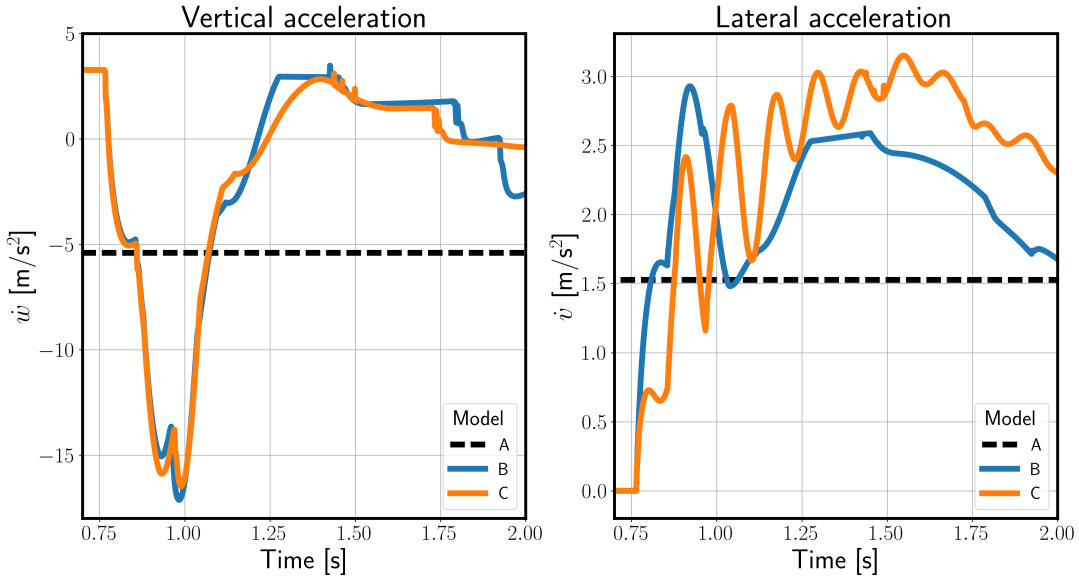


Figure 4.24: Time variation of vertical and lateral accelerations of the CG during lateral slope landing

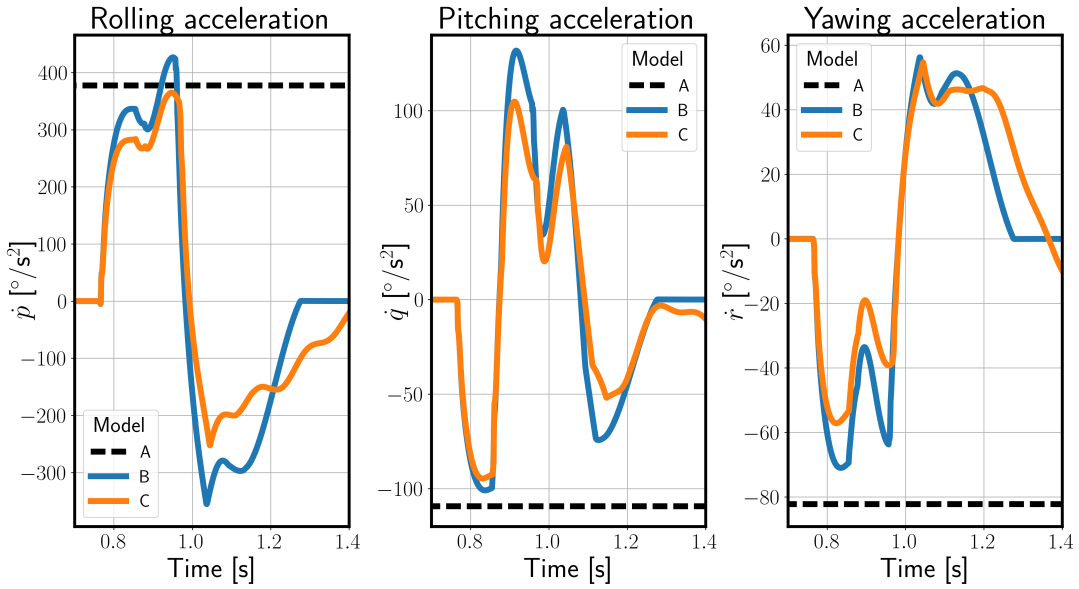


Figure 4.25: Time variation of angular accelerations of the helicopter during lateral slope landing

As depicted in Figure 4.24, while models B and C exhibit agreement in their vertical acceleration, Model A presents a significant underprediction, which can be attributed to both its underestimation of the MLGL reaction and its disregard of the ground reactions of the other two landing gear units. Similarly, the lateral acceleration, although low in magnitude, is also of significance as the helicopter's structure is designed to withstand larger loads in the vertical direction. It is imperative to note that the lateral acceleration in Model C exhibits an oscillatory behavior, a result of the oscillatory loads imposed on the airframe by the rotor. On the other hand, the results for the angular accelerations during lateral slope landing are similar to those observed during 3-point landing, with Model A unable to capture the changes in direction. However, it is crucial to consider the impact of lateral slope landing in both directions as per certification standards. While critical angular accelerations may not be accurately captured in this scenario, by analyzing the landing with the slope on the opposite side, these overlooked accelerations can be obtained and incorporated into the design of the helicopter.

Next, the vertical and lateral accelerations experienced by the nose and tail stations are analyzed and presented in Figures 4.26 and 4.27, respectively.

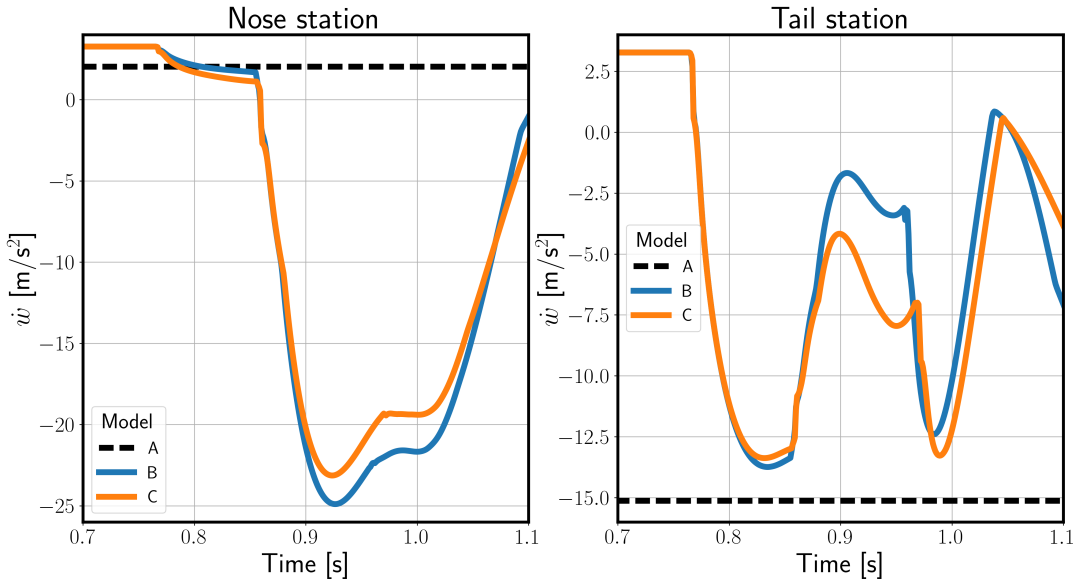


Figure 4.26: Time variation of vertical acceleration of the monitoring stations on the nose and tail sections during lateral slope landing

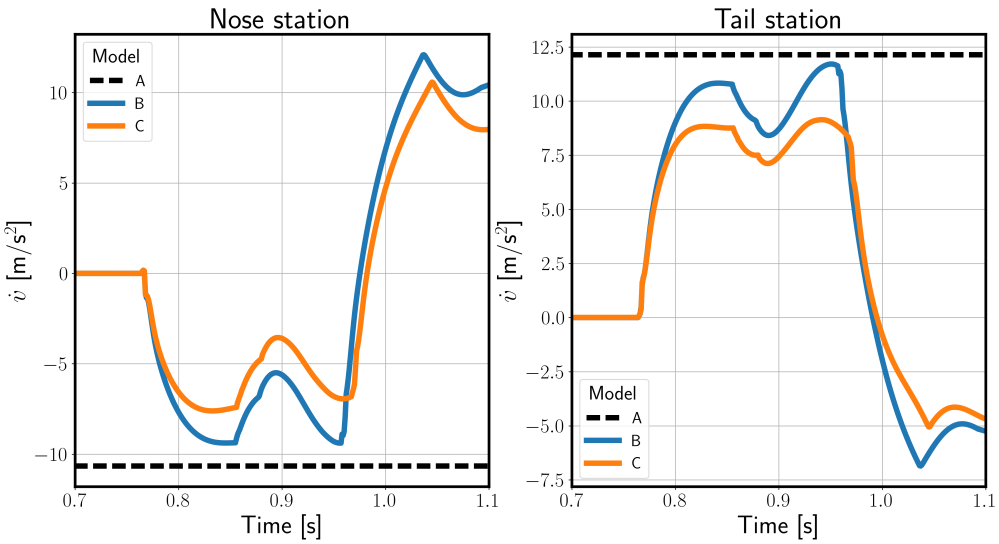


Figure 4.27: Time variation of lateral acceleration of the monitoring stations on the nose and tail sections during lateral slope landing

It is noteworthy that in the lateral slope landing scenario, the nose and tail stations experience significant lateral acceleration, a result of the yawing acceleration unique to this condition. Yawing acceleration manifests as side-to-side acceleration for these stations. The analysis shows that Model A slightly overestimates the lateral accelerations at the nose and tail stations, while Model C demonstrates lower values, due to the rotors' large angular momentum and its resistance to changes in orientation. The flap responses of the rotor blades are depicted in Figure 4.28.

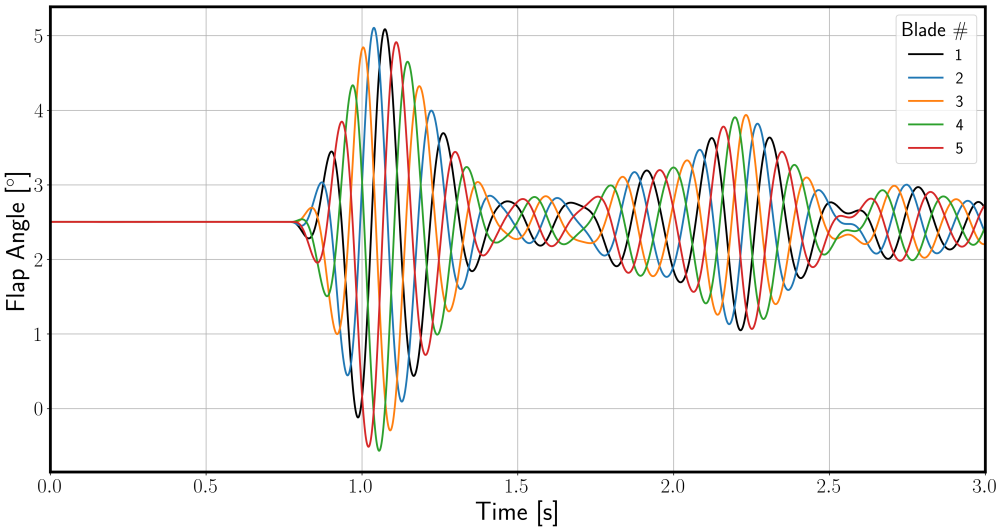


Figure 4.28: Flap response of the rotor blades in Model C during lateral slope landing

The flap response in the lateral slope landing scenario was found to be the most significant among the landing conditions analyzed. The magnitude of the oscillations was observed to be over 5 degrees. The flapping trend of each blade was found to be out of phase with each other, generating unequal and oscillatory forces on the rotor hub and applying moments on the airframe. The variations in the rotor-generated forces acting on the airframe are depicted in Figure 4.29.

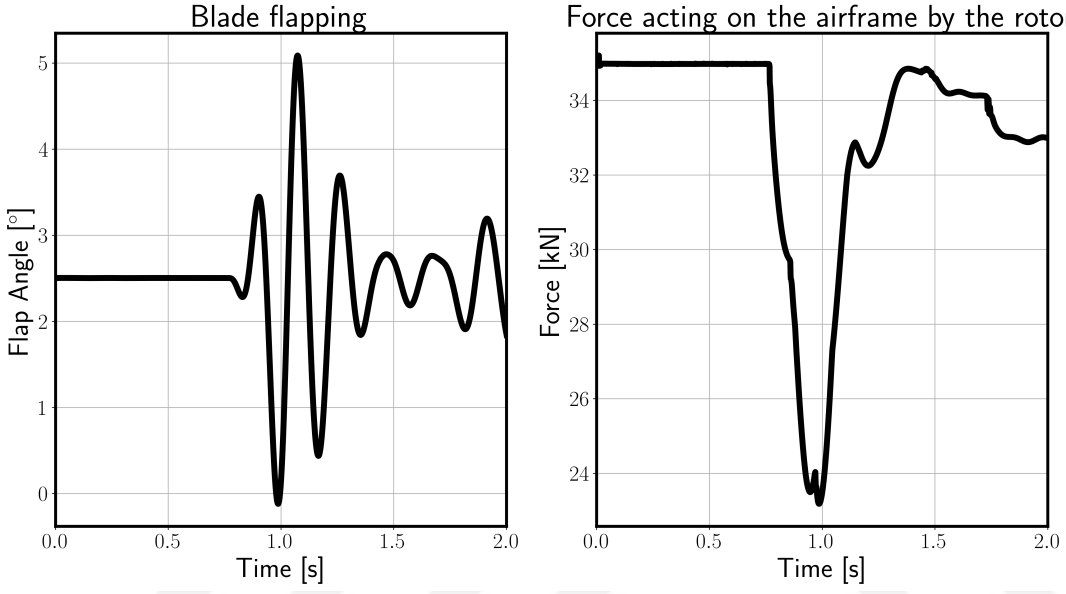


Figure 4.29: Flap response of an individual blade and rotor force acting on the airframe in Model C during lateral slope landing

The decline in the rotor force acting on the airframe in this landing scenario, followed by a swift increase to its normal value, results in more pronounced oscillatory behavior of the accelerations on the airframe. This trend is similar to that observed in previous landing scenarios.

It should also be noted that the correlation between the rotor force acting on the airframe and the vertical acceleration of the center of gravity previously presented in Figure 4.24, demonstrates the interdependence between the rotor and airframe.

The flapping rate of the blades and its impact on the total aerodynamic lift acting on the blades is presented in Figure 4.30.

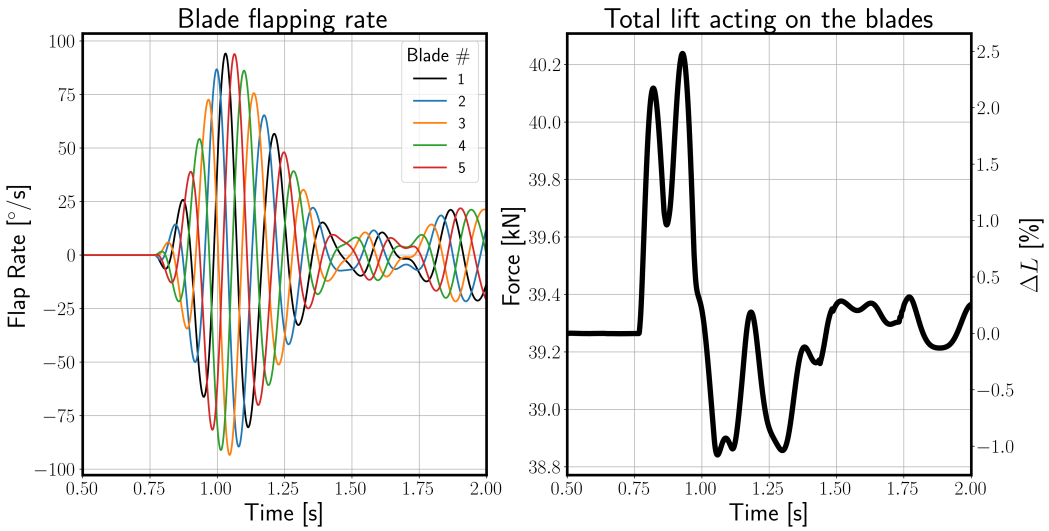


Figure 4.30: Flap rate of the blades and total aerodynamic lift acting on the blades in Model C during lateral slope landing

Despite the high rate of blade flapping, the overall aerodynamic lift experienced by the blades only experienced a 3.5% change. This was attributed to the out-of-phase motion of the blades, where the additional lift experienced by one blade was canceled out by the reduced lift experienced by another blade. The alteration in the lead-lag damper forces, as a result of flapping, and its consequent impact on the lead-lag motion of the blades are depicted in Figure 4.31.

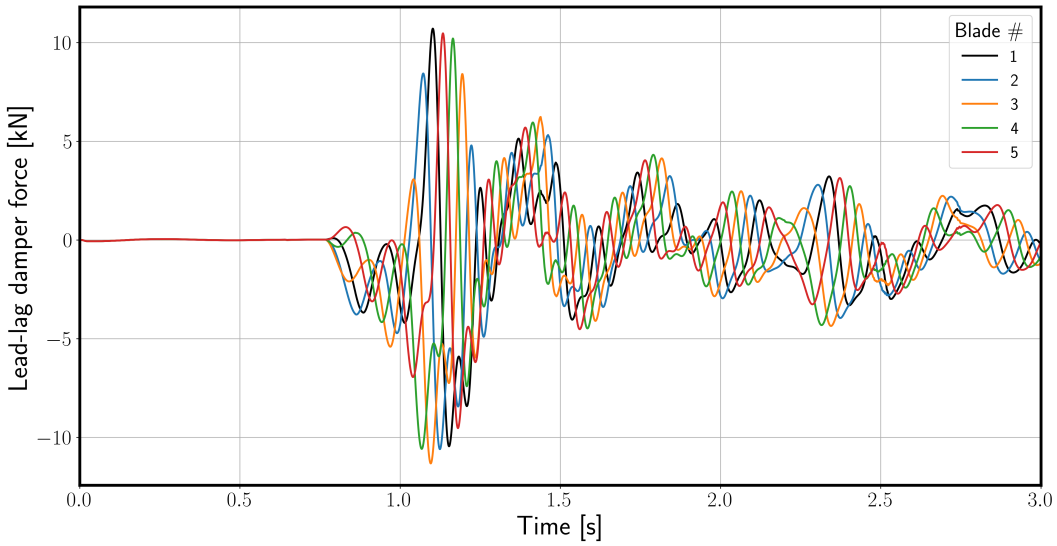


Figure 4.31: Lead-lag damper force acting on the blades in Model C during lateral slope landing

The comparison between the shock absorber force that acts on the airframe and the ground reaction that acts on the landing gear tire during a lateral slope landing scenario is depicted in Figure 4.32. The results obtained align with previous findings, as the ground reaction was determined to be 3.3% greater than the shock absorber force. This highlights the potential for a lighter airframe structure design, if the design is made based on the shock absorber force instead of the ground reaction.

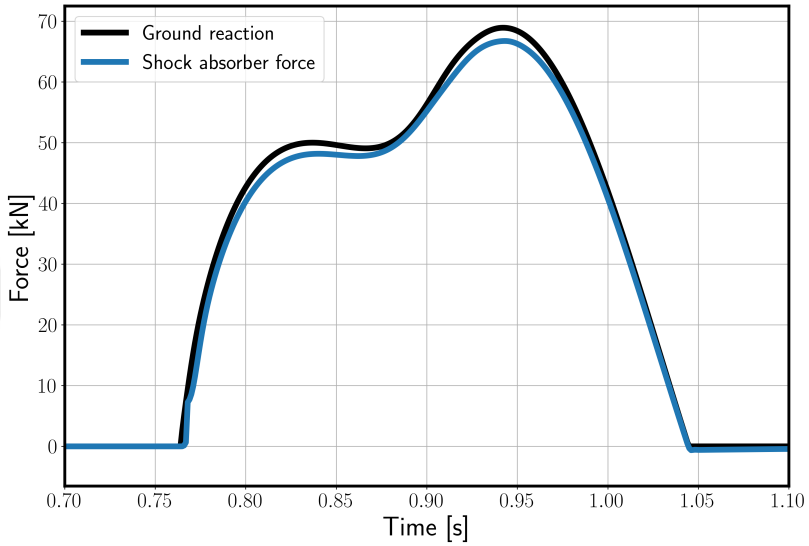


Figure 4.32: Comparison of ground reaction and shock absorber forces on left MLG unit in Model C during lateral slope landing

4.4 Running Landing

In this subchapter, the results of the running landing analyses are presented, utilizing a distinct approach compared to the previous landing cases. The load analysis for this landing maneuver is performed to validate the loads during spin-up, which represents the peak drag load experienced by the landing gears. According to CS 29.479(b)(3), the loads to be analyzed for this maneuver should comprise of the peak drag load at the moment of spin-up and the corresponding vertical force. Given that the drag force acts along the longitudinal axis of the helicopter, this load condition differs from previous landing cases, where ground reactions acted nearly perpendicular. Therefore, in the evaluation of the results for this analysis, only the results up to the spin-up event are considered, instead of the complete time history. This aligns with the static

analysis method employed for this landing condition, which focuses on the spin-up event loads as described in Chapter 3.4.

The maximum and minimum values of linear and angular accelerations until the spin-up moment are presented in Tables 4.9 and 4.10, respectively.

Table 4.9: Linear accelerations obtained in running landing. Unit is [m/s^2]

Model	**c.g.**			**Nose Station**			**Tail Station**		
	$\dot{u}$	$\dot{v}$	$\dot{w}$	$\dot{u}$	$\dot{v}$	$\dot{w}$	$\dot{u}$	$\dot{v}$	$\dot{w}$
A	-8.0	0.0	-11.2	-11.4	0.0	2.2	-6.2	0.0	-28.7
B max.	0.0	0.0	3.3	0.8	0.0	5.2	0.0	0.0	3.3
B min.	-9.3	0.0	-14.1	-12.5	0.0	-17.6	-7.9	0.0	-29.2
C max.	0.4	0.0	3.3	1.3	0.2	5.1	0.0	0.0	3.3
C min.	-9.6	0.0	-14.7	-12.1	0.0	-18.6	-7.8	-0.1	-28.6

Table 4.10: Angular accelerations and velocities obtained in running landing

Model	**Acceleration [°/s^2]**			**Velocity [°/s]**		
	$\dot{p}$	$\dot{q}$	$\dot{r}$	p	q	r
A	0.0	-196.5	0.0	0.0	0.0	0.0
B max.	0.0	51.6	0.0	0.0	0.0	0.0
B min.	0.0	-176.5	0.0	0.0	-2.6	0.0
C max.	0.0	57.2	1.3	0.0	0.0	0.0
C min.	-7.1	-163.4	-0.1	-0.1	-2.4	0.0

As demonstrated in Table 4.9, the results of the running landing scenario indicate that while vertical acceleration remains dominant, longitudinal acceleration ($\dot{u}$) is also substantial and surpasses the values obtained in previous landing cases. Additionally, the angular acceleration data in Table 4.10 shows that for Models A and B, angular acceleration is primarily in the pitch direction, whereas for Model C there is a non-zero component in the roll direction. This pitch down acceleration is a predictable outcome of the running landing scenario, as the drag forces acting on the wheels generate a pitch-down moment on the helicopter.

Table 4.11 displays the ground reactions at the moment of spin-up.

Table 4.11: Maximum ground reactions obtained in running landing, in Newtons

Model	**Drag, F_D**			**Vertical, F_V**		
	NLG	MLGL	MLGR	NLG	MLGL	MLGR
A	12862	17443	17443	23386	31715	31715
B	18853	18880	18880	35093	34997	34997
C	18784	18854	18852	34944	34948	34941

A comparison of the results of Models B and C reveals that they produce nearly identical results, with differences within 0.4% of each other. However, Model A shows higher error rates in the drag direction for the NLG, with an error rate of 46%, and 8% for both MLGL and MLGR. In the vertical direction, Model A has an error rate of 50% for NLG and 10% for both MLGL and MLGR. To further analyze these results, the time histories of ground reactions up to the spin-up event are depicted in Figures 4.33 and 4.34.

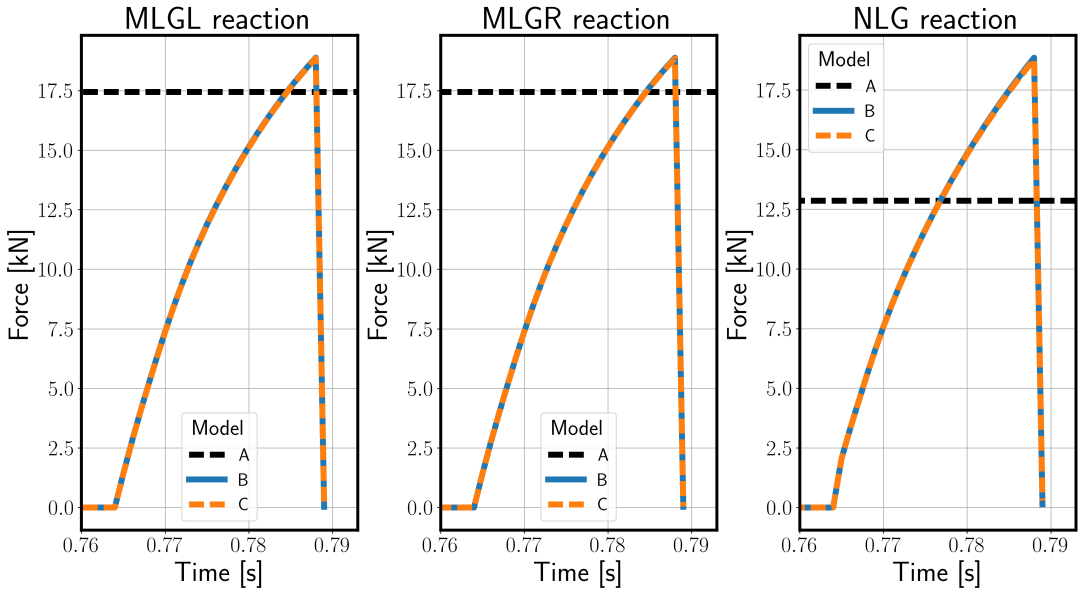


Figure 4.33: Comparison of longitudinal ground reactions between the models in running landing

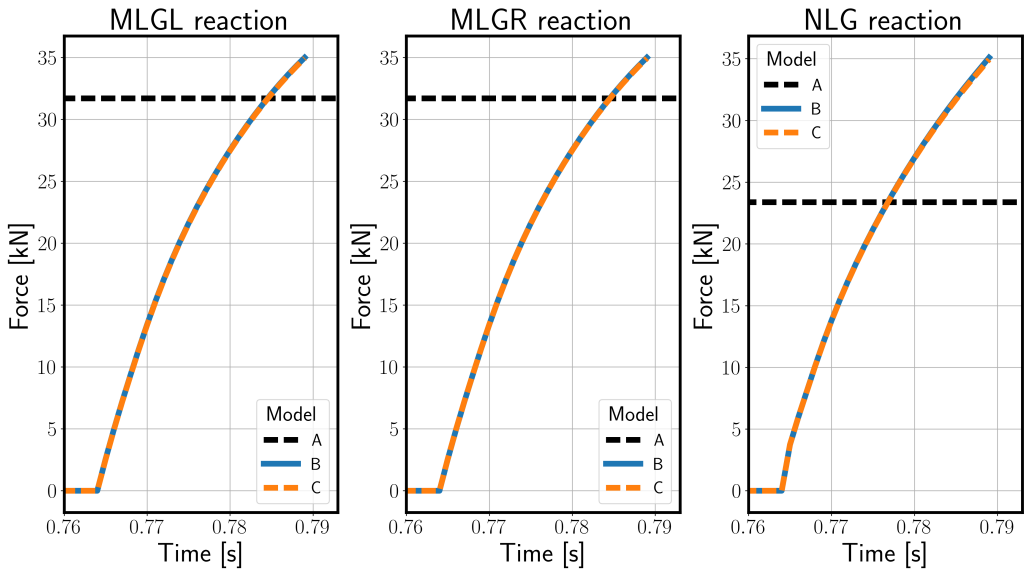


Figure 4.34: Comparison of vertical ground reactions between the models in running landing

As indicated in Figure 4.33, the longitudinal ground reaction, which represents the drag force, attains its maximum value before instantly reducing to zero, as hypothesized in Chapter 3.4. It is important to note that, as the drag force is the product of the vertical force and a constant friction coefficient in each model, the error rates in both the drag and vertical ground reactions are found to be equivalent.

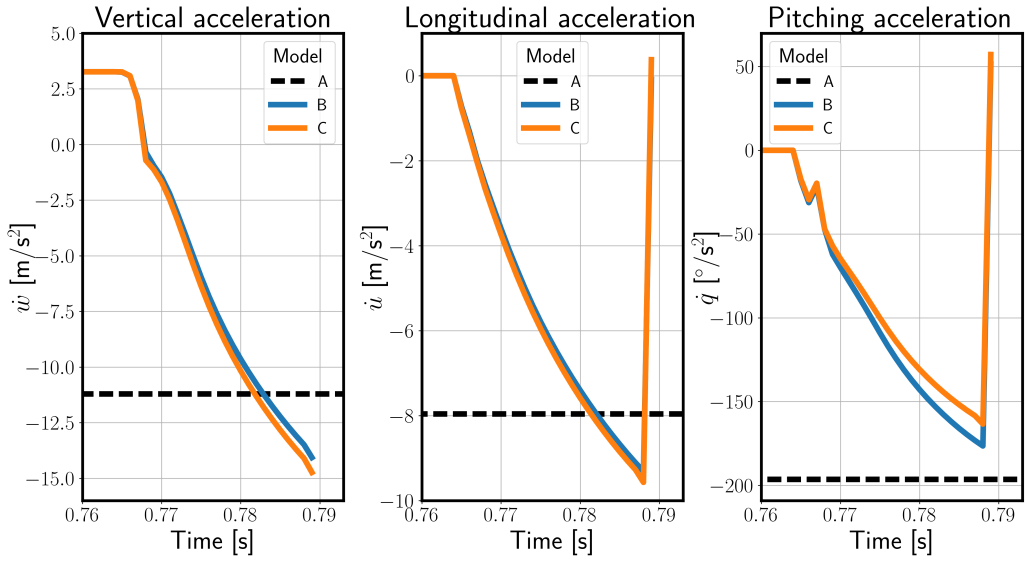


Figure 4.35: Time variation of vertical, longitudinal and pitching accelerations during running landing

The results of Model A show underprediction of both longitudinal and vertical accelerations, and overprediction of pitching acceleration. This discrepancy is due to the static nature of Model A, which assumes forces are applied at a fixed position of the helicopter, while Models B and C incorporate the time-dependent effect of forces as per the definition of a dynamic system. As the drag forces are applied on the helicopter, they cause it to pitch down, which results in a transfer of weight from the MLG to the NLG, leading to an increase in the NLG's vertical force and a decrease in pitching moment. The underprediction of NLG ground reactions in Model A are also mostly attributed to the absence of the actual pitch down motion of the helicopter.

In this landing scenario, it has been observed that Models B and C exhibit identical trends in their ground reactions, indicating that the effect of rotor dynamics on these reactions is not significant. Nonetheless, slight differences in the acceleration terms between the models B and C suggest that the rotor may still play a role in determining airframe loads.

The acceleration experienced in the vertical and longitudinal directions by the nose and tail stations is depicted in Figures 4.36 and 4.37, respectively.

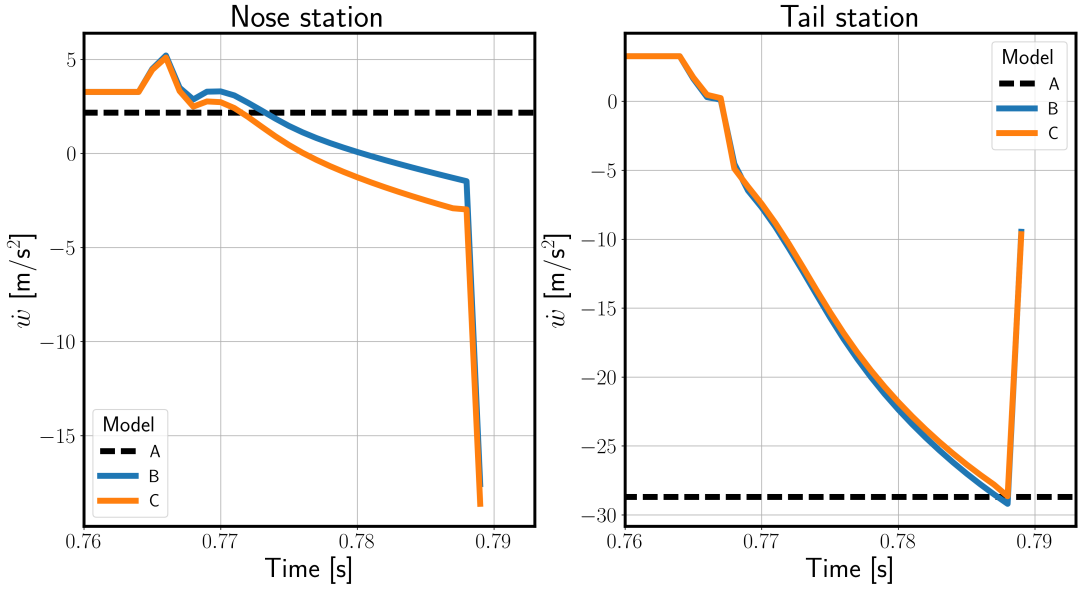


Figure 4.36: Time variation of vertical acceleration of the monitoring stations on the nose and tail sections during running landing

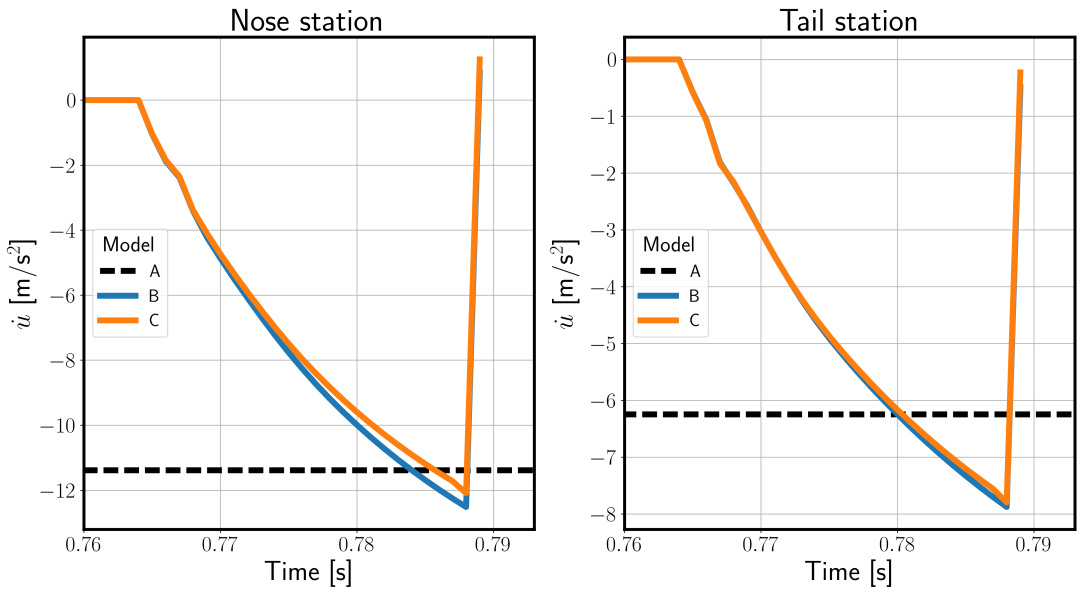


Figure 4.37: Time variation of longitudinal acceleration of the monitoring stations on the nose and tail sections during running landing

The error rates in the nose and tail section accelerations are consistent with the error rates observed in the ground reactions. The results from Model A exhibit varying degrees of discrepancy compared to those from Models B and C. Given that the equations governing the spin-up event for Model A were derived under specific assumptions, the validity of these assumptions must be critically evaluated.

One of the initial assumptions underlying the development of Model A was that the maximum ground reaction experienced by a landing gear during a running landing would be equivalent to the ground reaction experienced by that same gear during a purely vertical, three-point landing. The validity of this assumption was evaluated by comparing the ground reactions obtained from the spin-up and 3-point landing analysis using Model C, as illustrated in Figure 4.38.

The second assumption was that the MOG would exhibit only vertical motion and the ground reactions on each landing gear would reach their maximum values at a specific time following a sinusoidal pattern. The validity of the assumption can be evaluated by examining the evolution of ground reactions until the maximum values are reached, which are depicted in Figures 4.39 and 4.40 for each model.

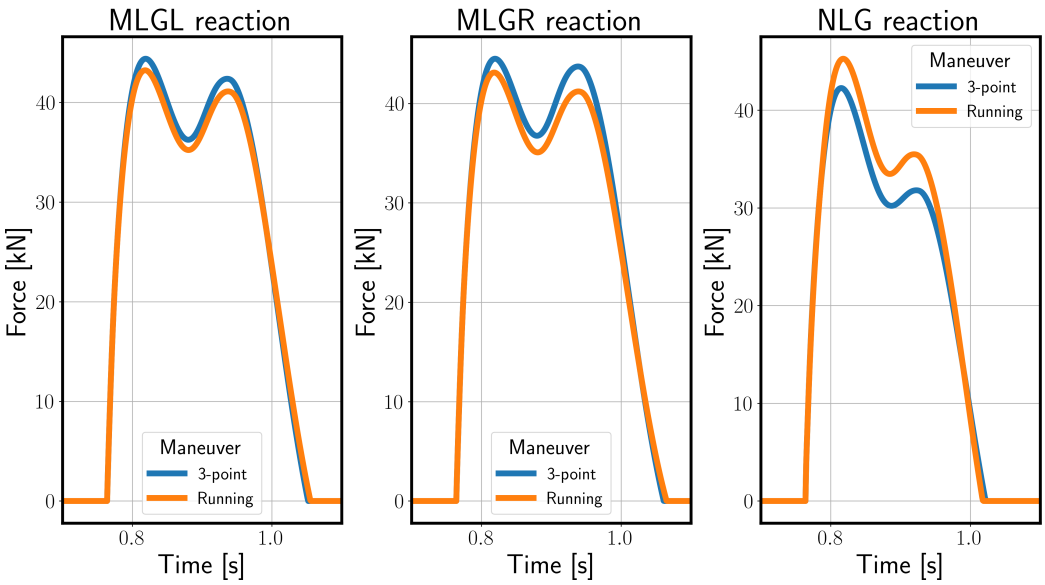


Figure 4.38: Comparison of vertical ground reactions between the 3-point and running landing maneuvers, in Model C

It is determined that the assumption that the ground reactions obtained in running and 3-point landing analyses would be equal is incorrect. This is due to the previously noted pitching motion of the helicopter, leading to an increase in load on NLG and a reduction in load on MLG.

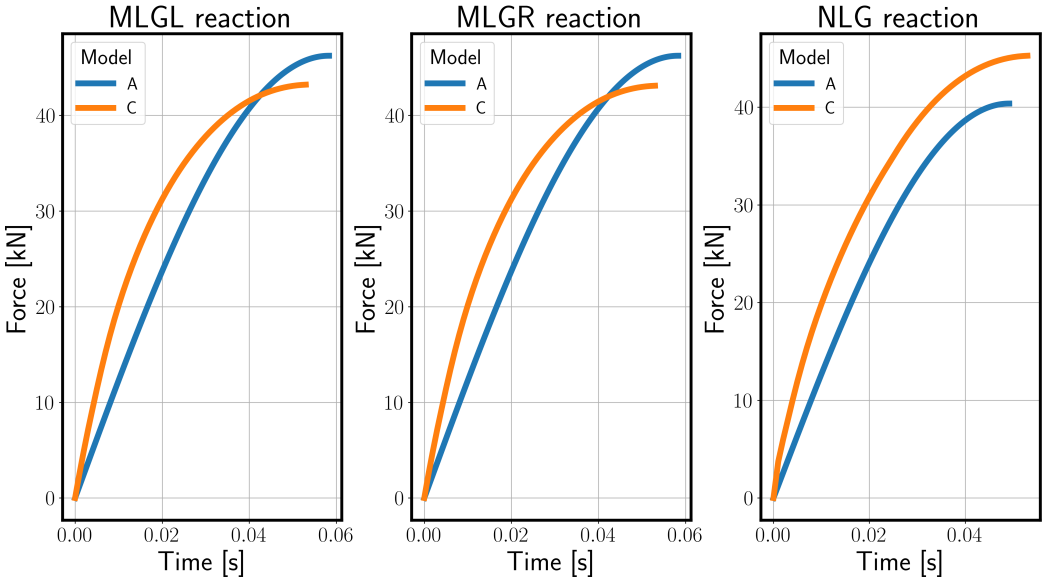


Figure 4.39: Evolution of vertical ground reactions to their maxima in running landing for models A and C

The assumption of ground reactions following a sinusoidal pattern is partially supported by the results, however, the previously established assumption of equal ground reactions in both 3-point and running landings was shown to be invalid, leading to inaccurate estimation of the ground reactions.

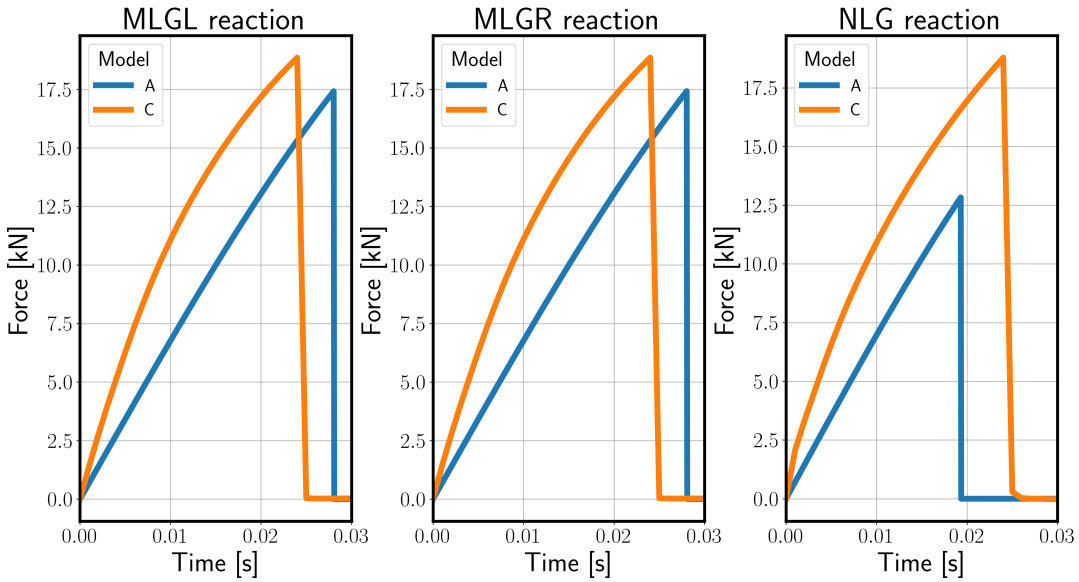


Figure 4.40: Evolution of longitudinal ground reactions to their maxima in running landing for models A and C

The conclusion of the study regarding the assumptions made in the derivation of the spin-up event for Model A reveals that these assumptions resulted in large discrepancies in the longitudinal ground reaction, specifically in the drag force. It was determined that the primary source of these inaccuracies was the incorrect assumption of equal ground reactions in both 3-point and running landing analyses, while the assumption of a sinusoidal pattern in the evolution of ground reactions was partially validated.

In continuation, the impact of the rotor on the loads experienced during the running landing event is evaluated. Again, only the temporal progression of the results leading up to the spin-up event is analyzed. The flapping response of the blades is depicted in Figure 4.41.

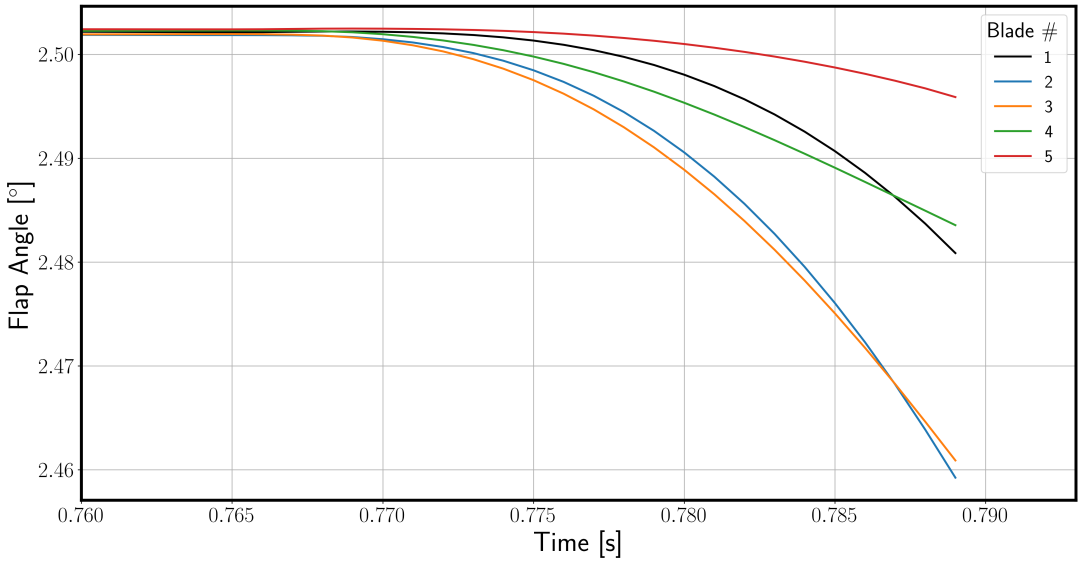


Figure 4.41: Flap response of the rotor blades in Model C during running landing

It can be observed that the blades exhibit only minimal flapping motion, with a displacement of only 0.04 degrees. The variation in the rotor force acting on the airframe during the spin-up event is displayed in Figure 4.42.

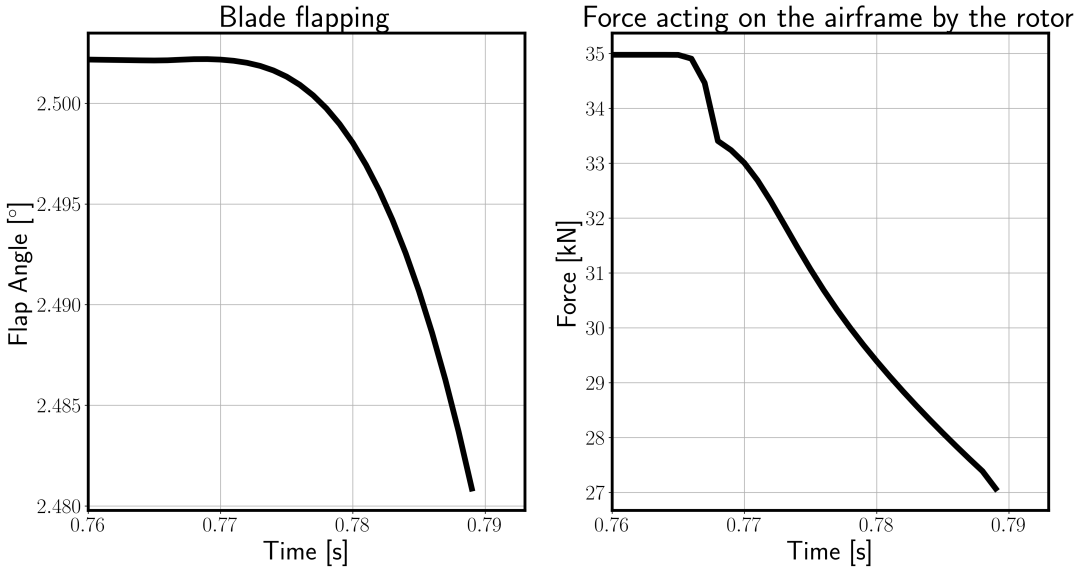


Figure 4.42: Flap response of an individual blade and rotor force acting on the airframe in Model C during running landing

The rate of blade flapping and the total aerodynamic lift acting on the blades are presented in Figure 4.43.

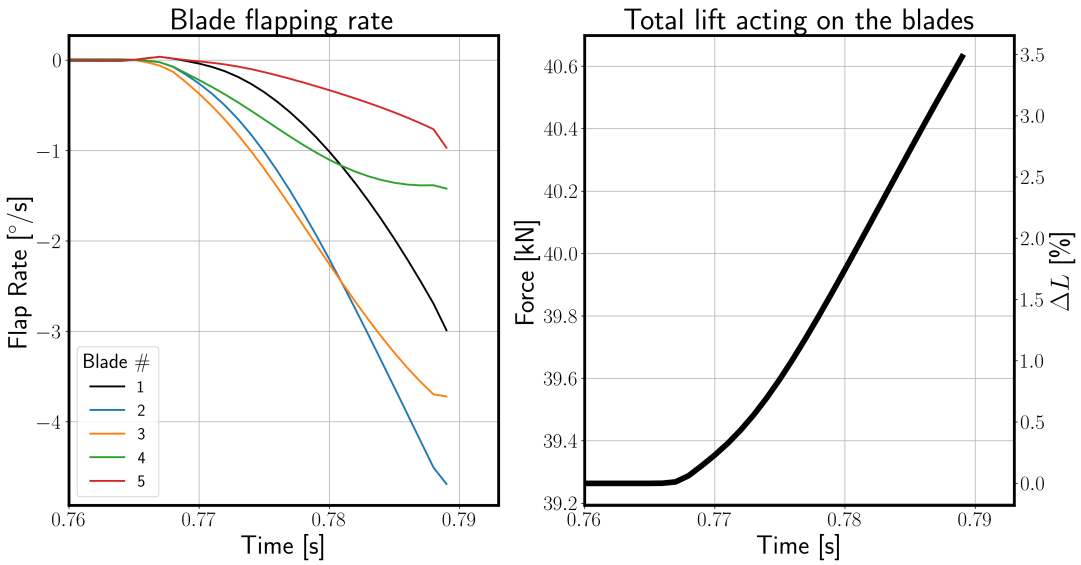


Figure 4.43: Flap rate of the blades and total aerodynamic lift acting on the blades in Model C during running landing

In conclusion, it has been found that the effect of rotor dynamics during a running landing is minimal, particularly during the spin-up event. This is due to the short time frame of the spin-up event, which lasts approximately 25 milliseconds, and the rotor dynamics taking a longer period of time to manifest. Hence, it can be inferred that the rotor dynamics do not significantly influence the results of the running landing analysis.

CHAPTER 5

CONCLUSIONS

In this comprehensive study, two multi-body dynamics models of a helicopter were developed, one including the landing gear and airframe, and the other incorporating the main rotor in addition. The simulation of four different landing conditions, namely 3-point, tail-down, lateral slope, and running landing, were performed using these models. The resulting ground reaction forces on the landing gears, angular velocities and accelerations of the airframe, and linear accelerations in the center of gravity, nose, and tail regions of the helicopter were analyzed and compared with the results of the static analysis method commonly used in the industry and deemed acceptable for certification by agencies such as EASA and FAR. Additionally, the impact of rotor dynamics on the landing problem was also investigated, highlighting important findings.

The present study demonstrates that the rotor's gyroscopic effect plays a crucial role in determining the critical loads of the landing gears, except in the case of running landings. This effect arises from the angular momentum of the rotor, which couples the rolling and pitching motions of the helicopter, leading to unequal loads on the main landing gears and higher critical loads on one of the landing gear units. The gyroscopic effect was observed to be particularly pronounced in tail-down and lateral slope landings, where the higher angular velocities contribute to its magnitude.

In all landing scenarios analyzed, with the exception of the running landing, the flapping degree of freedom of the blades emerged as a significant contributor to the loads on the airframe. Upon contact with the ground, the blades tend to flap downward, leading to a rapid reduction of the rotor force acting on the airframe and invalidating

the commonly made assumption of constant lift during the landing process. The results of the study showed that the aerodynamic forces acting on the blades are subject to fluctuations during the flapping motion. This, in turn, causes oscillations in the force acting on the airframe and results in the occurrence of critical loads.

In the 3-point landing scenario, results of the multi-body dynamics models demonstrated concurrence with the conventional method in terms of ground reactions, while some moderate discrepancies were identified in the accelerations of the nose and tail sections, which reflect the airframe loads. These disparities are attributed to the limitations of the conventional static analysis method, which is widely accepted in the literature but fails to accurately capture the changes in angular accelerations that occur during the landing phase due to its inherently static nature.

In tail-down and lateral slope landing scenarios, the conventional approach focuses on only considering the ground reactions on the landing gear units that make initial contact with the ground. However, the results of this study demonstrate that the secondary ground contacts from the other landing gears can also give rise to critical loads, thus highlighting the limitations of the traditional method and reinforcing the importance of considering all landing gear units in analysis of these maneuvers.

The findings of the running landing analysis showed that rotor dynamics during the spin-up event had a minimal impact on the results. This is because the spin-up event lasts only about 25 milliseconds and rotor dynamics take longer to manifest. Despite this, there were still significant deviations in the ground reactions and airframe loads in running landing. The study discovered that the conventional method's assumptions in the calculation of the spin-up event caused significant errors in the longitudinal ground reactions, primarily due to the false assumption of equal ground reactions in both 3-point and running landing scenarios.

Incorporating the principles of elasticity, particularly in regards to the helicopter's airframe, alongside the addition of rotor dynamics, could result in a more accurate and high-fidelity landing analysis, leading to optimized structural design, according to the study's author.

REFERENCES

[1] R. E. Benton. Structural integrity challenges for future rotorcraft programs. In *Vertical Flight Society 76th Annual Forum*, 2020.

[2] European Union Aviation Safety Agency (EASA). *Certification Specifications, Acceptable Means of Compliance and Guidance Material for Large Rotorcraft*, amendment 10 edition, 2021.

[3] W. R. Krüger and M. Morandini. Numerical simulation of landing gear dynamics: State-of-the-art and recent developments. In *NATO Research and Technology Organisation (RTO) Applied Vehicle Technology Panel (AVT) Symposium*, 2008.

[4] D. Cristiani, L. Colombo, W. Zielinski, C. Sbarufatti, F. Cadini, M. Dziendzikowski, and M. Giglio. On the evaluation of a coupled sequential approach for rotorcraft landing simulation. *Sensors*, 20(9), 2020.

[5] J. L. Nicholas. Advanced dynamic simulation for determination of landing gear loads. In *AHS International Forum 63*, Virginia Beach, VA, 2007.

[6] B. McClintick and R. Darlington. Unique methodology used in the bell-boeing v-22 main landing gear landing loads analysis and drop tests. In *Vertical Flight Society 45th Annual Forum*, Boston, Massachusetts, USA, 1989.

[7] G. Vallone, A. Manes, C. Sbarufatti, and M. Giglio. Helicopter harsh landing events: A computational hybrid methodology to estimate fuselage damage. *Journal of Aircraft*, 50(6):1896–1907, 2013.

[8] B. İ. Özturan. Multibody simulation of helicopter rotor with structural flexibility. Master's thesis, Middle East Technical University, 2019.

[9] D. Guivarch, E. Mermoz, and Y. Marino. A new modeling framework to predict helicopter dynamic systems loads. In *AHS International Forum 74*, Phoenix, Arizona, USA, 2018.

[10] H. Lee, S. R. Viswamurthy, S. C. Park, T. Kim, S. J. Shin, and D. Kim. Helicopter rotor load prediction using a geometrically exact beam with multicomponent model. *Journal of Aircraft*, 47(4):1382–1390, 2010.

[11] J. Stanisławski. A simulation model for computing the loads generated at landing site during helicopter take-off or landing operation. *Transactions on Aerospace Research*, Nr 2 (255):65–81, 2019.

[12] L. Dong, P. Hou, and W. Yang. Aeroelastic analysis of rotor/fuselage/landing gears coupled system of helicopter during rotor starting process on ground. In *1st Asian Australian Rotorcraft Forum and Exhibition*, BEXCO, Busan, Korea, 2012.

[13] G. Holmes, P. Sartor, S. Reed, P. Southern, K. Worden, and E. Cross. Prediction of landing gear loads using machine learning techniques. *Structural Health Monitoring*, 15(5):568–582, 2016.

[14] B. Miltzwitzky and D. C. Lindquist. *Evaluation of the Reduced-Mass Method of Representing Wing-Lift Effects in Free-Fall Drop Tests of Landing Gears*. National Advisory Committee For Aeronautics (NACA), Langley Aeronautical Laboratory, Langley Field, Va., 1951.

[15] NATO - Advisory Group For Aerospace Research & Development (AGARD), 7 Rue Ancelle, 92200 Neuilly-Sur-Seine, France. *Helicopter/Weapon System Integration*, 1997.

[16] R. Pecora. A rational numerical method for simulation of drop-impact dynamics of oleo-pneumatic landing gear. *Applied Sciences*, 11(9), 2021.

[17] S. Du, C. Zhang, K. Zhou, and Z. Zhao. Study of the two-phase flow characteristics of a damping orifice in an oleo-pneumatic shock absorber. *Fluids*, 7(12), 2022.

[18] W. R. Krüger and M. Morandini. Recent developments at the numerical simulation of landing gear dynamics. *CEAS Aeronautical Journal*, 1:55–68, 2011.

[19] J. R. Wright and J. E. Cooper. *Introduction to Aircraft Aeroelasticity and Loads*. John Wiley & Sons Ltd, The Atrium, Southern Gate, Chichester, West Sussex PO19 8SQ, England, 2007.

[20] D. Howe. *Aircraft Loading and Structural Layout*. Professional Engineering Publishing, London and Bury St Edmunds, UK, 2004.

[21] T. L. Lomax. *Structural Loads Analysis for Commercial Transport Aircraft: Theory and Practice*. American Institute of Aeronautics and Astronautics, Inc., 1801 Alexander Bell Drive, Reston, VA 22091, 1996.

[22] N. S. Currey. *Aircraft Landing Gear Design: Principles and Practices*. American Institute of Aeronautics and Astronautics, Inc., 370 L'Enfant Promenade, S.W., Washington, D.C. 20024, 1988.

[23] F. Yıldız. An algorithm for designing nonlinear springs, or nonlinear dampers, using a mechanical force generator and its application to an aircraft landing gear. Master's thesis, Middle East Technical University, 2021.

[24] R. K. Schmidt. *Advances in Aircraft Landing Gear*. SAE International, 400 Commonwealth Drive, Warrendale, PA 15096, USA, 2015.

[25] B. Miltzwitzky and F. E. Cook. *Analysis of Landing Gear Behavior*. National Advisory Committee For Aeronautics (NACA), Langley Aeronautical Laboratory, Langley Field, Va., 1953.

[26] NATO - Advisory Group For Aerospace Research & Development (AGARD), 7 Rue Ancelle, 92200 Neuilly-Sur-Seine, France. *Enhancement of Aircraft Ground Handling Simulation Capability*, 1998.

[27] R. K. Schmidt. *The Design of Aircraft Landing Gear*. SAE International, 400 Commonwealth Drive, Warrendale, PA 15096, USA, 2021.

[28] G. D. Padfield. *Helicopter Flight Dynamics: The Theory and Application of Flying Qualities and Simulation Modelling*. Blackwell Publishing, 2nd edition, 2007.

[29] W. Johnson. *Helicopter Theory*. Dover Publications, Inc., 31 East 2nd Street, Mineola, N.Y. 11501, 1994.

[30] J. G. Leishman. *Principles of Helicopter Aerodynamics*. Cambridge University Press, 32 Avenue of the Americas, New York, NY 10013-2473, USA, 2nd edition, 2006.

[31] W. Z. Shen, R. Mikkelsen, J. N. Sørensen, and C. Bak. Tip loss corrections for wind turbine computations. *Wind Energy*, 8(4):457–475, 2005.

[32] R. W. Prouty. *Helicopter Performance, Stability and Control*. Krieger Publishing Company, Inc., Krieger Drive, Malabar, Florida 32950, 1986.

[33] Air Force – Navy - Commerce Bulletin, Aircraft Design Criteria. *ANC-2, Ground Loads*, 1952.

[34] P. S. Suresh, N. K. Sura, and K. Shankar. Investigation of nonlinear landing gear behavior and dynamic responses on high performance aircraft. *Proceedings of the Institution of Mechanical Engineers, Part G: Journal of Aerospace Engineering*, 233(15):5674–5688, 2019.

[35] P. Sartor, R. K. Schmidt, W. Becker, K. Worden, D. A. Bond, and W. J. Staszewski. Conceptual design of a hard landing indication system using a flight parameter sensor simulation model. In *27th Congress of the International Council of the Aeronautical Sciences*, Nice, France, 19-24 September 2010.